ELECTROCHEMICAL PERFORMANCE OF LI-MG AND COLUMNAR SI ANODES FOR HIGH CAPACITY LI-ION CELLS: EXPERIMENTS AND MODELING OF CHARGE/ DISCHARGE BEHAVIOR

by

Madhusudan Jagannathan

A dissertation submitted to the faculty of
The University of Utah
in partial fulfillment of the requirements for the degree of

Doctor of Philosophy

Department of Metallurgical Engineering

The University of Utah

December 2013

The University of Utah Graduate School

STATEMENT OF DISSERTATION APPROVAL

The dissertation of Madhusudan Jagannathan

has been approved by the following supervisory committee members:

Ravi Chandran, Chair 9/30/2013
Date Approved

Michael L. Free, Member 9/30/2013
Date Approved

Manoranjan Misra, Member 9/30/2013
Date Approved

Henry White, Member 9/30/2013
Date Approved

Anil Virkar, Member 9/30/2013
Date Approved

and by Manoranjan Misra, Chair of

the Department of Metallurgical Engineering

and by David B. Kieda, Dean of The Graduate School.

ABSTRACT

This dissertation work can be divided into two parts: (1) an experimental section involving synthesis and electrochemical testing of (a) Li-Mg and (b) columnar Si anodes for high capacity Li-ion batteries, and (2) a theoretical modeling section in which analytical modeling frameworks are developed to predict (a) electrochemical charge/discharge behavior of amorphous Si thin film anodes, and (b) the discharge characteristics of a graphite/$LiFePO_4$ cell.

In the first part of the experimental work, two Li(Mg) alloys with nominal compositions, Li-60 wt.% Mg (Li_7Mg_3) and Li-30 wt.% Mg (Li_8Mg) were synthesized by direct alloying. These alloys showed electrochemical discharge characteristics that were comparable with those of pure Li. A phase transition, from the BCC Li(Mg) β-phase to the HCP Mg(Li) α-phase, was found to occur during the discharge. The Li(Mg) electrodes also showed some degree of reversibility when cycled against $LiCoO_2$ and Li.

In the second part of the experimental work, four different columnar Si structures were obtained by electrochemical etching. Si electrodes with porosities between 50-65% and with clear columnar structures showed reversible lithiation/delithiation capacities greater than 1000 mAh/g after 20 cycles, which is higher than the reported values in literature for Si anodes with similar structures. The Si electrode with wide interconnected pores showed poor electrochemical performance. The Si columns in the cycled electrodes appeared to be largely intact after 20 cycles.

In the theoretical modeling work, we first developed an analytical modeling framework to predict the lithiation/delithiation behavior of amorphous Si (a-Si) thin film electrodes. Li transport through the electrode (by diffusion) and electrochemical charge transfer at the electrode-electrolyte interface were described mathematically in this model. The simulated charge/discharge characteristics agreed well with the experimental data of a-Si thin film anodes at different C-rates.

An integrated model was developed to predict the discharge characteristics of a full cell consisting of graphite anode and $LiFePO_4$ cathode. In this model, the phase boundary movement within the $LiFePO_4$ electrode upon lithiation was described. When the simulation results for $LiFePO_4$/Li and LiC_6/Li half cells were coupled together, they were found to predict successfully the discharge behavior of a capacity-matched graphite/$LiFePO_4$ cell.

To my parents, Mr. S. Jagannathan and Mrs. Padma Jagannathan

TABLE OF CONTENTS

Chapters

LIST OF TABLES

ACKNOWLEDGEMENTS

I would like to express my heartiest gratitude to Prof. Ravi Chandran for providing me with the opportunity to pursue my Ph.D under his guidance. The various discussions we had over the course of my Ph.D not only enabled me to better understand the fundamentals of electrochemistry and diffusion, but also contributed in shaping my scientific outlook.

I would like to acknowledge my supervisory committee, Prof. Anil Virkar, Prof. Michael Free, Prof. Henry White and Prof. Mano Misra for their time and suggestions. I also want to thank Prof. G.V. Subba Rao and Dr. Neale Neelameggham for their valuable inputs.

Special thanks to my colleagues: Paul Chang, Biplab Sarma, Joshua Ramos, Bhaskar Vadlamani, Shawn (Yuxuan) Zhang for helping me out in the laboratory. This acknowledgment would not be complete without thanking Evelyn Wells, Kay Argyle, and Karen Haynes for their help with the administrative affairs in the department. I am grateful to the NSF-Division of Materials Research, DOE-Office of Science, and University of Utah Seed Grant for providing the financial support for this work. Last but not the least, I am thankful to my family for their blessings and support.

CHAPTER 1

INTRODUCTION

1.1 Background

Li-ion batteries have become the most widely used type of secondary batteries for portable electronic devices. They are preferred over other secondary battery systems such as Ni-Cd and Ni-MH cells, because of their higher gravimetric and volumetric capacities[1]. While Ni-Cd and Ni-MH cells have specific energies of 30-60 and 50-90 Wh/kg, respectively, a conventional Li-ion cell offers higher specific energy of 90-115 Wh/kg[2]. Amongst all rechargeable systems, Li-ion batteries offer the highest operating voltages, in the range of 3-5 V. Also, Li-ion cells have minimal self-discharge and lower maintenance requirements [3, 4].

Conventional Li-ion cells use $LiCoO_2$ as the cathode material and a graphitic anode, an electrode combination which was first developed by Sony [5] in the early 1990s. In these “rocking chair batteries,” Li^+ ions are shuttled back and forth between $LiCoO_2$ and graphite. These Li-ion cells have long cycle life, higher energy densities than NiCd batteries, and no major safety problems. However, miniaturization of electronic devices, development of next generation electric vehicles, and effective storage of renewable energy from wind and solar power generating stations require a manifold increase in the energy densities of batteries [3, 4].

While the specific energy and specific power provided by Li-ion batteries are sufficient to satisfy the requirements of hybrid-electric vehicles, all electric-vehicles require much larger energy capacities (See Figure 1.1). Therefore, further increases in energy density and functionality in terms of charge and discharge rates, are required if Li-based batteries are to become a practical reality in transportation and power industry. Such improvements cannot be achieved using conventional graphitic anodes and $LiCoO_2$

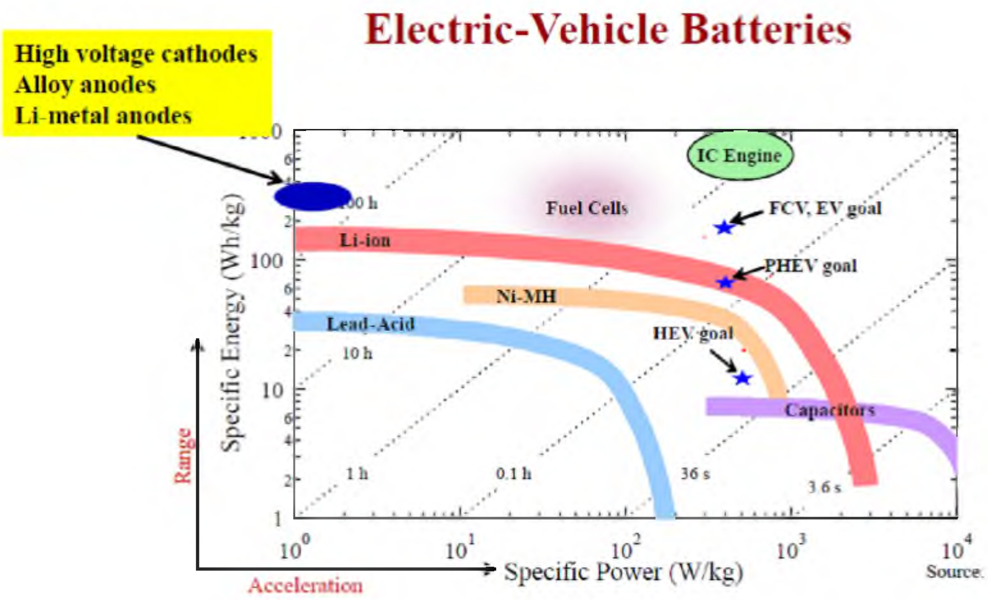

Figure 1.1 The specific energy and power capacities of several battery technologies for use in electric vehicles. Reprinted with permission from V. Srinivasan, Batteries for vehicular applications, AIP Conference Proceedings 1044, 283, 2008[6]. Copyright 2008, AIP Publishing LLC.

cathodes.

1.2 Alloy Anodes for Li-ion Batteries

The total cell capacity depends on the capacities of anode and cathode. While new cathode systems, such as $Li[Ni_xCo_{1-2x}Mn_x]O_2$ [7], Li-Mn-O spinels [8], $LiFePO_4$ [9, 10] are being investigated, it has been shown that they can lead to an increase of only 10-20% in the total capacity, which is not sufficient for plug-in electric vehicle applications. Hence, researchers are examining different anode systems which can provide superior capacities. Particularly, Li alloy anodes have attracted a lot of attention because their theoretical capacities are several times higher than those of carbonaceous anodes. The starting material for the alloy anode systems could be pure metals, solid solution alloys, or intermetallic compounds, either in crystalline or amorphous form. Si, Sb, Sn, Al and Mg are attractive candidates for alloy anodes because they are cheap, abundant, environmentally friendly and are known to form alloys with Li [11].

The major limitations associated with alloy anodes include short cycle life and rapid loss of reversible capacity as a result of volume expansion during Li insertion [3, 11-13]. The high volume changes, which can be as high as 400% during cycling, cause cracking and pulverization of the active particles and the surrounding matrix. This leads to electrode fragmentation and delamination from the current collector [12, 14-21], which in turn increases the electrode resistance, causing capacity fading that increases with the number of charge-discharge cycles.

To overcome these problems caused by volume changes, researchers have tried to use anodes consisting of amorphous/crystalline powders, thin films, and various architectures such as nanorods, nanowires. Most of these approaches have been employed on Si and Sn anodes because theoretically they have the highest Li uptake capacities, up to 4.4 atoms of Li per atom of Si or Sn (for $Li_{22}Si_5$ and $Li_{22}Sn_5$, respectively) [3]. The theoretical specific capacity of Si, when it is lithiated to $Li_{22}Si_5$, is 4200 mAh/g, which is the highest among alloying elements. But the increase in the volume when such compounds are formed is of the order of 300-400%.

The volume changes in the Li-Al and the Li-Mg system are not as high as they are with Li-Si or Li-Sn[22]. While Li forms a series of intermetallics with Al [23], it forms a solid solution with Mg over a wide range, from 30 at% Li to 100 at% Li [13, 24, 25]. The advantage in having a solid solution system is that the volume changes within a single phase are not abrupt, but continuously vary with Li content. However, this system has not been explored in detail before because of the difficulty in preparing homogeneous alloys due to the high reactivity of both Li and Mg [13, 25]. This research project aims to develop homogeneous Li-Mg alloys and investigate their electrochemical charge discharge characteristics, in order to assess the feasibility of using them as alloy anodes in rechargeable Li-ion batteries.

Considerable attention is also being focused on tailoring the nanostructures of anode particles to better accommodate the high volume changes. For example, Si nanowire architectures have been found to show good cyclability [26]. Also, porous anode structures obtained by depositing Si onto a porous current collector [27, 28] or onto a template [29, 30] have showed higher reversible capacities and longer cycle life than Si deposited on planar substrates [28]. Electrochemical etching of p-type Si by HF is a powerful method to prepare nanostructured porosity[31]. The etching conditions can be changed to control the morphology of the pores created in Si. The effect of columnar morphology of structured porous Si electrodes on their lithiation/delithiation behavior has not been systematically investigated. In this research, we plan to create different columnar morphologies on porous Si anode and examine the effect of morphology on its cyclability and capacity retention during electrochemical charge discharge testing.

Modeling of charge/discharge behavior of Li-ion cells, in particular the electrochemical insertion and deinsertion of Li^+ is challenging because of the complexity of the ion transport and phase transformations corresponding to Li intercalation and deintercalation. Mesoscopically, this requires analytical solutions of diffusion that incorporate moving phase boundaries due to phase transitions. In this research, we focus on developing an analytical computational scheme, using which one can predict the charge/discharge behavior of individual electrodes as well as full Li-ion cells.

1.3 Objectives of the Present Research

The objectives of the experimental section of this research work are as follows:

1. To synthesize homogeneous Li-Mg alloys, and to investigate their electrochemical charge discharge characteristics in order to assess the feasibility of using them as alloy anodes in Li-ion batteries. The corresponding phase transitions in these alloys and their reversibility during discharge and charge are to be established.
2. To fabricate Si anodes with structured columns with different pore morphologies so that the effect of morphology on the electrochemical performance as alloy anodes in Li-ion cells can be investigated.

The objectives of the modeling section of this research work are as follows:

1. To create a mathematical modeling framework to predict cell voltage and the charge/discharge behavior during electrochemical charge /discharge in order to get a phenomenological understanding of how Li transport through the electrodes and the electrolyte in Li-ion cells affects the electrochemical performance of the cells.
2. The accuracy of the thus constructed framework is to be verified by comparing the simulated results with experimental data of charge/discharge characteristics of (a) single electrodes (such as amorphous Si thin films vs. Li/Li^+), and (b) full cells consisting of commonly used anode/cathode materials (e.g., graphite/$LiFePO_4$).

1.4 References

1. M. Armand and J. M. Tarascon, *Nature*, **414**, 359 (2001).

2. H. J. Bergveld, W. S. Kruijt and P. H. L. Notten, *Battery Management Systems: Design by Modelling*, Kluwer Academic Publishers, Boston (2002).

3. U. Kasavajjula, C. Wang and A. J. Appleby, *Journal of Power Sources*, **163**, 1003 (2007).

4. A. Manthiram, *The Journal of Physical Chemistry Letters*, **2**, 176.

5. T. Nagaura, A lithium-ion battery, in *The Third International Rechargeable Battery Seminar*, Deerfield Beach, FL (March 5-7, 1990).

6. V. Srinivasan, in *AIP Conference Proceedings*, p. 283 (2008).

7. Z. Lu, D. D. MacNeil and J. R. Dahn, *Electrochemical and Solid-State Letters*, **4**, A200 (2001).

8. M. R. Mancini, L. Petrucci, F. Ronci, P. P. Prosini and S. Passerini, *Journal of Power Sources*, **76**, 91 (1998).

9. S. H. Wu, K. M. Hsiao and W. R. Liu, *Journal of Power Sources*, **146**, 550 (2005).

10. S. Y. Chung, J. T. Bloking and Y. M. Chiang, *Nature Materials*, **1**, 123 (2002).

11. W. J. Zhang, *Journal of Power Sources*, **196**, 13 (2011).

12. M. Winter, J. O. Besenhard, M. E. Spahr and P. Novak, *Advanced Materials*, **10**, 725 (1999).

13. D. Larcher, S. Beattie, M. Morcrette, K. Edstroem, J. C. Jumas and J. M. Tarascon, *J. Mater. Chem.*, **17**, 3759 (2007).

14. C. Wang, A. John Appleby and F. E. Little, *Journal of Power Sources*, **93**, 174 (2001).

15. J. Yang, M. Wachtler, M. Winter and J. O. Besenhard, *Electrochemical and Solid-State Letters*, **2**, 161 (1999).

16. H. Kim, J. Choi, H. J. Sohn and T. Kang, *Journal of The Electrochemical Society*, **146**, 4401 (1999).

17. M. Wachtler, M. Winter and J. O. Besenhard, *Journal of Power Sources*, **105**, 151 (2002).

18. M. Wachtler, J. O. Besenhard and M. Winter, *Journal of Power Sources*, **94**, 189 (2001).

19. J. W. Kim, J. H. Ryu, K. T. Lee and S. M. Oh, *Journal of Power Sources*, **147**, 227 (2005).

20. J. T. Vaughey, L. Fransson, H. A. Swinger, K. EdstrÃ¶m and M. M. Thackeray, *Journal of Power Sources*, **119**, 64 (2003).

21. L. Y. Beaulieu, K. W. Eberman, R. L. Turner, L. J. Krause and J. R. Dahn, *Electrochemical and Solid-State Letters*, **4**, A137 (2001).

22. J. O. Besenhard, J. Yang and M. Winter, *Journal of Power Sources*, **68**, 87 (1997).

23. A. J. McAlister, *Journal of Phase Equilibria*, **3**, 177 (1982).

24. C. M. Park, Y. U. Kim, H. Kim and H. J. Sohn, *Journal of Power Sources*, **158**, 1451 (2006).

25. T. J. Richardson and G. Chen, *Journal of Power Sources*, **174**, 810 (2007).

26. G. A. Roberts, E. J. Cairns and J. A. Reimer, *Journal of Power Sources*, **110**, 424 (2002).

27. L. Trahey, J. T. Vaughey, H. H. Kung and M. M. Thackeray, *Journal of The Electrochemical Society*, **156**, A385 (2009).

28. M. Yoshio, T. Tsumura and N. Dimov, *Journal of Power Sources*, **146**, 10 (2005).

29. K. Nishikawa, K. Dokko, K. Kinoshita, S. W. Woo and K. Kanamura, *Journal of Power Sources*, **189**, 726 (2009).

30. H. Zhao, C. Jiang, X. He and J. Ren, *Journal of Power Sources*, **184**, 532 (2008).

31. M. J. Sailor, *Porous Silicon in Practice*, Wiley-VCH, Weinheim, Germany (2012).

CHAPTER 2

LITERATURE REVIEW

2.1 Working Principle of Li-ion Cells

The basic principle of a Li-ion cell, with a graphitic anode and $LiCoO_2$ cathode, is illustrated in Figure 2.1. It shows how the Li^+ ion is transported from between the graphene layers in graphite anode to the $LiCoO_2$ cathode via the Li^+ ion-conducting electrolyte during discharge, and, in the opposite direction during charge [1]. Even though by definition, graphite is to be referred to as the negative electrode, not as anode (since the negative electrode becomes the anode during discharge and cathode during charging), for the sake of convenience, it is customary to use the term "anode" to refer to the negative electrode in a Li-ion cell. The current collectors in contact with the electrodes help in transporting the electrons from the electrode to the external circuit. In most cells, a porous separator soaked with electrolyte will be sandwiched between the two electrodes to prevent short circuiting. It is clear that for such a cell to have high cyclability, both the electrodes must facilitate reversible insertion and deinsertion of Li^+ ions over a large number of cycles, without a large drop in potential.

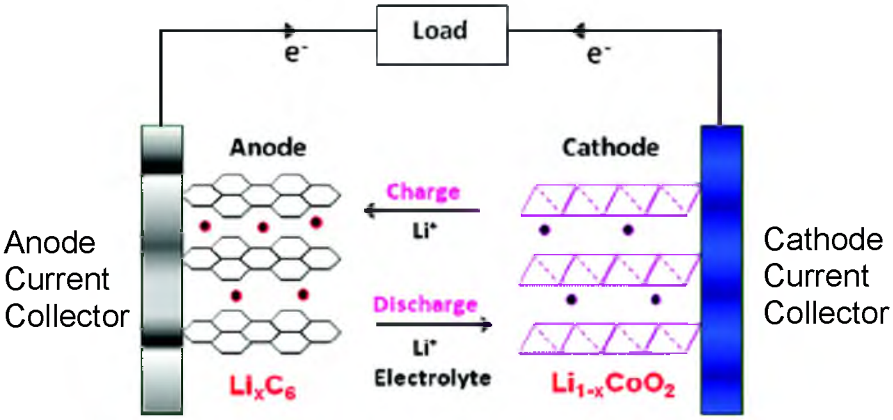

Figure 2.1 Schematic of a conventional Li-ion cell with graphitic anode and $LiCoO_2$ cathode. Reprinted with permission from A.Manthiram, Materials challenges and opportunities of lithium ion batteries, The Journal of Physical Chemistry Letters, 2(3), 176, 2011[1]. Copyright 2011 American Chemical Society.

2.2 Anodes in Li-ion Batteries

2.2.1 Metallic Li Anodes

In the past, attempts were made to use metallic Li as the anode because theoretically it offers a very high specific capacity, about 3800 mAh/g. However, it was found that the cycling performance of cells with metallic Li anodes was poor. A passivating layer was observed to form at the Li/electrolyte interface during charging which limits the diffusion of Li and modifies the charge transfer mechanism. The high reactivity of Li surface causes this layer to grow continually thus further increasing the impedance of the electrode. More importantly, Li metal anodes show an increased tendency to form dendrites during Li plating, which is aggravated by the nonuniform current density distribution at the surface[2-9]. Accumulation of these dendrites at the surface (see Figure 2.2) leads to safety issues because some of them can penetrate the separator, touch the cathode, and create a short circuit. The dendritic deposition of Li converts the Li anode into high surface area powder with high reactivity towards organic compounds. For instance, for an electrolyte consisting of $LiPF_6$ salt in a solution of

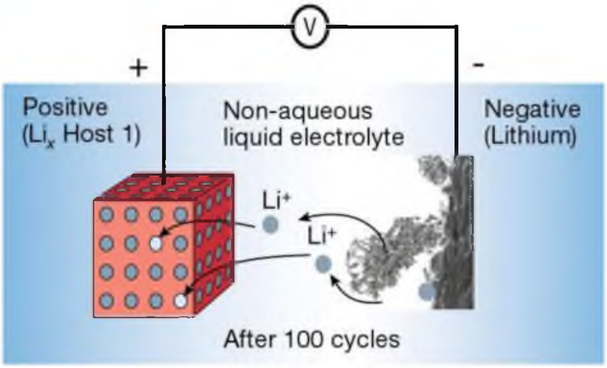

Figure 2.2 Formation of dendritic deposits on Li metal surface during cycling. Reprinted by permission from Macmillan Publishers Ltd: Nature, J.M.Tarascon and M. Armand, Issues and challenges facing rechargeable lithium batteries, Nature 414(6861), 359, 2001.[11] Copyright 2001.

ethylene carbonate and dimethyl carbonate, the compounds formed at the Li metal anode surface include $LiCH_2CH_2OCO_2Li$, LiOH, Li_2O, Li_2CO_3, LiF, CH_3OCO_2Li, CH_3OLi, etc. [10]. The reaction of dendrites with the electrolyte, apart from causing safety hazards also reduces the amount of active Li available for cycling, thus leading to poor cyclability of the cell.

Due to the above problems associated with metallic Li, research was redirected towards finding alternative anode materials for Li-ion cells. Graphite became an acceptable anode material for Li-ion cell in the early 1990s. Its working principle involved intercalation and deintercalation of Li between graphite layers. The anodic reaction in a Li-ion cell can be broadly divided into three categories: (1) intercalation reaction, (2) conversion reaction and (3) alloying.

2.2.2 Intercalation Reaction Anodes

Li intercalation in Li-ion cells involves insertion and deinsertion of Li into the anode material without causing large structural rearrangements in the host lattice. During intercalation, Li occupies an initially empty site in the host framework without breaking any bonds within the solid structure. Therefore, the structure of the intercalated compound is similar to that of the starting material, which makes the reaction truly reversible. This type of reaction occurs in anodes such as graphite and $Li_4Ti_5O_{12}$ (LTO), a new generation anode material. Graphite is the most commonly used anode material in commercial Li-ion batteries [12].

2.2.2.1 Graphitic anodes

Deep charge discharge cycling of Li-ion cells with graphitic anodes was first achieved by Sony Japan in the early 1990s [13, 14] and paved the way for the commercial success of Li-ion batteries. These cells are normally in the discharged state where Lithium is deintercalated from $LiCoO_2$ cathode and is inserted in graphite during charging. This type of battery exhibited good reversibility for over 1200 cycles. However, these cells have some first-cycle irreversible capacity loss, caused by the formation of a solid electrolyte interface (SEI) film on the surface, which is mostly due to decomposition and reaction of electrolyte with graphite anode. The SEI has benefits: while it allows the transport of Li ions, it also protects the anode surface against further degradation [15].

The improved reversibility provided by graphitic anodes is due to their layered structure consisting of basal planes stacked in c-direction, which allows intercalation of Li ions between the layers without large volume changes. The maximum extent of Li insertion into graphite corresponds to the formation of LiC_6, where one Li atom coordinates with each of the six C atoms of the basal plane. The layer spacing of LiC_6 is only 10% larger than that for pure graphite [16]. The electrode reaction is

$$LiC_6 \rightleftharpoons Li_xC_6 + (1-x)\ e^- + (1-x)\ Li^+ \qquad (2.1)$$

where $0<x<1$. This electrochemical reaction occurs at 0.1-0.2V vs. Li^+/Li (at nominal C-rates)[17], and hence the voltage penalty for using graphitic anodes instead of metallic Li anodes is very small. Figure 2.3 shows the charge and discharge curves in a cell with

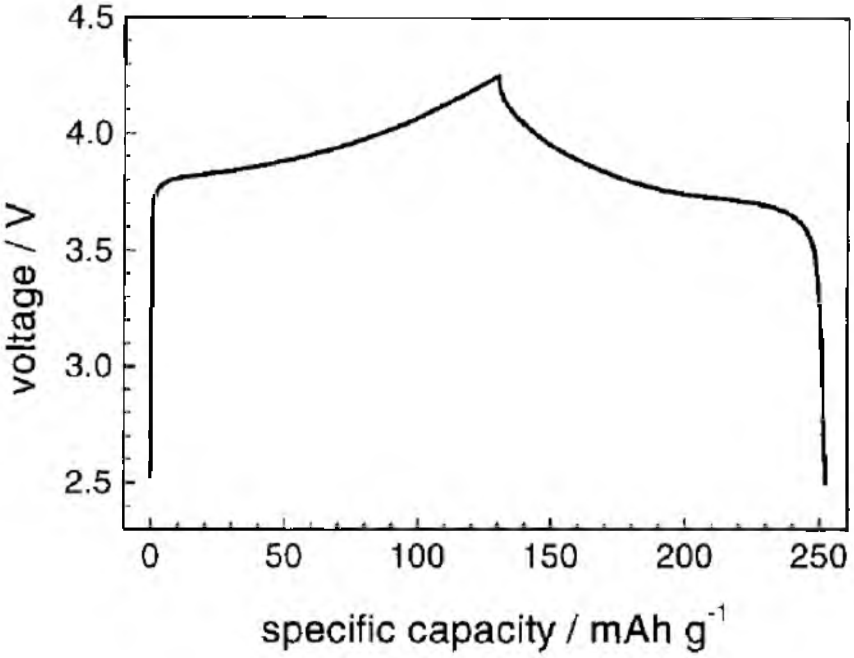

Figure 2.3 Typical charge and discharge curve for a cell with $LiCoO_2$ cathode and graphite anode at 0.2 C rate [19]. Reprinted from Springer and Journal of Applied Electrochemistry, Electrochemical evaluation of $LiCoO_2$ synthesized by decomposition and intercalation of hydroxides for lithium-ion battery applications, 28, 1998, 1365-1369, B. Huang, Y-I. Jang, Y-M. Chiang, D. R. Sadoway, Figure 6, ©1998 Springer, with kind permission from Springer Science + Business Media.

$LiCoO_2$ cathode and graphite anode at a slow rate of 0.2C. This cell is usually charged up to a voltage of 4.25 V and discharged to 2.5 V.

The reduction of electrolyte on the graphite surface occurs due to transfer of electrons across the interface from anode to the electrolyte, resulting in the formation of the SEI layer. Even though this layer prevents further reaction with electrolyte, the SEI layer limits Li ion diffusion and sometimes leads to plating of metallic Li on the surface, especially at high charging rates [18]. Li plating can lead to dendrite formation leading to internal short circuiting, and cell fire. The major disadvantage of graphitic anode is its low capacity. The theoretical capacity of graphite is 372 mAh/g [20, 21], which is 2-10 times lower than that of alloy anodes.

2.2.2.2 Lithium Titanate (LTO) Anode

In lithium titanate (with formula $Li_4Ti_5O_{12}$ and a cubic spinel structure), Li insertion occurs without any strain up to a stoichiometry of $Li_{6\text{-}7}Ti_50_{12}$ and hence is highly reversible. LTO has high thermal stability and long cycle life. It does not require the presence of passivating films on the surface because there is no reduction of electrolyte on the anode surface. The mobility of Li ion in lithium titanate during charge-discharge processes is high. But it has a low specific capacity of 150-160 mAh/g, which is lower than even that of graphite [22]. Also, the voltage penalty is high as the insertion reaction occurs at 1.5 V vs. Li^+/Li. Because of this high voltage of LTO vs. Li/Li^+ couple, the possibility of Li plating on the anode is eliminated [23].

2.2.3 Conversion Reaction Anodes

Certain anode materials rely on conversion and displacement upon Li insertion. Such reactions involve complete electrochemical reduction of metal oxides, sulfides, nitrides, phosphides and fluorides of the form, M_aX_b (M = transition metal, X = O, S, F, P, N…), by Li, to yield metallic nanoparticles embedded in a matrix of Li_yX. These reactions involve the reduction of the transition metal to its metallic state, delivering remarkably high capacity values. Poizot *et al.*[24, 25] first showed that nanoparticles of transition metal oxides, such as CuO, CoO, and Fe_2O_3 are reversibly reduced by Li ions according to the following equation:

$$\text{Nano-MO} + 2Li^+ + 2e^- \rightleftharpoons \text{nano-M} + Li_2O \qquad (2.2)$$

In such reactions, more than one electron transfer occurs per transition metal ion, as opposed to 0.5-1.0 electrons, which is typical for intercalation compounds. However, the voltages during charge-discharge cycles carried out on these anodes show a prominent hysteresis, as can be seen from Figure 2.4 which shows charge and discharge voltage curves as a function of composition curve for CoO/Li, NiO/Li, and FeO/Li cells at a C/5 rate. Special mention must be made of two systems: Li-S and Li-air batteries, which utilize conversion chemistry and show promise to offer high capacities[1].

2.2.3.1 Li-S Batteries

The Li-S system involves the following electrochemical reaction between Li metallic anode and S cathode:

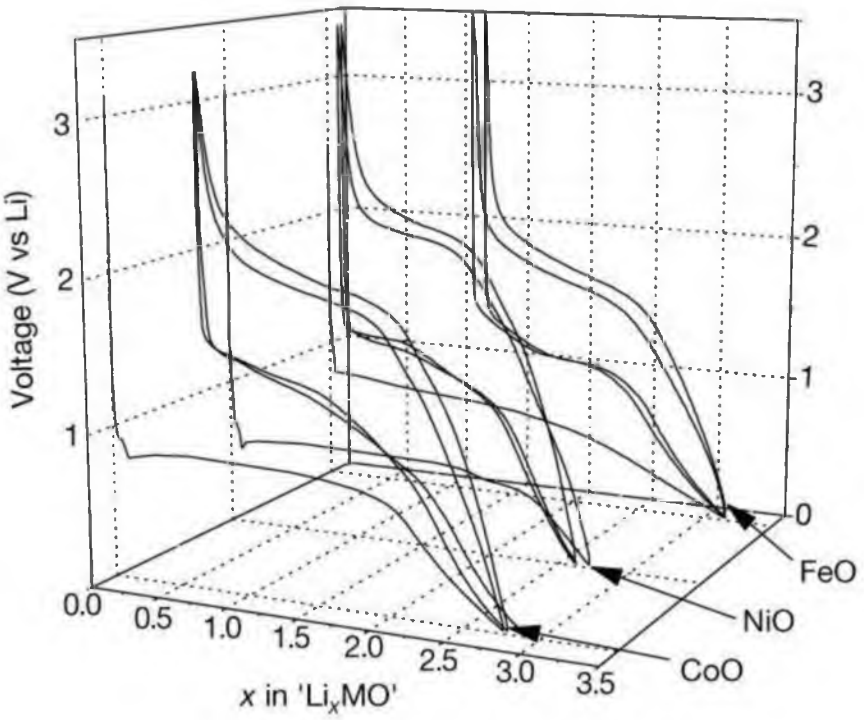

Figure 2.4 The voltage–composition profile for various MO/Li cells cycled between 0.01 V and 3 V at a rate of C/5 (1 lithium in 5 hours). Reprinted by permission from Macmillan Publishers Ltd: Nature, P.Poizot, S.Laruelle, S.Grugeon, L.Dupont, and J.M.Tarascon, Nano-sized transition-metal oxides as negative-electrode materials for lithium-ion batteries, Nature, 407(6803), 496, 2000 [24], copyright 2000.

$$2\,Li+S \rightleftharpoons Li_2S \tag{2.3}$$

This system can provide a specific capacity of 1675 mAh/g and an open circuit potential of 2.23 V vs. Li, leading to a theoretical energy density of 3730 Wh/kg. But high solubility of the cell reaction products in organic carbonate electrolytes used in conventional Li-ion batteries is a huge problem that has prevented effective commercialization of these cells[26, 27]. The reaction products, which are polysulfides of the form Li_xS_y dissolve in the electrolyte and can even sometimes diffuse towards the Li electrode, leading to capacity fade during cycling. It has been shown that this dissolution problem could be averted if the liquid organic electrolytes are replaced with polymer gel-type Li-ion conducting electrolyte membranes [28-30].

Another basic issue is the low electrical conductivity of S, Li_2S and the other Li-S products. This concern is addressed by using sulfur-carbon composite electrodes as the cathode material instead of S[27, 31-33]. The disadvantages associated with Li metallic anode are applicable in this system too, and hence, systems with Li_2S-C composite cathodes and alternative anodes such as Sn-C or Si-C are being investigated [34-36].

2.2.3.2 Li-Air Batteries

Li-air batteries are attracting a lot of attention because of their high capacities and abundant supply of oxygen from air. They are estimated to have theoretical energy densities as high as 5000 Wh/kg [37]. Li-air cells consist of a Li metal anode along with a porous carbon electrode exposed to air with nonaqueous or aqueous electrolytes [37, 38]. In the case of aqueous electrolyte, the following reaction occurs:

$$O_2 + 4\,Li + 2\,H_2O \rightleftharpoons 4\,LiOH \qquad (2.4)$$

In a practical version of Li-air cell, a Li^+ ion conducting glass ceramic is used to separate the Li anode and electrolyte. In the second category of Li-air batteries, nonaqueous electrolytes are used and the following reaction occurs:

$$4\,Li + O_2 \rightleftharpoons 2\,Li_2O \qquad (2.5)$$

This reaction provides atheoretical energy density of ~5200 Wh/kg and occurs at a potential of ~2.91 V [37, 38]. The discharge-charge proceses in Li-air cells involve the formation of a series of products : Li_2O_2 superoxide, then Li_2O_2 and finally Li_2O. The major challenges to be overcome include selection of appropriate electrocatalysts for air electrode during oxygen evolution and reduction, protection of electrolyte and anode from attack by CO_2 and H_2O, and safety concerns and poor cyclability of metallic Li electrode.

To solve the problem of corrosion of Li metallic anode in the presence of moisture in Li-air batteries, Visco *et al.* [39] developed a protected lithium-metal electrode (PLE). In PLEs, the Li metal is covered by a Li-ion conducting solid electrolyte film, such as Lisicon, which prevents contact with soluble intermediate compounds and electroylte, and at the same time allows transport of Li^+ ions. Another interlayer is required between Li metal and the Lisicon layer to prevent reduction of the latter. In Li-air batteries with such electrodes, reasonable capacity retention has been observed even after 40 cycles [40].

Figure 2.5 shows the relative capacities and voltages of different anode and

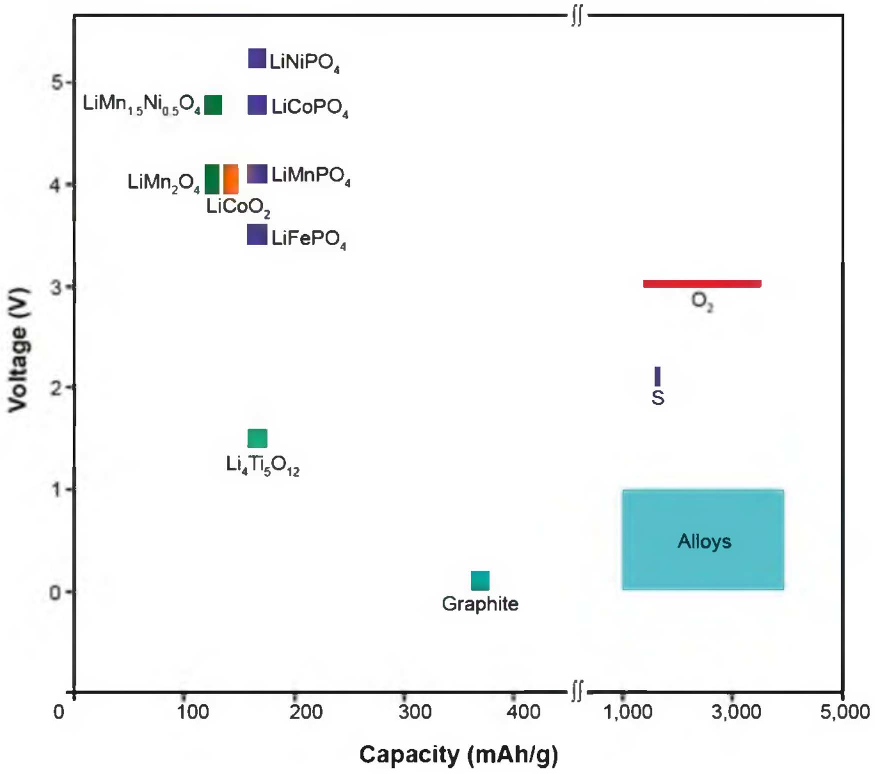

Figure 2.5 Voltage (vs. Li^+/Li) and capacity ranges of various anode and cathode materials in Li-ion cells. Reprinted with permission from A. Manthiram, Materials challenges and opportunities of lithium ion batteries, The Journal of Physical Chemistry Letters, 2(3), 176, 2011 [1]. Copyright 2011 American Chemical Society.

cathode materials used in Li-ion cells. It can be seen that cells with alloy anodes and the cathodes given on the top left side of the figure will show high voltages and capacities, much higher than those provided by LTO and graphitic anodes. S and O_2 cathodes will have capacities higher than 1000 mAh/g and voltages between 2 and 3 V vs. Li^+/Li.

2.2.4 Alloy Reaction Anodes

Alloying reaction refers to the formation of intermetallic compounds of the form Li_xM during Li insertion, as in the case of Li-Sn, Li-Si, Li-Al, etc. It can also occur in a solid solution system such as Li-Mg in which Li can be inserted or deinserted without a phase change, for a specific compositional range. These systems can offer capacities 2-10 times higher than that of graphite. However, the volume change during Li insertion in these anodes is of the order of 100-300%, which is much higher than that observed in graphite (~10%).

The first systematic work on Li alloys involved their use in high temperature batteries (~ 400°C), which have molten salts as electrolytes. Li metal cannot be used in these systems because of its low melting point, 180°C [41]. Alloying of Li with several metals at room temperature was first observed when these metals were used as substrates for electrodeposition of metallic Li from Li^+ containing electrolytes[42-45]. Bauman *et al.*[46] observed that the deposition of Li formed a black deposit, which could not be easily removed by reaction with water, indicative of the formation of Li-Pt alloy. Selim *et al.* [47]and Brauer *et al.* [48] found out that the reversibility of Li electrodeposition was higher on substrates such as Ag, Al and Pt, metals with which Li is known to alloy, than on Cu, Ni, and stainless steel. Dey [49] systematically studied the reaction products of Li electrodeposition on several metal substrates and divided them into two categories. The first category consisted of metals with which Li formed alloys and included Sn, Pb, Mg, Ag, Au, Pt, Zn, and Cd. The second category included metals with which Li did not show significant alloying (Ti, Cu, Ni, and stainless steel). Subsequently, others studied alloying and delloying phenomena in Li-As, Li-Sb, Li-Bi[50, 51], Li-Al[52-54], Li-Mg[55, 56], , Li-Si[57, 58] systems. In particular, between the 1970s and the 1990s, numerous research efforts were focused on the replacement of metallic Li anode by Li alloys in rechargeable Li cells[59-64]. Matsuhita-Panasonic used Wood's metal (an alloy of Bi, Pb, Sn, Cd) as an anode in commercial button type cells[65, 66].

The announcement of a carbonaceous anode by Sony in early 1990s [13, 14], led to development of cells which showed very good and deep charge/discharge cycling behavior. This shifted the focus from alloy anodes to different forms of carbon anodes. However, in the recent years, the quest for cells with higher energy densities has led to renewed interest in alloy anodes. Apart from their high gravimetric and volumetric capacities, alloy anodes are relatively inexpensive, and operate at high potentials. Their disadvantages include limited cell reversibility, high first-cycle irreversible capacity loss and capacity fading, which occur due to the large volume expansion in the material upon Li insertion. Most of the present research on alloy anodes is focused on resolving these problems in Li-Si, Li-Sn, and Li-Sb systems and on composite anodes consisting of these elements.

Before going on to examine the performance of various alloy systems, it would be instructive to understand how the thermodynamics and kinetics of alloying and dealloying affect the electrochemical performance, especially the voltage during discharging and charging.

2.2.4.1 Electrochemical Perspective of Alloying-Dealloying

Insertion and deinsertion of Li in most alloy anodes occur at a potential in the range of 0-1 V vs. Li^+/Li[1]. The equilibrium alloying potential for the reactions of the form:

$$\mathrm{Li} + x\,\mathrm{M} \rightleftharpoons \mathrm{LiM}_x \tag{2.6}$$

can be calculated by the Nernst equation[67] as follows:

$$E_A = -\frac{\Delta G_f}{nF} \tag{2.7}$$

where ΔG_f is the free energy of formation of the product LiM_x, n is the number of electrons involved in the reaction and F is the Faraday's constant. ΔG_f is the reversible change in free energy under electrochemical alloying of the cell and is related to the emf of the cell. Hence, this is the initial potential at the beginning of the discharge. The shape of the subsequent voltage curve also depends on the alloying mechanism.

If Li insertion into a metal M results in the formation of a new compound or a phase, such as LiM_x, then further lithiation will result in advancement of the two-phase (LiM_x/M) boundary within the electrode without changing the composition of the two phases significantly. In this two-phase region, the chemical potential of Li is equal in both the phases and is composition-independent. Therefore, we see a flat plateau in the voltage vs. composition curve in this region[68]. Figure 2.6(a) shows several such plateau potentials for the Li-Si and the Li-Sn system during coulometric titration.

Another type of insertion mechanism is the solid solution reaction which involves insertion of Li into the crystal structure of the host species without causing a phase change. The Li activity in the existing phase changes continuously during Li incorporation, thereby inducing a sloping potential profile during lithiation/delithiation. Such a profile can be seen in Figure 2.6(b), which shows the charge-discharge voltage curves for tin oxide anode[70].

In the following sections, several individual alloy systems will be examined one by one, with a discussion on their advantages and limitations, following which a side by side comparison of these systems will be made.

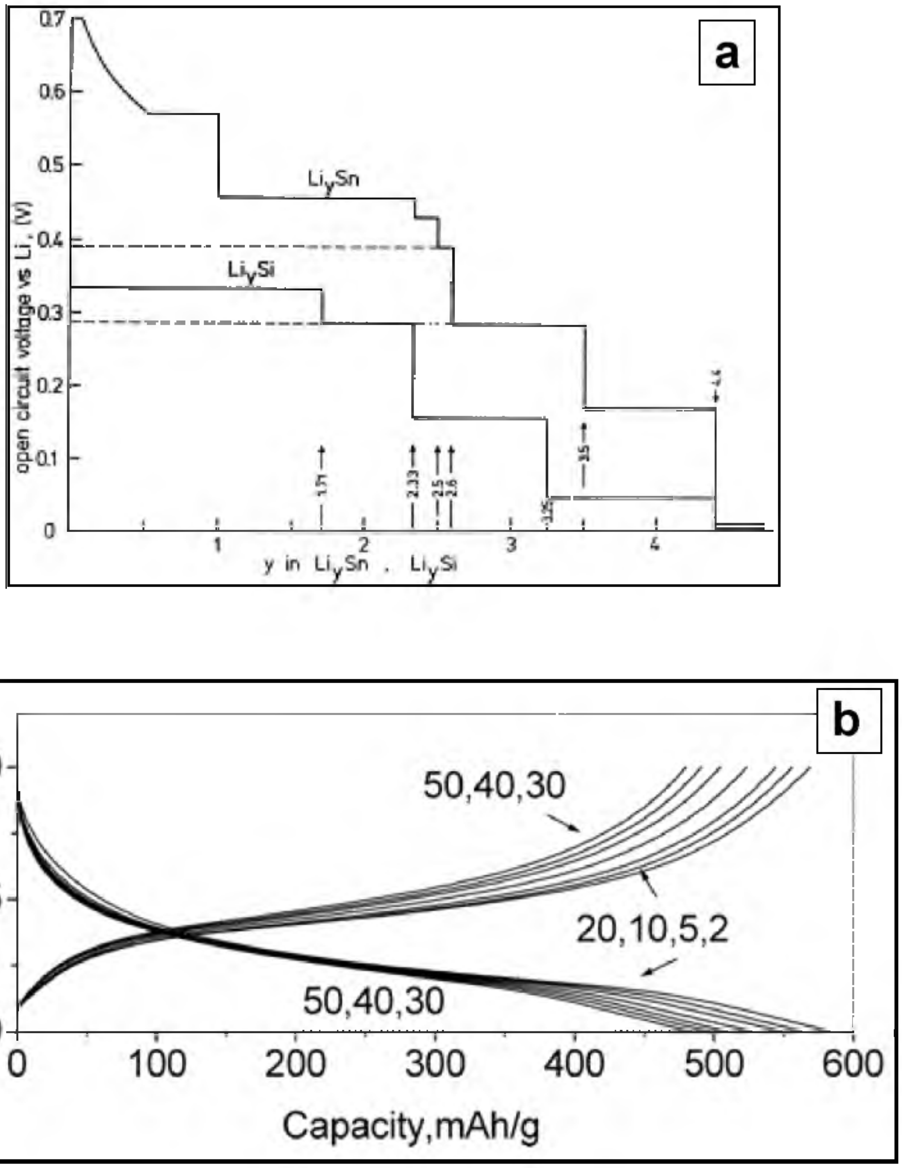

Figure 2.6 Charge/discharge curves showing plateau potentials and sloping voltage profiles in different systems. (a) shows well defined voltage plateaus during equilibrium titration in Li-Sn and Li-Si systems and (b) shows sloping charge/discharge voltage curves for tin oxide with hollandite structure. (a) is reprinted from Journal of Power Sources, 81, R.A.Huggins, Lithium alloy negative electrodes, 13-19, Copyright 1999, with permission from Elsevier[69]. (b) is reprinted with permission from N. Sharma, J. Plevert, G. V. Subba Rao, B. V. R. Chowdari, and T. J. White, Tin oxides with hollandite structure as anodes for lithium ion batteries, Chemistry of Materials 17(18), 4700, 2005[70]. Copyright 2005 American Chemical Society.

2.2.4.2 Li-Al Alloy Anodes

The use of Li-Al alloy anode was extensively researched to explore the possibility of replacing Li as anode material in primary Li batteries[71, 72]. The high temperature LiAl/ FeS_2 system has been well researched [73, 74]. According to the Li-Al phase diagram, at the Al rich side, there is a solid solution phase of Li in Al, (the α phase) and as Li content is increased, the intermetallic compounds LiAl (β), Li_3Al_2, and Li_9Al_4 [75] form. The solubility of Al in Li is very low. At 423°C, the solid solubility limit of Li in Al is 9.2 at% , the β phase exists between 47 to 56 at% and the γ phase between 60.3 and 61.7 at% Li.

The maximum theoretical uptake of Li in Al (for Li_9Al_4) is 2.25 Li per Al atom, providing a theoretical specific capacity of 2234 mAh/g. For LiAl , the capacity is 993 mAh/g. During electrochemical lithiation of Al, a voltage plateau was observed at 0.26 V vs. Li^+/Li, which corresponds to the formation of LiAl; however, there was no further plateau between 0.26 V and 10 mV vs. Li^+/Li, which indicates that other intermetallic Li-Al compounds do not form. The dealloying was observed to occur at a a potential of ~0.43 V vs. Li^+/Li [76, 77]. However, the LiAl phase could not be identified by X-ray diffraction analysis, indicating that the electrochemically formed LiAl could be amorphous [76-78].

There are contradictory reports on the electrochemical performance of LiAl alloy anodes. While Besenhard *et al.* [52, 79] reported that electrochemically formed LiAl showed poor Li recovery on cycling, Geronov *et al.*[80] have cycled LiAl alloys for >220 cycles with reversible capacity of 667 mAh/g. It is commonly agreed that loss of contact of LiAl with the substrate is a major limitation which reduces the cyclability of LiAl anodes [52, 59, [79, 80]. This is confirmed by the fact that on pressing LiAl onto a Cu current collector at a stress of 20 MPa, better cycling performance was obtained [79].

Since LiAl is known to be a hard and brittle compound, the loss of contact with the current collector can be attributed to the electrode fragmentation resulting from the volume expansion during Li insertion [59]. When inspected under the scanning electron microscope, the cycled LiAl electrodes were found to be heavily cracked and powdered [79, 81-83]. Because of the reduced effect of the volume changes in the case of nanoparticles, finely dispersed LiAl nanoparticles in a a polyacetylene matrix were found to show better electrochemical performance under cycling than thin film LiAl anodes [84].

Also, the diffusivity of Li in β-LiAl phase is 7 x 10^{-9} cm^2/s (at room temperature), whereas in α-Al phase, it is much lower, about 2-5 x 10^{-11} cm^2/s [80, 85]. So, if the α phase is formed during discharge, and in the subsequent charging cycle, if the alloying kinetics becomes sluggish, then Li plating can occur on the surface, which can quickly lead to loss of reversible capacity [59].

Thus, the high volume changes coupled with low diffusivity of Li in the α-phase are major limitiations for adopting Al as the negative electrodes in Li-ion batteries. The actual capacity of Al anodes (600-700 mAh/g) is also lower than that which can be offered by other alloy systems.

2.2.4.3 Li-Sn Alloy Anodes

The Li-Sn alloy system has attracted a lot of interest after the announcement of the Stalion Li-ion cell by Fuji Photo Film Celltec in 1997 [86]. This cell employed the standard $LiCoO_2$ cathode but an amorphous Sn based composite oxide as anode material. This cell showed high specific charging capacity due to the alloying reaction between Li and metallic Sn.

Lithiation of Sn electrode in a Li^+ ion containing electrolyte leads to the formation of a number of intermetallic compounds with the formula Li_xSn_y at a high temperature of 415°C [87] as well as at room temperature [88-90]. Li-Sn diagram suggests that there are 8 crystalline phases that sequentially can form at room temperature: Sn, Li_2Sn_5, LiSn, Li_7Sn_3, Li_5Sn_2, $Li_{13}Sn_5$, Li_7Sn_2, and $Li_{22}Sn_5$. Lithiation occurs at the potentials, 0.66, 0.53, 0.485, 0.42, and 0.38V, respectively, vs. Li/Li^+ [91] as determined by coulombic titration. These potentials correspond to the different two-phase regions in the Li-Sn system. The formation of Li_7Sn_3 and $Li_{22}Sn_5$ at voltages <0.31V was observed but could not be distinguished by X-ray diffraction because the structures of the two phases are similar. The final lithiated product was identified to be $Li_{22}Sn_5$. During dealloying, the formation of LiSn was reported to occur at 0.78 V vs. Li^+/Li and Sn was formed at 1.0 V. These delithiation potentials are higher than the equilibrium values [92].

The formation of various Li_xSn_y phases has also been confirmed by X-ray diffraction on electrodes during very slow near-equilibrium electrochemical charging experiments[60, 90, 93]. But, at room temperature and under practical charging conditions, only Li_2Sn_5 and LiSn are the dominant phases which can be distinguished[94, 95].

During lithiation, Sn anode pulverizes rapidly due to large volume increase. However, if the lithiation is stopped when stoichiometric LiSn is formed, this problem is solved to some extent because the differences between densities of pure Sn and LiSn/ Li_2Sn_5 are relatively small. Further alloying leads to the formation of other Li-rich Li_xSn_y compounds that have much lower densities than Sn because of an increase in lattice volume. Such major structural rearrangements increase the mechanical stresses in the host lattice [41].

As in other systems, the dimensional stability of the the electrode material during alloying and dealloying depend on the particle size, shape, texture and porosity[96, 97]. For anodes with coarse Sn particles, cracking and delamination of active material from the substrate occurs earlier in the cycling life than for small sized Sn anodes. If the cracks are deep enough, the electrolyte can penetrate and even react with the current collector, forming products that tend to insulate the current collector. The amount of active material available for cycling reduces with loss of electronic contact between the particles and the collector. This eventually leads to electrode failure [41]. Although, all these effects occur due to volume change, the major increase in the volume actually occurs in the first alloying cycle. The volume changes during the subsequent cycles are not large, which indicates that the electrode does not return to its original volume upon Li removal [17]. Hence, the resulting porous regions of the electrode help in better accommodation of Li ions with lower volume expansions in the following cycles.

Even though anodes with nanosized Sn particles exhibit better cycling performance than the coarser ones, the stability of capacity under further cycling is poor. To improve the electrode performance, Sn-based intermetallic and/or composite hosts were experimented with [41] and they show better cycling characteristics. For instance, the reversiblity of Sn/SnSb or Sn/$SnAg_3$/$SnAg_4$ composite anodes is superior to that of pure Sn based anodes with comparable particle sizes. In the composite electrode such as Sn/SnSb, SnSb gets lithiated at 850 mV vs. Li^+/Li, whereas Sn lithiates at 650-670 mV vs. Li^+/Li; hence at 850 mV, Sn acts as an inactive buffer [41]. Such Sn-M-C like systems, with an active component and an inactive buffer have also been found to yield better cycling performance as anode materials, where Ti, V, Cr, Mn, Fe, and Co have been tried out as M [98]. In 2005, Sony Corporation introduced a new Li-ion battery called Nexelion with an amorphous Sn-Co-C composite as the anode[99].

2.2.4.4 Li-Si Alloy Anodes

Sharma and Seefurth [100] first reported the formation of Li-Si alloys in high temperature electrochemical cells operating at 400-500°C. Compounds such as $Li_{12}Si_7$, $Li_{14}Si_6$, $Li_{13}Si_4$ and $Li_{22}Si_5$ [100-102] were observed to form during lithiation of Si. The alloying was found to be reversible even at room temperature[124]. $Li_{22}Si_5$ has a specific energy capacity of 4200 mAh/g, which is the highest amongst all alloying elements. The high specific capacity, abundance of Si, and the relatively low cost of raw material have led to the choice of Li-Si as the most studied alloy anode system for Li-ion cells in the past few years.

Si-based anodes suffer from capacity loss due to several factors. The first cycle irreversible capacity loss and capacity fade in subsequent cycles are major challenges for Si anode systems during cycling. For example, in the case of bulk Si anode, the initial charge cycle showed a capacity of 3260 mAh/g, which was followed by a discharge capacity of 1170 mAh/g, corresponding to a coulombic efficiency of only 35% [103]. By the end of the 5th cycle, the reversible capacity reduced to 500 mAh/g. As in the case of other alloy anodes, the progressively larger volume changes occurring with the formation of Li_xSi_y compounds during lithiation leads to development of stresses within the electrode. These stresses cause cracking within electrode and lead to loss of electronic contact and reduced availability of active element, thus decreasing the capacity.

Some of the approaches to overcome these challenges include using (1) Si nanosized powder anodes, (2) Si thin films, (3) architectured Si anodes, and (4) Si particles dispersed in active/inactive matrix.

In Si anode, Li insertion decreases the internal resistance because the Li-Si compounds have higher electrical conductivity than Si and conversely, during dealloying the resistance increases. Complete dealloying does not occur since some Li^+ ions are trapped inside the alloy particles [103]. Graphite flakes and/or nanoscale carbon black, when added to Si improve the electronic contact between particles [104]. By narrowing the voltage window, the cell reversibility can be improved, but at the cost of capacity. Nanosized Si powders, synthesized by laser-induced silane gas reaction showed higher reversible capacity of 1729 mAh/g in the 10th cycle (compared to 500 mAh/g after 5th cycle for bulk Si anode) [105, 106].

Thin film Si anodes with nano Si particles have longer cycle life, higher reversible capacities and better capacity retention than bulk Si anodes. Si thin films can be synthesized using amorphous or nanocrystalline Si particles. Nanocrystalline Si thin films showed an initial capacity of 2400 mAh/g and a discharge capacity of 1000 mAh/g [107]. After 50 cycles, it showed a reversible capacity of 525 mAh/g, which is much better than the performance of bulk Si. It is believed that the good adhesion achieved between the deposited particles and the current collector substrate is during deposition processes is responsible for the superior performance of the thin film anodes.

The cycling performance of amorphous Si thin films deposited on Ni foils by physical vapor deposition [107] and vacuum evaporation [108] were found to be even superior to that of nanocrystalline Si thin film anodes. As shown in Figure 2.7, the amorphous thin films show better charge-discharge characteristics than both bulk Si and nanocrystalline

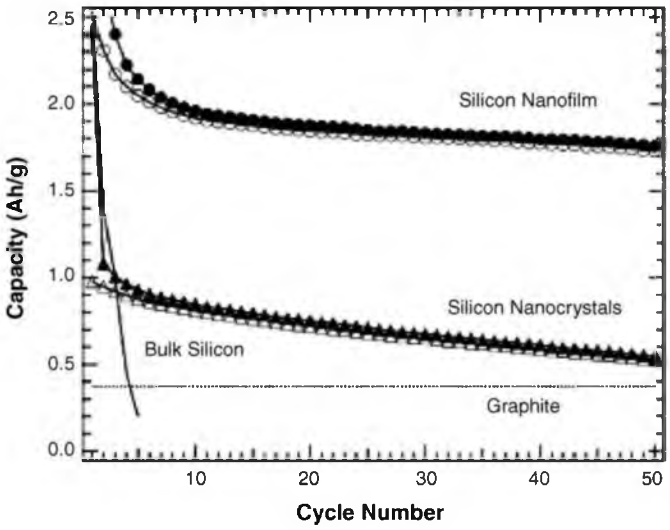

Figure 2.7 Specific capacity vs. cycle number for nanocrystalline Si and nanoamorphous Si thin film anodes prepared by thermal vapor deposition. Specific capacity of graphite and bulk-silicon anodes is also shown. Reprinted from J. Graetz, C. C. Ahn, R. Yazami, and B. Fultz, Highly reversible lithium storage in nanostructured silicon, Electrochemical and Solid-State Letters 6(9), A194, 2003[107]. Reproduced by permission of The Electrochemical Society.

Si powder anodes. The figure shows a comparison between the anode capacities of nanoamorphous Si thin films, Si nanocrystals, and bulk Si plotted against cycle number. The capacity of graphite is also included for reference. The open points indicate the voltages during alloying and the filled points represent dealloying cycles. As can be seen, amorphous Si thin films show a stable reversible capacity of 2000 mAh/g even after 50 cycles, which is the highest among all types of Si anodes. The capacity fade is also the least among all systems.

X-ray diffraction analysis performed on crystalline Si anodes, lithiated to 74% mol Li, revealed the presence of only the initial crystalline Si phase and a few unidentified broad peaks, none of which corresponded to the three expected crystalline Li-Si phases. High resolution transmission electron microscopy of this electrode showed that crystalline Si coexisted with an unknown amorphous phase [109, 110]. It is suggested that during Li insertion, crystalline Si is converted to an amorphous lithiated phase, leading to the formation of a two-phase region. However, at voltages lower than 0.050 V, crystalline $Li_{15}Si_4$ is reported to form, again leading to a two-phase region (amorphous phase + $Li_{15}Si_4$). Any two-phase region causes large structural stresses in the electrode, leading to pulverization [111]. Hence, if the voltage is limited to values > 0.050 V, the cyclability of the cell improved as the two-phase region is avoided. This is also believed to be the reason behind the superior performance of amorphous thin film Si anodes over nanocrystalline ones, because in the former, the initial two-phase region (crystalline Si + amorphous lithiated Si) is avoided.

Synthesizing Si anodes with certain nanostructures can lead to improved cycling performance of the cells. Si nanowire architectures[112] have shown good cyclability. Figure 2.8 illustrates how nanowires can (1) improve the contact between active particles and the current collector and (2) help in maintaining the structural integrity of the anode. Similarly, Si anodes with sufficient porosity can also better accommodate the large strains arising from the volume changes during lithiation, and hence provide good reversibility. Porous Si anode structures can be prepared by electrodeposition of Si onto a porous current collector or on to a template [113]. Porous Si deposited on Ni foam current collector showed a stable cycle life of >400 cycles, while providing a reversible capacity of ~500 mAh/g [113].

This research attempts to investigate the effect of porous nanostructure on the cycling performance and the capacity of the Li-ion cell. In particular, our objective is to obtain porous Si anodes with different columnar morphologies. Electrochemical

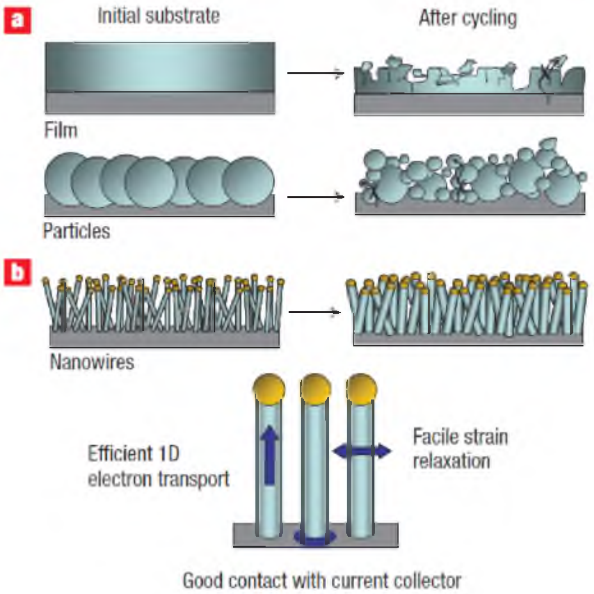

Figure 2.8 Illustration showing how nanowire architecture can better protect the anode material from pulverization during cycling while maintaining electrical contact. Reprinted by permission from Macmillan Publishers Ltd: Nature Nanotechnology, C. K. Chan, Candace, H. Peng, G. Liu, K. McIlwrath, X. F. Zhang, R. A. Huggins, and Y. Cui, High-performance lithium battery anodes using silicon nanowires, Nature Nanotechnology 3(1), 31, 2007[112], copyright 2008.

lithiation/delithiation carried out on these anodes will enable us to investigate the effect of the morphology on cycling performance. Electrochemical etching of Si can be employed to obtain varied morphologies of Si nanostructure.

2.2.4.5 Li-Mg Alloy Anodes

With most of the other metals, Li forms intermetallic compounds which have a high degree of ionic bonding, thus making the compounds brittle and easily susceptible to mechanical degradation [114, 115]. But Mg is one of the very few elements with which Li forms a stable solid solution that is also ductile. The advantage of having a solid solution system is that within a single phase, the volume changes during Li insertion/removal are more continuous and not abrupt as in the intermetallic systems. This can be seen in

Figure 2.9 where the change in volume during formation of LiMg from 1 mole of Mg, is plotted.

In the Li-Mg system at room temperature, the BCC β-phase has a wide compositional range between 11.5 wt.% to 100 wt.% Li (see Figure 2.10). The HCP α-phase is stable between 0 to 5 wt.% Li. Based on the reported lattice parameter for Mg-Li alloy [116], the volume change for insertion of 1 mole of Li into 1 mole of Mg is estimated to be ~85% (Figure 2.9). This is much lower than the corresponding volume change associated with formation of $Li_{22}Sn_5$ and $Li_{15}Si_4$[41], which is 300-400%. The bcc β phase is stable when the Li content in Li-Mg exceeds 11.5 wt% Li. Within this phase, the molar volume initially decreases for Li content between 11 to ~30 wt.% and then starts to increase again.

Dey [49] and Nicholson [55] demonstrated that Li(Mg) alloys can be electrochemically synthesized by reduction of Li on the surface of magnesium substrate. Li alloying of Mg occurred at a potential 0.03 - 0.05 V [49, 117] and the dealloying occurred at 0.2 - 0.4 V with respect to Li^+/Li [55, 117]. Hence, the voltage penalty associated with using Mg as an anode is very low. The alloying results also suggest that it is possible to diffuse Li into Mg at room temperature during charging, which is necessary for cyclability.

Attempts have been made to employ Mg as negative electrode materials in Li-ion batteries [118, 119]. Morales *et al.* [119] experimented with a cell having $LiFePO_4$ as the positive electrode and a Li deposit on Mg film, acting as the anode. This cell showed higher capacities during charge cycling, than a cell with pure Li anode. It is suggested that a thinner solid electrolyte interface (SEI) layer on the Li(Mg) surface and the clean Li/Mg interface, acting as an efficient current collector, are responsible for the good

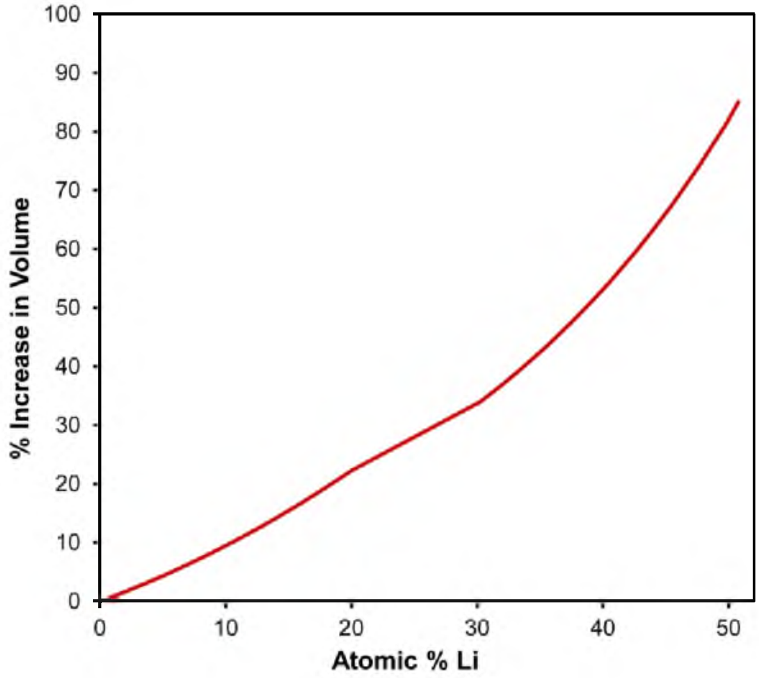

Figure 2.9 Increase in volume during lithiation of 1 mole Mg as a function of Li content.

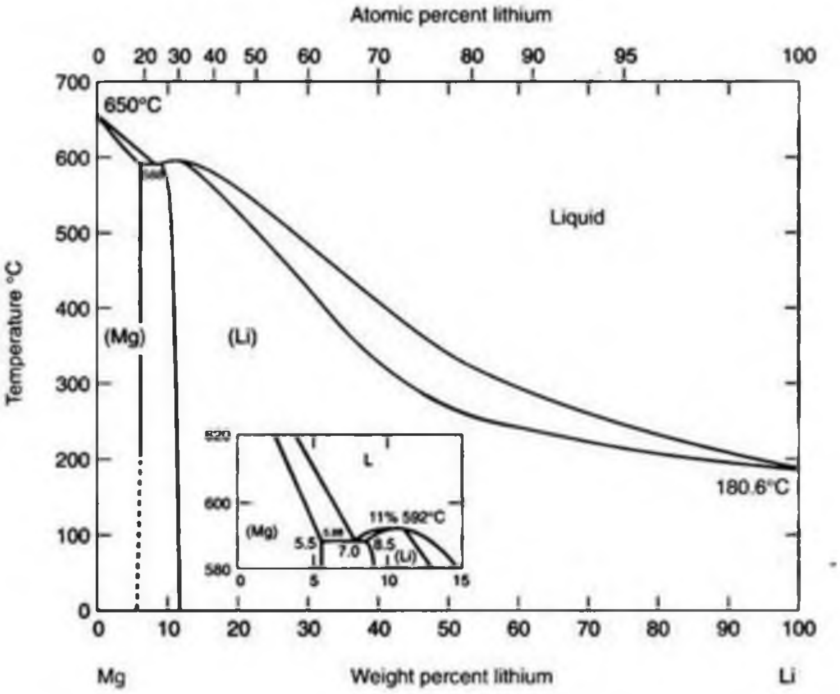

Figure 2.10 Lithium magnesium phase diagram. Reprinted from H. Baker, and H. Okamoto, ASM handbook, Alloy phase diagrams 3(2), 2.276, 1992 [120]. Reprinted with permission of ASM International. All rights reserved. www.asminternational.org

cycling performance.

The reported values of diffusivity of Li^+ ion in the Li(Mg) β-phase (~ 10^{-7} cm^2/s) are much higher than in other intermetallic alloys (e.g., in LiAl, it is 6 x 10^{-10} cm^2/s) [117]. Consequently, the dendrite formation at the surface of the electrode during recharging could be less, thus potentially improving the cyclability and capacity retention of the cell. In a preliminary work, Richardson *et al.* [121] observed that the surfaces of charged Li(Mg) alloy anodes were free of dendrites.

The diffusivity of Li in the HCP α-phase is reported to be several orders of magnitude lower than in the β-phase [122]. Hence, the lithiation and delithiation kinetics on a single phase β-Li(Mg) alloy anode will be more favorable than pure Mg anodes. The objective of this study is to synthesize such Li(Mg) alloys and to examine the charge discharge characteristics on these alloy anodes. During continuous Li extraction, a Li(Mg) β-phase should gradually transform into Mg rich α-phase. However, this phase transition at room temperature is to yet to be convincingly shown to occur throughout the bulk of the electrode. A detailed study of Li-Mg alloy as anode for reversible Li insertion and extraction is one of the objectives of this research.

2.2.4.6 Relative Comparison of Alloy Anode Systems

To summarize our discussion on the alloy anodes, a side-by-side comparison of some important properties of the common alloy systems can be made. Figures 2.11 (a) and 2.11(b) show the gravimetric capacities of initial material and the volumetric capacities of the lithiated phases, respectively. Metallic Li and graphite are also included for reference. For the case of Mg anode, Li_3Mg, lying in the single β-phase region, was arbitrarily chosen as the final lithiated phase. It can be seen that Si can theoretically

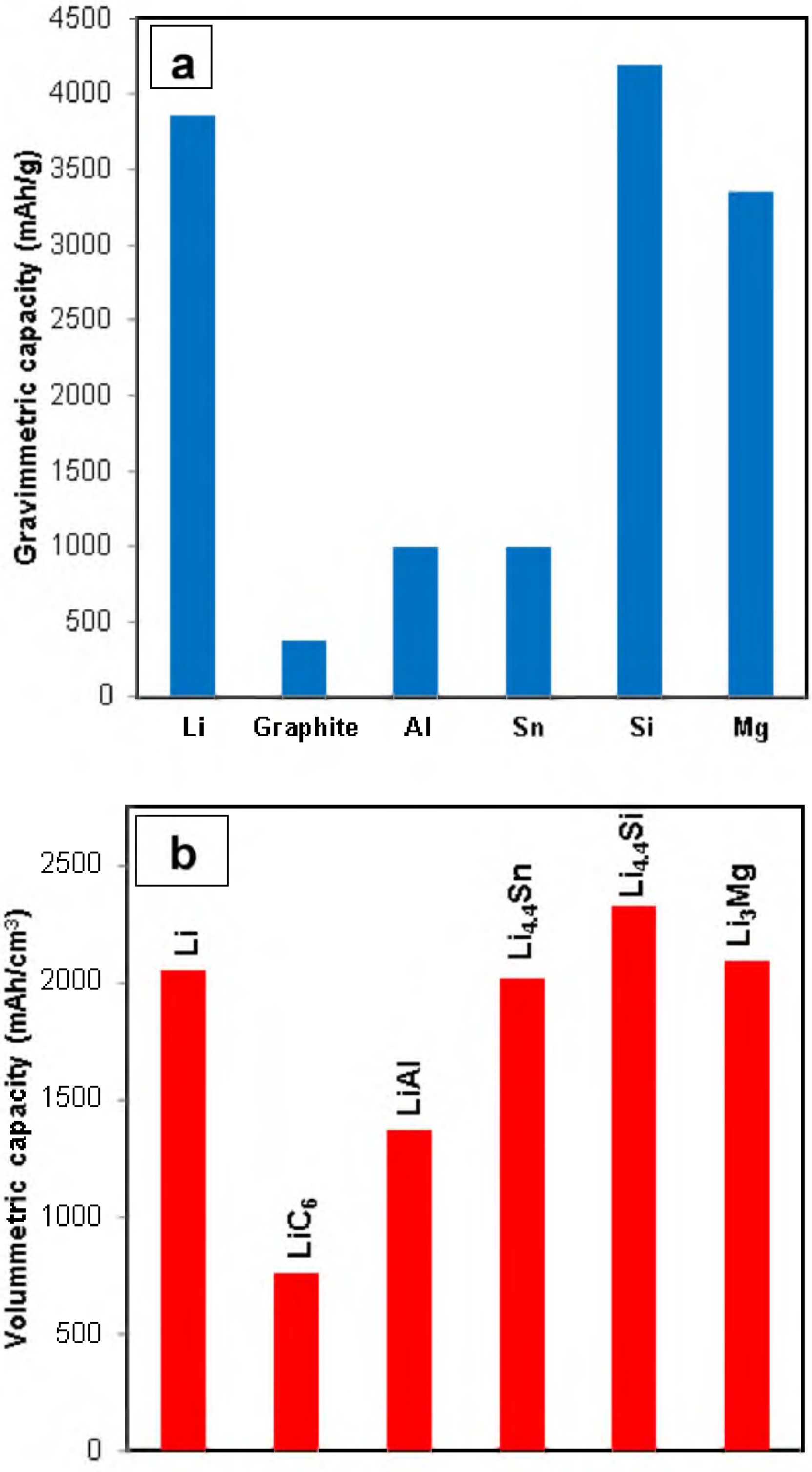

Figure 2.11 Capacities of different anode materials. The theoretical gravimetric capacities are shown in (a) whereas (b) shows the volumetric capacities of the anodes.

provide specific capacities higher than even that of metallic Li. The gravimetric and volumetric capacities of graphite are much lower, when compared with other anodes. The volumetric capacities of Sn, Si and Mg are comparable with that of Li.

The volumes of the anode materials before and after Li insertion are compared in Figure 2.12. These volumes are normalized for storage of 1 mol Li, i.e., their initial volume is adjusted so that it can accommodate 1 mole of Li in its final lithiated phase. The initial volume of graphite anode required is the highest, since it has the lowest Li uptake capacity (only 1 mol of Li for 6 moles of C). But it also has the minimum change in volume after lithiation, about 10%. The maximum volume changes occur during the formation of $Li_{22}Sn_5$ (260%) or $Li_{22}Si_5$ (320%). In LiAl, there is a change of 100% and in Li_3Mg, about 175%.

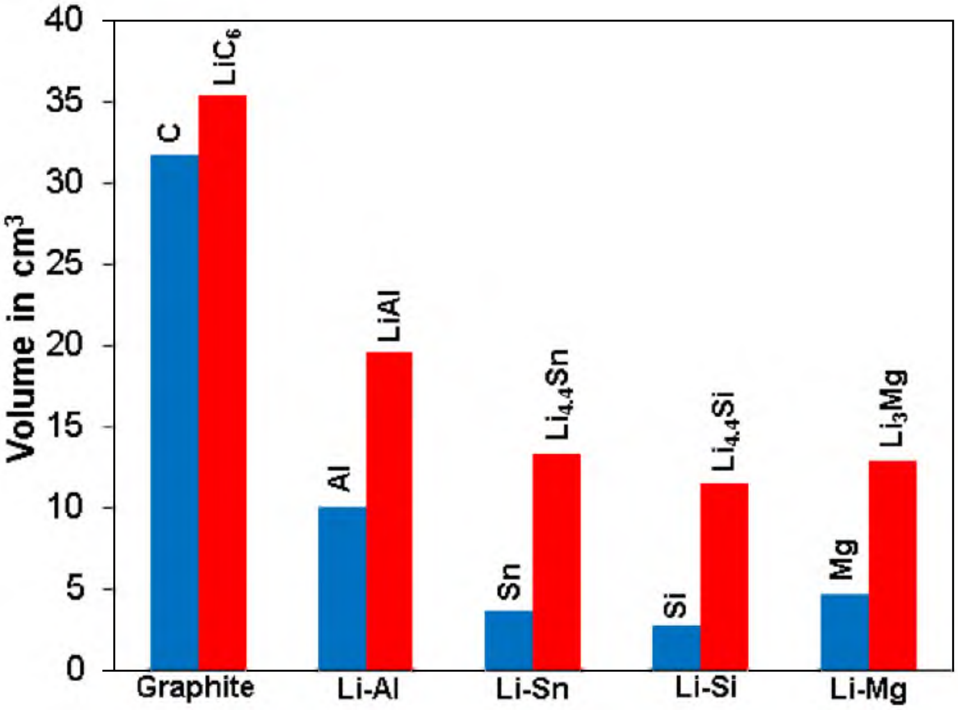

Figure 2.12 Volume of anode materials before and after lithiation. The initial volumes are normalized for storage of 1 mol Li.

2.3 Electrochemical Modeling in Li-ion Cells

Mathematical modeling of electrochemical behavior of Li-ion cells, in particular the charge discharge characteristics, will be extremely helpful in understanding the potential and limitations of various physical, chemical and transport processes involved. In particular, it is important to examine the following questions:

1. How does Li insertion and removal occur within electrodes under the governing potentials? Does this process occur under largely equilibrium or nonequilibrium conditions, in terms of phase transformations within the electrode?
2. How do the phase transformations and the associated phase boundary movement affect the Li insertion and removal at various C rates?
3. How can the diffusion and electrochemical over potentials be included in the modeling to reflect the actual cell behavior under various charge/discharge conditions?

It is recognized that to address the above questions, we need to develop a clean modeling approach that includes (1) phase transformation and phase boundary movement within electrodes, (2) appropriate flux or concentration boundary conditions at the surfaces/interfaces and (3) charge transfer (Butler-Volmer) kinetics at the electrode-electrolyte interfaces and (4) mass transfer over potentials in the electrolyte and within the electrodes.

The objective of this research is to develop a comprehensive mathematical model that can faithfully reflect the physical, chemical and transport processes that occur within the electrode under any external charge/discharge conditions. First, the prior work in this area is reviewed in the following section.

2.3.1 Review of Prior Modeling Research

Doyle *et al.* [123] first developed a model to predict the cell voltage during galvanostatic charge/discharge in Li-ion cells consisting of Li metal anode, solid polymer separator and an insertion composite cathode. The simulation data obtained by this model matched experimental results under isothermal conditions. An energy balance was later added to this model in order to account for the temperature changes within the cell during charge-discharge[124, 125]. In these models, the Li^+ ion transport through electrolyte is addressed using the concentrated solution theory and the porous electrode theory is used to describe Li transport through the composite cathode.

As far as describing Li insertion through electrodes is concerned, the porous electrode theory, first proposed by Newman [125], is the most widely used approach. In this theory, the electrode was assumed to consist of spherical particles coated with the conductive additives on the surface, as shown in Figure 2.13. The Li transport in the separator was modeled with the concentrated solution theory which takes into account the transport of both Li^+ and X^- ions in the electrolyte containing LiX salts. The liquid electrolyte was treated as a nonideal solution [126]. Butler-Volmer type expressions were used to relate the current to the potential difference across the electrode-electrolyte interfaces. Ohm's law was used to predict the potential variation within the solid phases and the solutions. The transport of Li into the electrode particles was treated as a purely chemical diffusion problem [128]. The mass transport in the solid electrode is solved using Fickian diffusion equations in spherical coordinates [125]. It was also assumed that due to porosity, the electrolyte has access to each spherical particle within the electrode

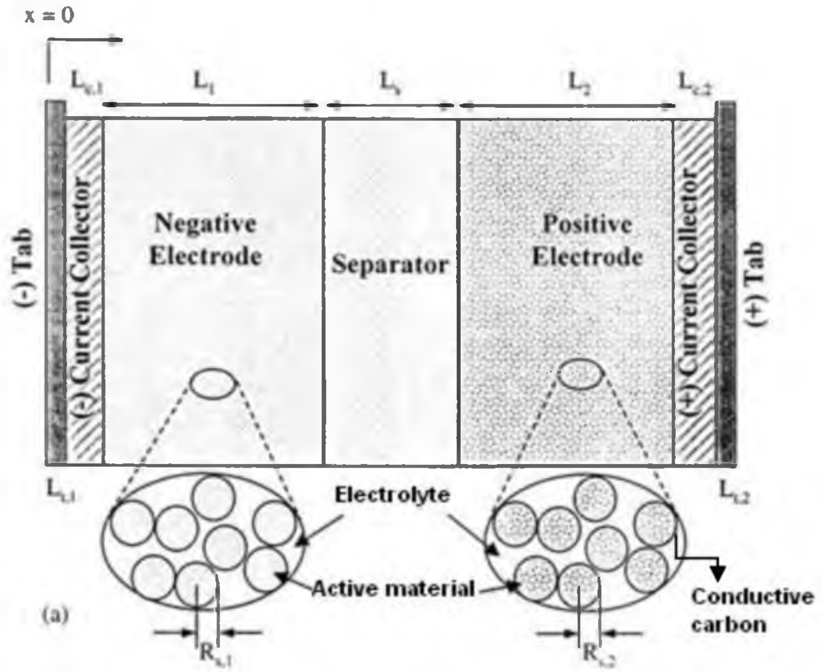

Figure 2.13 Schematic of a cell with porous electrodes consisting of spherical particles coated with conductive carbon additives[127]. Reprinted from Electrochimica Acta, 45(15), G. G. Botte, V. R. Subramanian, and R. E. White, Mathematical modeling of secondary lithium batteries, 2595-2609, 2000. Copyright 2000, with permission from Elsevier.

simultaneously.

First, in many Li-ion cells, planar or rolled batteries [126], the assumption of spherical particles in electrode is not valid. Secondly, the electrolyte does not have access to all the particles within the electrode, but only to particles close to the interface. This is important because if the electrolyte has access to particles, then the Li insertion and removal will be controlled by transport within the electrolyte. On the other hand, if this is not the case, Li transport must occur through solid state diffusion and hence, the kinetics of phase boundary movement between lithiated and unlithiated regions becomes important. Also, the modeling of nonporous electrodes is of great interest for thin film microbatteries, especially all solid-state batteries. In such cases, no electrolyte, binder or filler is assumed to be present inside the electrode[129] and the ionic transport occurs in a planar fashion.

Danilov *et al.* [130] used a planar approach to model the behavior of all solid-state thin film batteries comprising of Li metal anode and $LiCoO_2$ cathode. The model considered charge transfer kinetics at the electrode/electrolyte interface, diffusion of Li in the intercalation electrode and diffusion and migration of ions through the electrolyte. A Nernst-Planck approach, which was earlier developed for liquid electrolytes [131], was used to model the diffusion and migration of Li^+ ions through the solid electrolyte. Boundary conditions of constant flux on one side and zero flux on the other side of the cathode were imposed to solve for diffusional mass transport within the $LiCoO_2$ thin film cathode. However, this model did not take into account the phase transitions occurring in the $LiCoO_2$ electrode.

Zhang *et al.* [132] developed a moving boundary model to include phase-transformation in $LiCoO_2$ electrode during Li insertion in particles. Lithiation was assumed to begin on single phase α-$LiCoO_2$ particle, with Li diffusing inward from the surface. Further insertion leads to the formation of a thin Li-rich β-phase shell surrounding the α-phase particles. This phase boundary moves toward the center of the spherical particle until the entire α-core is transformed to β-phase. Similarly, Srinivasan *et al.*[133] developed a shrinking core model for Li insertion in $LiFePO_4$ particles. Unlike the moving boundary model, here it was assumed that a shell of Li-rich phase immediately formed outside the core, i.e., a two-phase region is present from the beginning of the lithiation.

While these models may adequately describe lithiation of a particle, lithiation of electrode as a whole can be described only by a mesoscopic approach where consideration to planar boundary movement in electrode is essential for a proper description of lithiation process. This is yet to be done.

In any model, once the governing partial differential equations for mass transport of Li are set up, they can be solved by different techniques. It is highly desirable to solve these equations analytically [134]. This is because analytical solutions are continuous in time and space and hence, explicitly reveal the effect of various parameters on Li insertion and removal. Classical analytical techniques that enable closed form solution to diffusional transport include Laplace transformation, separation of variables, Green's function, Duhamel superposition and the method of images, etc [127]. For models based on the porous electrode theory, the governing equations cannot be solved analytically. The most commonly used method is the BAND subroutine developed by Newman [125], a numerical solution technique for solving boundary value problems that consist of coupled, ordinary differential equations.

The objective of this research is to create a mesoscopic modeling framework where analytical solutions to diffusion equations, taking into account moving phase boundaries within nonporous electrodes, will be derived ,for Li insertion and removal processes. The diffusion equations will be solved for planar geometries, unlike the previous modeling efforts which mostly considered spherical particles. In particular, appropriate flux/concentration boundary conditions, phase boundary movement and charge transfer at the electrode/electrolyte interfaces are key physical aspects that should be included in a consistent manner. The migration and diffusion of Li^+ ions within the electrolyte also need to be taken into account.

The objective is to develop a computational scheme, that directly incorporates the physical processes in electrode and that can be adopted to simulate the charge-discharge behavior of Li-ion batteries in a realistic way. This model is particularly relevant for thin-film batteries, all solid-state batteries and nonporous electrodes. This model will be more direct, intuitive and can be adopted to simulate the charge-discharge behavior of Li-ion batteries.

2.4 References

1. A. Manthiram, *The Journal of Physical Chemistry Letters*, **2**, 176.
2. D. Aurbach, *Journal of The Electrochemical Society*, **136**, 906 (1989).
3. D. Aurbach, *Journal of The Electrochemical Society*, **136**, 1606 (1989).
4. D. Aurbach, *Journal of The Electrochemical Society*, **136**, 1611 (1989).
5. D. Aurbach, M. L. Daroux, P. W. Faguy and E. Yeager, *Journal of The Electrochemical Society*, **134**, 1611 (1987).
6. D. Aurbach, M. L. Daroux, P. W. Faguy and E. Yeager, *Journal of The Electrochemical Society*, **135**, 1863 (1988).
7. D. Aurbach, Y. Gofer and J. Langzam, *Journal of The Electrochemical Society*, **136**, 3198 (1989).
8. D. Aurbach and H. Gottlieb, *Electrochimica Acta*, **34**, 141 (1989).
9. K. M. Abraham, S. Subbarao, V. R. Kock, B. B. Owens and H. Smyrl, *Rechargeable Lithium Batteries* p. 1, Pennington, NJ (1990).
10. D. Aurbach, E. Zinigrad, Y. Cohen and H. Teller, *Solid State Ionics*, **148**, 405 (2002).
11. J. M. Tarascon and M. Armand, *Nature*, **414**, 359 (2001).
12. W. J. Zhang, *Journal of Power Sources*, **196**, 13 (2011).
13. T. Nagaura, A lithium-ion battery, in *The Third International Rechargeable Battery Seminar*, Deerfield Beach, FL (March 5-7, 1990).
14. T. Nagaura and K. Tozawa, *Prog. Batteries Solar Cells*, **9**, 209 (1990).

15. M. Wachtler, J. O. Besenhard and M. Winter, *Journal of Power Sources*, **94**, 189 (2001).

16. R. Yazami and P. Touzain, *Journal of Power Sources*, **9**, 365 (1983).

17. J. O. Besenhard, J. Yang and M. Winter, *Journal of Power Sources*, **68**, 87 (1997).

18. J. B. Goodenough and Y. Kim, *Chemistry of Materials*, **22**, 587 (2009).

19. B. Huang, Y. I. Jang, Y. M. Chiang and D. R. Sadoway, *Journal of Applied Electrochemistry*, **28**, 1365 (1998).

20. M. Winter, J. O. Besenhard, M. E. Spahr and P. Novak, *Advanced Materials*, **10**, 725 (1999).

21. A. K. Shukla and T. Prem Kumar, *Current Science*, **94**, 314 (2008).

22. Y. Tang, L. Yang, Z. Qiu and J. Huang, *Journal of Materials Chemistry*, **19**, 5980 (2009).

23. I. Belharouak, Y. K. Sun, W. Lu and K. Amine, *Journal of The Electrochemical Society*, **154**, A1083 (2007).

24. P. Poizot, S. Laruelle, S. Grugeon, L. Dupont and J. M. Tarascon, *Nature*, **407**, 496 (2000).

25. M. R. Palacin, *Chemical Society Reviews*, **38**, 2565 (2009).

26. H. J. Ahn, K. W. Kim and J. H. Ahn, *Encyclopedia of Power Sources*, Elsevier, Amsterdam, The Netherlands (2009).

27. X. Ji and L. F. Nazar, *J. Mater. Chem.*, **20**, 9821.

28. F. Croce, G. B. Appetecchi, L. Persi and B. Scrosati, *Nature*, **394**, 456 (1998).

29. S. S. Jeong, Y. T. Lim, Y. J. Choi, G. B. Cho, K. W. Kim, H. J. Ahn and K. K. Cho, *Journal of Power Sources*, **174**, 745 (2007).

30. J. Hassoun and B. Scrosati, *Advanced Materials*, **22**, 5198.

31. T. Takeuchi, H. Sakaebe, H. Kageyama, H. Senoh, T. Sakai and K. Tatsumi, *Journal of Power Sources*, **195**, 2928 (2010).

32. X. Ji, K. T. Lee and L. F. Nazar, *Nature Materials*, **8**, 500 (2009).

33. D. Aurbach, E. Pollak, R. Elazari, G. Salitra, C. S. Kelley and J. Affinito, *Journal of The Electrochemical Society*, **156**, A694 (2009).

34. J. Hassoun and B. Scrosati, *Angewandte Chemie International Edition*, **49**, 2371.

35. J. Hassoun, Y. K. Sun and B. Scrosati, *Journal of Power Sources*, **196**, 343.

36. Y. Yang, M. T. McDowell, A. Jackson, J. J. Cha, S. S. Hong and Y. Cui, *Nano Letters*, **10**, 1486 (2010).

37. B. Scrosati, J. Hassoun and Y. K. Sun, *Energy & Environmental Science*, **4**, 3287.

38. K. M. Abraham, Z. Jiang and B. Carroll, *Chemistry of Materials*, **9**, 1978 (1997).

39. S. J. Visco, E. Nimon and L. C. De Jonghe, *Elsevier*, **4**, 376 (2009).

40. B. Kumar, J. Kumar, R. Leese, J. P. Fellner, S. J. Rodrigues and K. M. Abraham, *Journal of The Electrochemical Society*, **157**, A50.

41. M. Winter and J. O. Besenhard, *Electrochim. Acta*, **45**, 31 (1999).

42. J. S. Dunning, W. H. Tiedemann, L. Hsueh and D. N. Bennion, *Journal of The Electrochemical Society*, **118**, 1886 (1971).

43. M. L. B. Rao, *Journal of The Electrochemical Society*, **114**, 665 (1967).

44. N. P. Yao, E. D'Orsay and D. N. Bennion, *Journal of The Electrochemical Society*, **115**, 999 (1968).

45. A. N. Dey, *Journal of The Electrochemical Society*, **114**, 823 (1967).

46. H.F. Baumann, J.E. Shilton, W.J. Conner and G.M. Cook, *New cathode anode couples using nonaqueous electrolyte*, in Project No. 8173, Lockheed Missiles and Space Co, Palo Alto (1963).

47. R.G. Selim, K.R. Hill and M. L. B. Rao, *Research and development of a high capacity nonaqueous secondary battery*, in P.R. Mallory and Co., Burlington (1965).

48. K.H.M. Braeuer and J. A. Harvey, Status report on organic electrolyte high energy density batteries, in US Army Electronics Command, Fort Monmouth, NJ (1967).

49. A. N. Dey, *Journal of The Electrochemical Society*, **118**, 1547 (1971).

50. J. O. Besenhard and H. P. Fritz, *Electrochimica Acta*, **20**, 513 (1975).

51. H.P. Fritz and J. O. Besenhard, US Patent 3,960,594 (1976).

52. J. O. Besenhard, *Journal of Electroanalytical Chemistry and Interfacial Electrochemistry*, **94**, 77 (1978).

53. B. M. L. Rao, R. W. Francis and H. A. Christopher, *Journal of The Electrochemical Society*, **124**, 1490 (1977).

54. J. O. Besenhard, *Journal of Electroanalytical Chemistry and Interfacial Electrochemistry*, **78**, 189 (1977).

55. M. M. Nicholson, *Journal of The Electrochemical Society*, **121**, 734 (1974).

56. M. M. Nicholson, in *Fall Meeting of the Electrochemical Society*, Miami Beach, FL (1972).

57. J. Antaul and B.F. Becker, *J. Phys. Chem.*, **79** (1975).

58. D. Sam and J.H. Ambrus, in *Fall Meeting of the Electrochemical Society*, p. 57, New York (1974).

59. D. Fauteux and R. Koksbang, *Journal of Applied Electrochemistry*, **23**, 1 (1993).

60. R. A. Huggins, *Journal of Power Sources*, **22**, 341 (1988).

61. R. A. Huggins, *Journal of Power Sources*, **26**, 109 (1989).

62. J. O. Besenhard and G. Eichinger, *Journal of Electroanalytical Chemistry and Interfacial Electrochemistry*, **68**, 1 (1976).

63. D. Rahner, S. Machill, H. Schlorb, K. Siury, M. Kloss and W. Plieth, *Journal of Solid State Electrochemistry*, **2**, 78 (1998).

64. D. Rahner, S. Machill and K. Siury, *Solid State Ionics*, **86**, 925 (1996).

65. Y. Toyoguchi, S. Nankai, J. Yamaura, T. Matsui and T. Ijima, in *Extended Abstracts*, p. 205 (1983).

66. K. Nishio, N. Furukawa and J. O. Besenhard, *Handbook of Battery Materials*, Wiley-VCH, New York (1999).

67. A. Anani and R. A. Huggins, *Journal of Power Sources*, **38**, 351 (1992).

68. R. Huggins, *Advanced Batteries: Materials Science Aspects*, Springer, New York (2009).

69. R. A. Huggins, *Journal of Power Sources*, **81**, 13 (1999).

70. N. Sharma, J. Plevert, G. V. S. Rao, B. V. R. Chowdari and T. J. White, *Chemistry of Materials*, **17**, 4700 (2005).

71. M. Armand, *Solid State Ionics*, **9**, 745 (1983).

72. M. Gauthier, in *3rd International Meeting on Lithium Batteries*, Kyoto, Japan (1986).

73. C. J. Wen, B. A. Boukamp, R. A. Huggins and W. Weppner, *Journal of The Electrochemical Society*, **126**, 2258 (1979).

74. N. P. Yao, L. A. Heredy and R. C. Saunders, *Journal of The Electrochemical Society*, **118**, 1039 (1971).

75. A. J. McAlister, *Journal of Phase Equilibria*, **3**, 177 (1982).

76. Y. Hamon, T. Brousse, F. Jousse, P. Topart, P. Buvat and D. M. Schleich, *Journal of Power Sources*, **97**, 185 (2001).

77. D. Larcher, L. Y. Beaulieu, O. Mao, A. E. George and J. R. Dahn, *Journal of The Electrochemical Society*, **147**, 1703 (2000).

78. M. J. Lindsay, G. X. Wang and H. K. Liu, *Journal of Power Sources*, **119**, 84 (2003).

79. J. O. Besenhard, M. Hess and P. Komenda, *Solid State Ionics*, **40**, 525 (1990).

80. Y. Geronov, P. Zlatilova and R. V. Moshtev, *Journal of Power Sources*, **12**, 145 (1984).

81. M. Garreau, J. Thevenin and M. Fekir, *Journal of Power Sources*, **9**, 235 (1983).

82. W. C. Maskell and J. R. Owen, *Journal of The Electrochemical Society*, **132**, 1602 (1985).

83. A. S. Baranski, W. R. Fawcett, T. Krogulec and M. Drogowska, *Journal of The Electrochemical Society*, **131**, 1750 (1984).

84. M. Maxfield, T. R. Jow, S. Gould, M. G. Sewchok and L. W. Shacklette, *Journal of The Electrochemical Society*, **135**, 299 (1988).

85. T. R. Jow and C. C. Liang, *Journal of The Electrochemical Society*, **129**, 1429 (1982).

86. Y. Idota, T. Kubota, A. Matsufuji, Y. Maekawa and T. Miyasaka, *Science*, **276**, 1395 (1997).

87. C. J. Wen and R. A. Huggins, *Journal of The Electrochemical Society*, **128**, 1181 (1981).

88. C. J. Wen and R. A. Huggins, *Journal of Solid State Chemistry*, **35**, 376 (1980).

89. J. Sangster and C. W. Bale, *Journal of Phase Equilibria*, **19**, 70 (1998).

90. I. A. Courtney and J. R. Dahn, *Journal of The Electrochemical Society*, **144**, 2045 (1997).

91. J. Wang, I. D. Raistrick and R. A. Huggins, *Journal of The Electrochemical Society*, **133**, 457 (1986).

92. W. J. Zhang, *Journal of Power Sources*, **196**, 877 (2011).

93. J. R. Dahn, I. A. Courtney and O. Mao, *Solid State Ionics*, **111**, 289 (1998).

94. M. Wachtler, M. Winter and J. O. Besenhard, *Journal of Power Sources*, **105**, 151 (2002).

95. P. P. Ferguson, R. A. Dunlap and J. R. Dahn, *Journal of The Electrochemical Society*, **157**, A326 (2010).

96. J. Yang, M. Winter and J. O. Besenhard, *Solid State Ionics*, **90**, 281 (1996).

97. J. Yang, M. Wachtler, M. Winter and J. O. Besenhard, *Electrochemical and Solid-State Letters*, **2**, 161 (1999).

98. A. D. W. Todd, R. E. Mar and J. R. Dahn, *Journal of The Electrochemical Society*, **153**, A1998 (2006).

99. S. Mizutani and H. Inoue, U.S. Patent Application 10/519,898 (2004).

100. R. A. Sharma and R. N. Seefurth, *Journal of The Electrochemical Society*, **123**, 1763 (1976).

101. B. A. Boukamp, G. C. Lesh and R. A. Huggins, *Journal of The Electrochemical Society*, **128**, 725 (1981).

102. C. Van der Marel, G. J. B. Vinke and W. Van der Lugt, *Solid State Communications*, **54**, 917 (1985).

103. J. H. Ryu, J. W. Kim, Y. E. Sung and S. M. Oh, *Electrochemical and Solid-State Letters*, **7**, A306 (2004).

104. W. R. Liu, Z. Z. Guo, W. S. Young, D. T. Shieh, H. C. Wu, M. H. Yang and N. L. Wu, *Journal of Power Sources*, **140**, 139 (2005).

105. Z. P. Guo, J. Z. Wang, H. K. Liu and S. X. Dou, *Journal of Power Sources*, **146**, 448 (2005).

106. H. Li, X. Huang, L. Chen, Z. Wu and Y. Liang, *Electrochemical and Solid-State Letters*, **2**, 547 (1999).

107. J. Graetz, C. C. Ahn, R. Yazami and B. Fultz, *Electrochemical and Solid-State Letters*, **6**, A194 (2003).

108. T. Takamura, S. Ohara, M. Uehara, J. Suzuki and K. Sekine, *Journal of Power Sources*, **129**, 96 (2004).

109. P. Limthongkul, Y. I. Jang, N. J. Dudney and Y. M. Chiang, *Journal of Power Sources*, **119**, 604 (2003).

110. P. Limthongkul, Y. I. Jang, N. J. Dudney and Y. M. Chiang, *Acta Materialia*, **51**, 1103 (2003).

111. U. Kasavajjula, C. Wang and A. J. Appleby, *Journal of Power Sources*, **163**, 1003 (2007).

112. C. K. Chan, H. Peng, G. Liu, K. McIlwrath, X. F. Zhang, R. A. Huggins and Y. Cui, *Nature Nanotechnology*, **3**, 31 (2007).

113. M. Yoshio, T. Tsumura and N. Dimov, *Journal of Power Sources*, **146**, 10 (2005).

114. R. Nesper, *Prog. Solid State Chem.*, **20**, 1 (1990).

115. R. Nesper, *Angew. Chem. Intl. Ed. Engl.*, **30**, 789 (1991).

116. R. S. Busk, *Trans. Metall. Soc. AIME*, **188**, 1460 (1950).

117. Z. Shi, M. Liu, D. Naik and J. L. Gole, *Journal of Power Sources*, **92**, 70 (2001).

118. H. Kim, B. Park, H.-J. Sohn and T. Kang, *J. Power Sources*, **90**, 59 (2000).

119. J. Morales, R. Trocoli and J. Santos-Pena, *Electrochem. Solid-State Lett.*, **12**, A145 (2009).

120. H. Baker and H. Okamoto, *Alloy Phase Diagrams*, **3**, 2 (1992).

121. T. J. Richardson and G. Chen, *J. Power Sources*, **174**, 810 (2007).

122. Y. Iwadate, M. Lassouani, F. Lantelme and M. Chemla, *J. Appl. Electrochem.*, **17**, 385 (1987).

123. M. Doyle, T. F. Fuller and J. Newman, *Journal of The Electrochemical Society*, **140**, 1526 (1993).

124. L. Song and J. W. Evans, *Journal of The Electrochemical Society*, **147**, 2086 (2000).

125. J. S. Newman and K. E. Thomas-Alyea, *Electrochemical Systems*, Wiley Hoboken, NJ (2004).

126. W. Lai and F. Ciucci, *Electrochimica Acta*, **56**, 4369.

127. G. G. Botte, V. R. Subramanian and R. E. White, *Electrochimica Acta*, **45**, 2595 (2000).

128. P. M. Gomadam, J. W. Weidner, R. A. Dougal and R. E. White, *Journal of Power Sources*, **110**, 267 (2002).

129. K. Thomas, J. Newman and R. Darling, in *Advances in Lithium-Ion Batteries*, p. 345, Springer, New York (2002).

130. D. Danilov, R. A. H. Niessen and P. H. L. Notten, *Journal of The Electrochemical Society*, **158**, A215 (2011).

131. D. Danilov and P. H. L. Notten, *Electrochimica Acta*, **53**, 5569 (2008).

132. Q. Zhang and R. E. White, *Journal of The Electrochemical Society*, **154**, A587 (2007).

133. V. Srinivasan and J. Newman, *Journal of The Electrochemical Society*, **151**, A1517 (2004).

134. J. Newman and W. Tiedemann, *AIChE Journal*, **21**, 25 (2004).

CHAPTER 3

ELECTROCHEMICAL CHARGE/DISCHARGE BEHAVIOR AND PHASE TRANSITIONS DURING CELL CYCLING OF LI(MG) ALLOY ANODES FOR HIGH CAPACITY LI-ION BATTERIES

Published as:

M. Jagannathan and K.S. Ravi Chandran

Electrochemical Charge/Discharge Behavior and Phase Transitions During Cell Cycling of Li(Mg) Alloy Anodes for High Capacity Li Ion Batteries

Journal of The Electrochemical Society, 2013, Vol. 160 (10), pp. A1922-1926.

Journal of The Electrochemical Society, **160** (10) A1922-A1926 (2013)
0013-4651/2013/160(10)/A1922/5/$31.00 © The Electrochemical Society

Electrochemical Charge/Discharge Behavior and Phase Transitions during Cell Cycling of Li(Mg) Alloy Anodes for High Capacity Li Ion Batteries

M. Jagannathan[z] and K. S. Ravi Chandran

Department of Metallurgical Engineering, University of Utah, Salt Lake City, Utah 84112, USA

Electrochemical performance of Li(Mg) alloys as potential negative electrodes for Li-ion batteries has been investigated. Two Li(Mg) alloys with nominal compositions, Li-60 wt% Mg (Li_7Mg_3) and Li-30 wt% Mg (Li_8Mg) were synthesized and electrodes were prepared by melting, rolling and annealing. Both the alloys showed a discharge plateau voltage of ~2 V compared to the ~2.5 V with pure Li anode with reference to MnO_2 as cathode. Detailed ex situ X-ray diffraction analysis revealed that during the discharge of Li(Mg) anodes, a gradual phase transformation, from the BCC Li(Mg) β-phase to the HCP Mg(Li) α-phase, occurred in the electrodes. An intriguing finding is that the Li-depleted Li(Mg) anode was largely intact as solid electrode even after delithiation. The Li(Mg) electrode showed some degree of reversibility (against $LiCoO_2$), possibly by a combination of a small amount of Li alloying and/or deposition at the electrode-electrolyte interface during charging, a promising aspect for further investigation.
[DOI: 10.1149/2.006311jes]

Manuscript submitted June 10, 2013; revised manuscript received August 21, 2013. Published September 6, 2013.

It is well known[1–6] that Li alloy anodes, especially Si, Sn, and Sb as negative electrode materials, are highly desirable for rechargeable lithium-ion batteries because of their high theoretical specific capacities (4200, 994 and 660 mAh/g for Si, Sn, and Sb respectively). However, the volume changes associated with insertion/removal of Li in these alloys are substantial—the insertion of 1 mole of Li into graphite causes a volume change of only 8% but the volume change in the case of Si is ~300% (for $Li_{22}Si_5$) and ~250% for Sn ($Li_{22}Sn_5$).[5] The high volume changes lead to cracking and crumbling of the electrode and consequently diminish the conductive pathways within the electrode. However, recent researches with nanoparticle Si electrodes show significantly improved performances and promise for practical electrodes.[7]

As potential negative electrodes, Li(Mg) alloys are quite intriguing. First, Li and Mg share a diagonal relationship in the periodic table and have comparable atomic radii, leading to extended solid solubility[8]—a single BCC phase solid solution alloys exists over 11.5–100 wt% Li in Li(Mg). This is unlike other anode materials (e.g. Si, Sn), where Li actually forms intermetallic compounds of the type Li_xM_y which have a high degree of ionic bonding, and are hence brittle and fragile.[9,10] The Li-Mg BCC solid solution can act as a scaffold-like structure that might facilitate insertion and removal of Li^+ ions during charge/discharge cycling. The volume change for the insertion of 1 mole of Li into Mg is estimated to be ~80% using Li(Mg) alloy lattice parameters.[11] This is much lower than that arising from Li reaction with Sn, Sb, and Si.[5] Additionally, BCC Li(Mg) alloys are very ductile allowing straight-forward fabrication of electrodes by rolling and annealing. In encouraging preliminary studies, Dey,[12] Nicholson,[13] Shi et al[14] and Kim et al[15] demonstrated electrochemically that Li alloying with Mg occurred at a potential of 0.015–0.05 V and the dealloying occurred at a potential of 0.2–0.4 V, with respect to Li/Li^+. This suggests that a Li(Mg) electrode may provide voltages similar to those offered by graphite electrodes while offering much higher practical specific capacities (e.g. 1930 mAh/g for Li-50 wt%Mg alloy). Based on these findings, it is of interest to systematically evaluate the potential of Li-Mg alloys as negative electrodes in Li-ion batteries.

The primary objective of this research is to completely characterize the electrochemical performance and the associated electrode phase transitions during Li insertion/removal in Li(Mg) negative electrodes. The work is also motivated by the encouraging values of diffusivity of Li^+ ion in the Li(Mg) β-phase (~10^{-7} cm^2/s)[14] which are much higher than that in other intermetallic alloys (e.g. in LiAl, it is 6×10^{-10} cm^2/s). Also, the continuous electrochemical Li extraction during discharge should cause the Li(Mg) β-phase to gradually transform into Mg rich α-phase. This phase transition and the corresponding structural/mechanical state of electrode after Li removal are yet to be convincingly demonstrated. We have also further investigated the extent of cyclability of Li(Mg) electrode against $LiCoO_2$ which shows some promising results.

Materials and Experimental Procedure

The Li(Mg) alloys were fabricated by gradually adding 99.5% pure magnesium chips (US Magnesium LLC, Salt Lake City, UT) to a lithium melt, obtained by melting rods of 99.9% Li (ESPI metals, Ashland, OR). Since both Li and Mg readily react with air and moisture, the alloy synthesis was carried out in a glove box under argon atmosphere. Li rods, received in Ar-sealed cans, were opened inside the glove box. The weighed pieces of ingots were melted in a stainless steel crucible and a melt temperature of about 220°C was maintained. Mg pieces, chopped into a few mm sized granules, were added gradually to the molten Li. The molten Li was continually stirred while the Mg pieces were added in order to aid alloy formation. At the same time, the melt temperature was increased to a value at least 50°C higher than the liquidus temperature of the alloy at the required composition. After several trials, two alloy compositions: Li-60 wt% Mg (Li_7Mg_3) and Li-30 wt% Mg (Li_8Mg) were successfully synthesized. X-ray diffraction and ICP-AES analyzes were performed to assess their homogeneity and composition.

For electrochemical testing, the alloys were rolled to foils of thickness 0.35 mm, which were then annealed under argon gas atmosphere at 100°C for 24 hours. Electrodes, punched from the sheets of MnO_2 (ratio of active-material:carbon:PVDF-binder as 0.80:0.1:0.1) and $LiCoO_2$ (ratio of active-material:carbon:PVDF-binder as 0.85:0.1:0.05) were used as positive electrodes in discharge and cell cycle tests, respectively. A polypropylene Celgard 2400 membrane was used as the separator. The electrolyte was 1M $LiPF_6$ in 1:1:1 ratio of EC:DMC:DEC (EC is ethylene carbonate, DMC is dimethyl carbonate, and DEC is diethyl carbonate) solution (MTI Corp. Richmond, CA). A Keithley 2420 source-meter was used for performing galvanostatic cell discharge/cycling tests. To monitor the phase changes during Li removal, several Li(Mg) electrodes were discharged to certain levels of specific capacity, at a constant current density of 0.5 mA/cm^2. The discharged electrodes were then wrapped in polyethylene protective cover and ex-situ X-ray diffraction was performed to determine the crystallography of phases.

In charge-discharge cycle testing, the cells (Li_8Mg coupled with $LiCoO_2$) were cycled between 4.25 V and 2.8 V at a current density of 0.3 mA/cm^2, which corresponds to a rate of ~C/10 (C defined with respect to $LiCoO_2$). For comparison, a $Li/LiCoO_2$ cell was also cycled under identical conditions. Also, charge/discharge cycling of

---

[z] E-mail: m.jagannathan@utah.edu

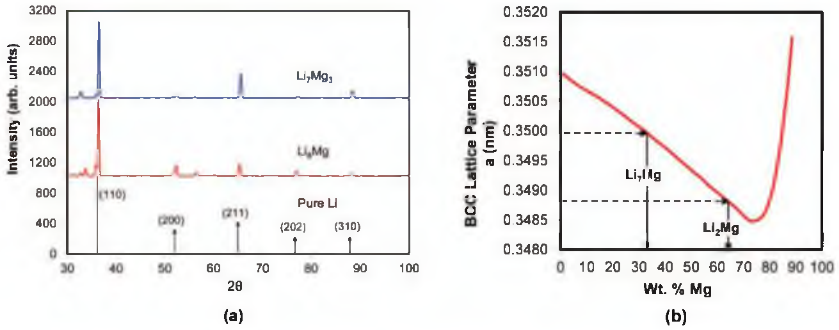

Figure 1. (a) X-ray diffraction patterns of Li$_7$Mg$_3$, Li$_8$Mg, and pure Li and (b) the variation of experimental BCC lattice parameter data of Li(Mg) as a function of Mg content showing the placement of the actual compositions of the two alloys.

Li$_8$Mg electrode was carried out against Li foil to closely examine the mechanism of Li insertion/de-insertion.

Results and Discussion

Electrode composition.— The X-ray diffraction patterns of Li(Mg) alloys along with that of pure Li are shown in Figure 1a. All the diffraction peaks for the Li(Mg) alloys matched with those of Li, but are slightly shifted to the right — the shifts for the strongest peak ($2\theta = 36.2^\circ$) for Li$_7$Mg$_3$ and Li$_8$Mg are 0.18° and 0.06°, respectively. Levinson[16] experimentally showed that the lattice parameter of the BCC unit cell decreases with addition of Mg to Li until the Mg concentration reaches ~75 wt% after which it starts to increase. The alloy lattice parameter (d_{100}) was calculated using the (d_{110}) values, which were determined from the (110) peaks of the alloys. The calculated d_{100} values are compared with Levinson's data[16] in Figure 1b. The alloy compositions thus have been found to correspond to ~64 wt% and ~33 wt% Mg, for Li$_7$Mg$_3$ and Li$_8$Mg respectively. This is roughly in agreement with ICP data from the average of 4 random samples for each of the two alloys (Table I). For X-ray diffraction, the alloy samples were wrapped in polyethylene protective cover inside a glove box and then transported for analysis. Some reaction of Li with air/moisture is unavoidable during handling. This can explain the presence of some additional smaller diffraction peaks in the pattern. The peaks at $2\theta \sim 32.5^\circ$ and at $2\theta \sim 35.7^\circ$ correspond to LiOH (JCPDS card number 32–0564) whereas the peak at $2\theta \sim 33.7^\circ$ can be attributed to LiOH.H$_2$O (JCPDS card number 25–0486).

The average Mg concentrations obtained from the ICP analysis for the two alloys are close to 64 wt% and 28 wt% respectively with a standard deviation of <5 wt%. The small differences in the compositions between the lattice parameter and ICP results may be attributed to some surface oxidation of the alloys during electrode fabrication.

Electrode discharge and phase transition characteristics.— The discharge curves for the Li(Mg) alloy anodes are shown in Figures 2a and 2b. The specific Li discharge capacities (normalized with respect

Table I. Compositions of the two alloys as determined by ICP-AES analysis.

ICP Trial	Mg wt% from ICP for Li-60 wt% Mg	Mg wt% from ICP for Li-30 wt% Mg
1	65.0	27.7
2	64.4	31.1
3	65.3	25.7
4	62.5	27.5

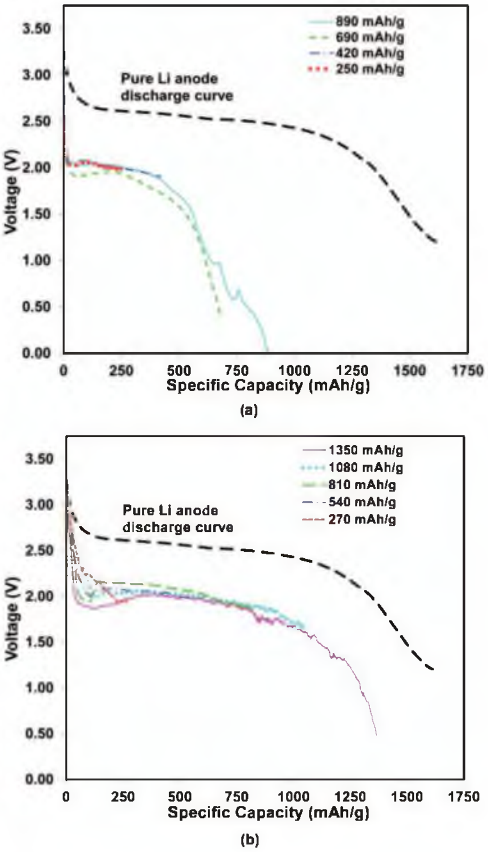

Figure 2. Potential curves for (a) Li$_7$Mg$_3$ and (b) Li$_8$Mg alloy anodes discharged to different capacities (between 250–890 mAh/g for Li$_7$Mg$_3$ and 270–1350 mAh/g for Li$_8$Mg) at a current density of 0.5 mA/cm^2 with MnO$_2$ as the cathode.

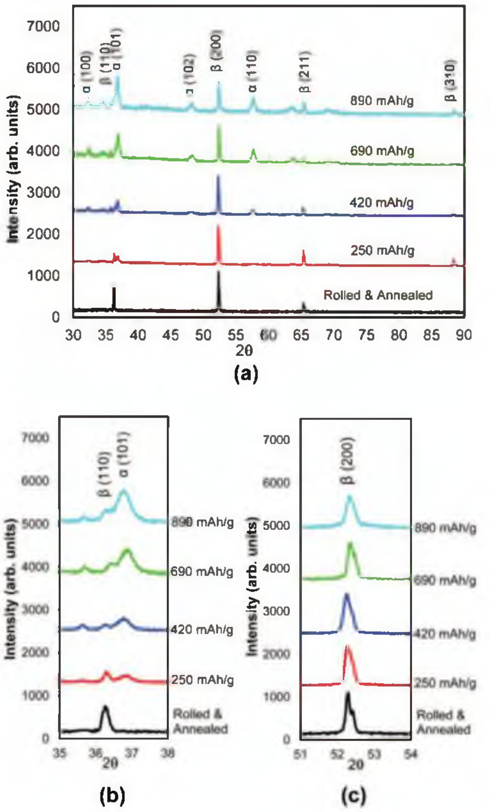

Figure 3. (a) X-ray diffraction data for Li_7Mg_3 alloy anodes with different states of discharge and magnified view of (b) β-phase (110) and α-phase (101) diffraction peaks, and (c) shifting of the (200) β-phase peak position.

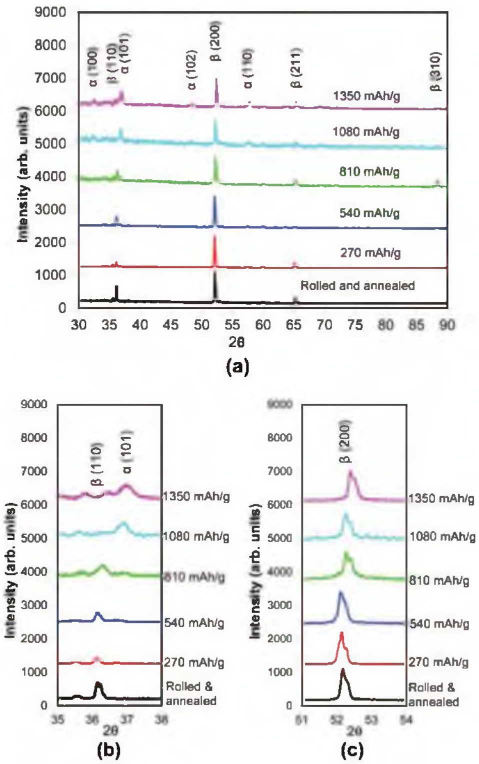

Figure 4. (a) X-ray diffraction data for Li_8Mg alloy anodes with different states of discharge and magnified view of (b) β-phase (110) and α-phase (101) diffraction peaks, and (c) shifting of the (200) β-phase peak position.

to the initial mass of the anode) for Li_7Mg_3 and Li_8Mg are ~900 and ~1350 mAh/g, respectively. All the electrodes for both alloys consistently showed an initial drop in the voltage from open circuit value of 3.25 V to a plateau value of 2 V. This drop may be attributed to the formation of the SEI layer[17] on the surface of the Li(Mg) anode due to reaction with the electrolyte. As the alloy gets depleted in Li, the reduced Li activity on the electrode surface produces the sloping voltage trend, which indicates that the Li removal occurs by a single phase reaction. Considering the fact that the plateau voltages for the two alloys were both around ~ 2 V and that for metallic Li anode is ~2.5 V, the difference of 0.5 V in the plateau potentials can be attributed to the dealloying of Li from Li(Mg), which is in agreement with the observations of Li dealloying at a voltage of 0.2–0.4 V with respect to Li^+/Li.[13,14] A voltage difference of 0.5 V would roughly correspond to a dealloying energy of ~8 kcal/mol of Li[13] assuming rapid charge transfer. This energy is comparable to the estimated free energy of formation of LiAl at room temperature (−8.9 kcal/mol).[18] Thus, the plateau voltage of ~2 V can be explained on the basis of dealloying of Li from Li(Mg).

Ex-situ X-ray diffraction analysis of the electrode samples of both alloys, discharged to different capacities, revealed quite an interesting phase transition behavior (Figures 3a and 4a). A gradual phase transformation from the Li rich BCC β-phase to the Mg rich HCP α-phase can be seen to occur as the delithiation process proceeds with time. Enlarged regions of the XRD patterns around 35–38° (Figures 3b and 4b)) show how the growth of (101) peak of the α-phase proceeds at the expense of the (110) β–phase peak. Enlarged regions around 51–54° show the shifting of (200) β–phase peak to the right (Figures 3c and 4c). These shifts in the peak angles to the right suggest Li depletion from the BCC phase and are in agreement with the reported lattice parameter variations in the BCC Li-Mg phase, shown in Figure 1b.

It is also interesting to note that in the discharge curves (Figures 2a, 2b), the final drop in the voltage from ~1.8 V to values < 0.5 V occurs whenever the height of the (101) α peak becomes comparable to that of the (200) β phase peak (See Figures 3a and 4a). Therefore, it is likely that a significant fraction of α-phase was present on the anode surface and this could be responsible for the final fall in potential after the plateau. The diffusivity of Li in the α-phase region is reported to be $\sim 10^{-9}$ to 10^{-10} cm^2/s[19] which is about 2-3 orders of magnitude less than that in β-phase; hence the formation of the α-phase layer can create a diffusion limitation for delithiation, which in turn would lead to a steep fall in the voltage.

An intriguing observation is that the alloy electrodes did not crumble after complete discharge. Figures 5a and 5b show optical micrographs of the anode samples Li_7Mg_3 and Li_8Mg, after having discharged to capacities of 890 mAh/g and 1350 mAh/g respectively. We can see that the samples are intact and metallic and the Li depletion

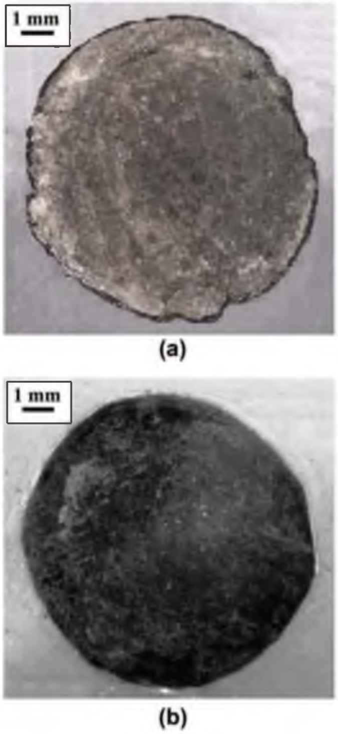

Figure 5. Optical micrographs of (a) Li_7Mg_3 and (b) Li_8Mg electrodes after having been discharged to capacities of 890 and 1350 mAh/g respectively.

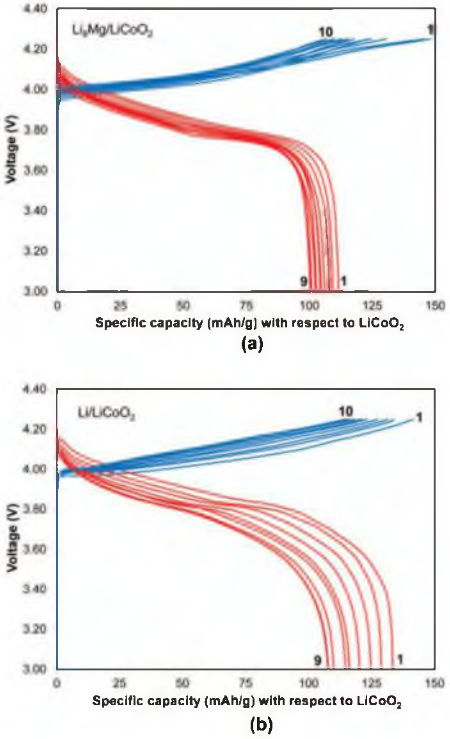

Figure 6. Charge discharge curves of (a) Li_8Mg anode and (b) Li anode with $LiCoO_2$ cathode at a current density of 0.3 mA/cm^2. The first and the tenth charging cycles as well as the first and the ninth discharge cycles are indicated. The capacities are normalized with respect to initial mass of $LiCoO_2$ cathode.

has not led to mechanical degradation. The tarnished appearance on the surface appears to be due to the SEI layer formed by the reaction between the alloys and the electrolyte. The phase transition from Li rich phase to Mg rich phase, as evidenced by XRD and the mechanical integrity of electrode, confirms the fact that Mg is relatively inert during the discharge process. Thus, Mg appears to be providing a good host lattice for Li atoms.

Cell reversibility.— To examine the reversibility performance, Li(Mg) negative electrodes were cycled against $LiCoO_2$ using Swagelok cells. For comparison, these cycling tests were repeated with Li foil anodes. The charge discharge cycling results for the cell combinations: $Li_8Mg/LiCoO_2$ and $Li/LiCoO_2$ are shown in Figures 6a and 6b respectively. A capacity fade with cycling is observed in the Li(Mg) alloy, but this was smaller than that with Li anode. At the end of the 10th charging cycle, the capacity in both the cells is about 100–105 mAh/g (normalized with respect to initial mass of $LiCoO_2$). However, the difference between first cycle charging capacity and first cycle discharge capacity is higher for Li_8Mg, indicating greater irreversible loss. This first cycle capacity loss is usually associated with the formation of the SEI layer on the surface of the electrode. It is possible that the SEI formed on the Li(Mg) consumes more Li or the layer itself has a greater impedance. For the Li anode, this initial capacity loss is smaller, but the discharge capacity decreases more rapidly with each cycle. This suggests that with Li electrode, some Li is being lost after each Li plating cycle, possibly in the form of reaction with electrolyte. On the other hand, for the Li-Mg alloy anode, the discharge curves are more closely spaced, i.e. the decrease in capacity after each cycle is less. This might suggest that the initial SEI layer formed on the Li(Mg) electrode is more stable and prevents continual loss of active material due to reaction with electrolyte during further cycling. It would be interesting to investigate the nature of the SEI layer formed on Li(Mg) electrode. An electrode with a stable SEI layer is highly preferred, as it will ensure good capacity retention over several cycles.

Since the charge/discharge behavior for the $Li/LiCoO_2$ and the $Li_8Mg/LiCoO_2$ cells are nearly similar, it may be inferred that Li insertion into Li_8Mg proceeds through either Li plating or a combination of alloying and plating. In order to further investigate the mechanism of Li insertion/deinsertion in Li(Mg), charge/discharge cycling of Li_8Mg electrode was carried out against Li foil between 0–0.7 V at a current density of 0.3 mA/cm^2 (See Figure 7). It can be seen that after initial delithiation (capacity of ~360 mAh/g). Li can be successfully inserted into the Li(Mg) electrode— however, the lithiation capacity decreases from 37 mAh/g in the first cycle to 14 mAh/g in the fourth cycle, as shown in the figure. This indicates that Li(Mg) alloy electrodes could show reversible Li storage if the electrode structure can be optimized.

The result shown in Figure 7 is indicative of electrochemical alloying between Li and Li(Mg) during lithiation. The alloying potential for Li on pure Mg has been reported be in the range of 0.015–0.05 V.[14,15] The cell potential during lithiation is positive and close to the reported

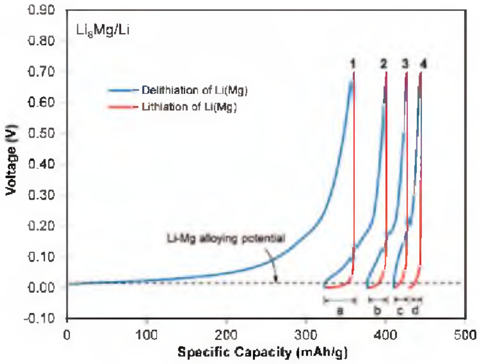

Figure 7. Lithiation/delithiation characteristics of a Li_8Mg/Li cell cycled between 0–0.7 V at a current density of 0.3 mA/cm^2. The ranges indicated in a, b, c and d are the lithiation capacities for the first four cycles (37, 24, 17 and 14 mAh/g respectively).

values, thus providing evidence for alloy formation. The asymmetry between the charge and discharge behavior of Li(Mg) electrodes is interesting and requires further investigation. The chemical composition of the electrode surface could be responsible for inhibiting the alloying reaction. The alloying kinetics might be improved if porous or nanostructured Li(Mg) electrodes are employed where Li pile-up can be potentially reduced or avoided.

Conclusions

(1) Li(Mg) alloy electrodes of two nominal compositions, Li_7Mg_3 and Li_8Mg, were successfully made in the laboratory.
(2) The Li(Mg) alloy electrodes showed a delithiation behavior during cell discharge which is comparable to that of pure Li electrode. An intriguing observation is that the plateau potential is 2 V compared to 2.5 V for Li (against MnO_2) which closely corresponded to the dealloying potential of Li from Li(Mg).
(3) A continuous and gradual phase transition from Li-rich BCC β-phase to Li-lean α-phase occurred evidencing a diffusion-controlled Li transport process during the delithiation of the electrodes. The accompanying shifts in X-ray diffraction peaks were consistent with the notion of RT Li diffusion causing the phase transition during delithiation.
(4) The Mg-rich electrodes after discharge were structurally intact, suggesting Mg can act as a host for Li insertion and removal.
(5) The cyclic reversibility of the Li(Mg)-$LiCoO_2$ cell was limited as indicated by the charging potential saturating to about 4 V over all the cycles. There was some experimental indication of limited alloying of Li in Li(Mg) during charging. This is in contrast with the smooth delithiation process where RT Li diffusion kinetics appears to be controlling the process. Further investigation would be interesting.

Acknowledgments

This research was supported by NSF through grant DMR-1135176 and the associated undergraduate research supplement. The authors thank Dr. G. V. Subba Rao, formerly at National University of Singapore, for many insightful suggestions.

References

1. C. J. Wen and R. A. Huggins, *J. Electrochem. Soc.*, **128**, 1181 (1981).
2. I. A. Courtney, J. S. Tse, O. Mao, J. Hafner, and J. R. Dahn, *Phys. Rev. B*, **58**, 15583 (1998).
3. R. A. Huggins, in *Handbook of Battery Materials* J. O. Besenhard Editor, p. 359, Wiley-VCH, Weinheim (1999).
4. J. Wang, I. D. Raistrick, and R. A. Huggins, *J. Electrochem. Soc.*, **133**, 457 (1986).
5. M. Winter and J. r. O. Besenhard, *Electrochim. Acta*, **45**, 31 (1999).
6. J. Yang, M. Wachtler, W. Martin, and O. B. Jurgen, *Electrochem. Solid-State Lett.*, **2**, 161 (1999).
7. H. Kim, M. Seo, M. H. Park, and J. Cho, *Angew. Chem. Int. Ed.*, **49**, 2146 (2010).
8. A. A. Nayeb-Hashemi, J. B. Clark, and A. D. Pelton, *Journal of Phase Equilibria*, **5**, 365 (1984).
9. R. Nesper, *Prog. Solid State Chem.*, **20**, 1 (1990).
10. R. Nesper, *Angew. Chem. Intl. Ed. Engl.*, **30**, 789 (1991).
11. R. S. Busk, *Trans. Metall. Soc. AIME*, **188**, 1460 (1950).
12. A. N. Dey, *J. Electrochem. Soc.*, **118**, 1547 (1971).
13. M. M. Nicholson, *J. Electrochem. Soc.*, **121**, 734 (1974).
14. Z. Shi, M. Liu, D. Naik, and J. L. Gole, *J. Power Sources*, **92**, 70 (2001).
15. H. Kim, B. Park, H.-J. Sohn, and T. Kang, *J. Power Sources*, **90**, 59 (2000).
16. D. W. Levinson, *Acta Metall.*, **3**, 294 (1955).
17. E. Peled, *J. Power Sources*, **9**, 253 (1983).
18. N. P. Yao, L. A. Heredy, and R. C. Saunders, *J. Electrochem. Soc.*, **118**, 1039 (1971).
19. Y. Iwadate, M. Lassouani, F. Lantelme, and M. Chemla, *J. Appl. Electrochem.*, **17**, 385 (1987).

CHAPTER 4

ENERGY STORAGE CAPACITY AND ELECTROCHEMICAL CYCLABILITY OF COLUMNAR SI STRUCTURES AS ANODES FOR LI-ION BATTERIES

(Manuscript in preparation)

4.1 Introduction

Si is a highly desirable anode material for Li ion batteries because it offers a very large specific capacity (3580 mAh/g) that is about an order of magnitude higher than the capacity of graphite or C-based anodes[1]. However, the large volume expansion in Si during lithiation (~300% corresponding to the formation of $Li_{22}Si_5$) causes cracking and pulverization of the electrode. This leads to a progressive loss of contacts between active material regions as well as with the current collector, resulting in capacity fading during electrochemical charge/discharge cycling of Si [1-3]. To mitigate this problem, researchers have focused on designing anodes made of (a) amorphous/crystalline Si thin films [4, 5], (b) micro/nanosized Si powders [3, 6-8], (c) Si-based composites [9-12], and several modifications of these materials. Architectured Si anodes consisting of Si nanowires[13-15], Si core-shell nanowires[16, 17] and porous Si structures[18, 19] are also attracting a lot of attention, particularly as a way of dealing with the volume change problem of Si during lithiation.

Porous Si anodes obtained by electrochemical etching are promising because of the relative ease of fabrication and the control available to engineer the pore morphology. Also, electrochemical etching of Si lends itself readily to process scale-up, which is necessary for successful commercialization. Shin *et al.*[20] first explored the feasibility of using one-dimensional porous Si as a negative electrode for rechargeable batteries. Thakur's group[21, 22] has investigated the lithiation/delithiation characteristics of gold coated porous Si films and macroporous Si particulates. Zhu *et al.*[23] synthesized nanoporous Si networks and reported a reversible capacity of 1000 mAh/g after 200 cycles.

While the promise of porous Si is clear, it is not known how the changes in pore dimensions and other morphological changes, which are sometimes difficult to control, will affect the lithiation capacity and cell cyclability. There is no research in the literature which has systematically examined the effect of pore dimensions and morphology on cycling characteristics. Additionally, much of the work is inclined towards reporting energy capacities with little exploration into the mechanisms of lithiation of Si columnar spacing.

The objective of this work is to first synthesize porous Si anodes with different columnar morphologies (different pore size and volume fraction) and then to examine the effect of the structural characteristics on the lithiation/delithiation behavior. The findings from this work can offer insights as to how to design the optimum structure for obtaining the best electrochemical performance from porous Si anodes in the context of Li-ion batteries.

4.2 Experimental Procedure

4.2.1 Synthesis of Porous Si

Single-side polished p-type (B-doped) Si wafers, (with (100) orientation, a resistivity of 1-10 ohm-cm and thickness of 375 μm), manufactured by Silicon Quest International, were used in the etching experiments. The wafer was placed in the cavity of a Teflon beaker cell with a Pt coil acting as the counter electrode. To create an ohmic contact for Si, a 275 nm thick Cu layer was deposited on the back surface of the wafer by e-beam evaporation. The wafer was then annealed at 700°C for 2 hours to diffuse Cu into Si and to form a strong and conducting back layer.

The electrolyte solution is 49% HF mixed with dimethylformamide (DMF) in different proportions. It has been reported[24] that the presence of a mild oxidizer such as

DMF in the etch solution creates smooth and narrow pores. Also, DMF is a good solvent for positive charge carriers[25] — a higher concentration of DMF increases the flux of holes at the pore walls, thereby increasing the pore diameter.

Different pore structures were obtained by varying the following parameters: (1) current density, (2) etching duration, and (3) the HF:DMF ratio. To examine the effect of surface roughness of Si wafer on columnar morphology, etching experiments were carried out on the polished surface of the Si wafer as well as the rougher caustic-etched back side. The etching current was controlled with the help of a Keithley 2400 source-meter and the voltage was monitored during the experiments. The top views and the cross-sections of the etched structures were examined under SEM. The SEM micrographs were used to estimate the void fraction in the porous structures.

4.2.2 Lithiation/Delithiation Cycling of Porous Si

The electrodes for the lithiation/delithiation cycling experiments were obtained by cutting out disks of area 5 mm^2 from the etched region of the Si wafer. The Cu layer deposited on the rear surface of the Si wafers functioned like a current collector during the electrochemical charge discharge tests. A two-electrode Swagelok cell was used for the cycling experiments, with Li as the counter electrode and 1M LiPF6 in EC: DEC: DMC as the electrolyte. A Celgard 2400 polypropylene separator, soaked with electrolyte was placed between the porous Si and the Li foil. A current corresponding to a C-rate of C/10 was used in these experiments. The specific capacity, C, here is calculated on the basis of the porous Si mass, using the following formula:

C = (3580 mAh/g) x (2.33 g/cc) x (1-porosity) x (electrode area) x (average etched depth) where 3580 mAh/g is the specific lithiation capacity of Si at room temperature and 2.33 g/cc is the density of Si. After 20 charge/discharge cycles, the cycled electrode was rinsed in DMC to remove traces of electrolyte and then was examined under SEM.

4.3 Results and Discussion

4.3.1 Porous Si Structure

Table 4.1 shows the etching parameters used in fabricating four different porous structures. The four porous Si structures will be henceforth referred to as PS1, PS2, PS3 and PS4. Table 4.2 lists the estimated pore diameter, pore fraction, and the etched depth for each structure. The top views and the cross-sectional views of the porous structures of the samples PS1 to PS4 are shown in Figures 4.1(a)-4.1(d) and Figures 4.2(a)-4.2(d), respectively.

It can be seen that the average pore diameters of PS1 and PS4 are nearly similar (about 1 μm each). The average pore diameter of PS2 is slightly larger (1.3 μm) and that of PS3 is the largest (~ 2μm). While the PS1 and PS4 have similar pore areal fractions (about 0.5), the PS2 has an intermediate value (0.63) and PS3 has the highest porosity (0.75). It appears that in PS3, the relatively higher current density might have caused a rapid transverse etching of Si walls, leading to pore collapse and resulting in a network of columns with significant connected porosity (see Figure 4.1(c)).

An interesting observation is that even though the pore structures in PS1 and PS4 are similar to each other, for PS4 (where it was the unpolished surface that was etched), the porous regions are separated from each other by a network of boundaries (Figure 4.1(d)). On the other hand, there are no such boundaries visible in PS1. It is possible that the relatively rougher unpolished surface of the Si wafers, which has more defects than

Table 4.1 Etching parameters for the Si porous and columnar structures

Sample name	**HF:DMF ratio**	**Current density (mA/cm^2)**	**Etching duration**	**Surface etched**
PS1	1:30	0.9	4 hrs	Polished
PS2	1:10	0.9	3 hrs	Polished
PS3	1:10	1.3	4 hrs	Polished
PS4	1:30	1.1	4 hrs	Nonpolished

Table 4.2 Pore morphologies of the Si porous and columnar structures

Sample name	**Average pore diameter (μm)**	**Average etched depth (μm)**	**Pore fraction**
PS1	1.0	8	0.52
PS2	1.3	7	0.63
PS3	2.0	9	0.75
PS4	1.0	8	0.49

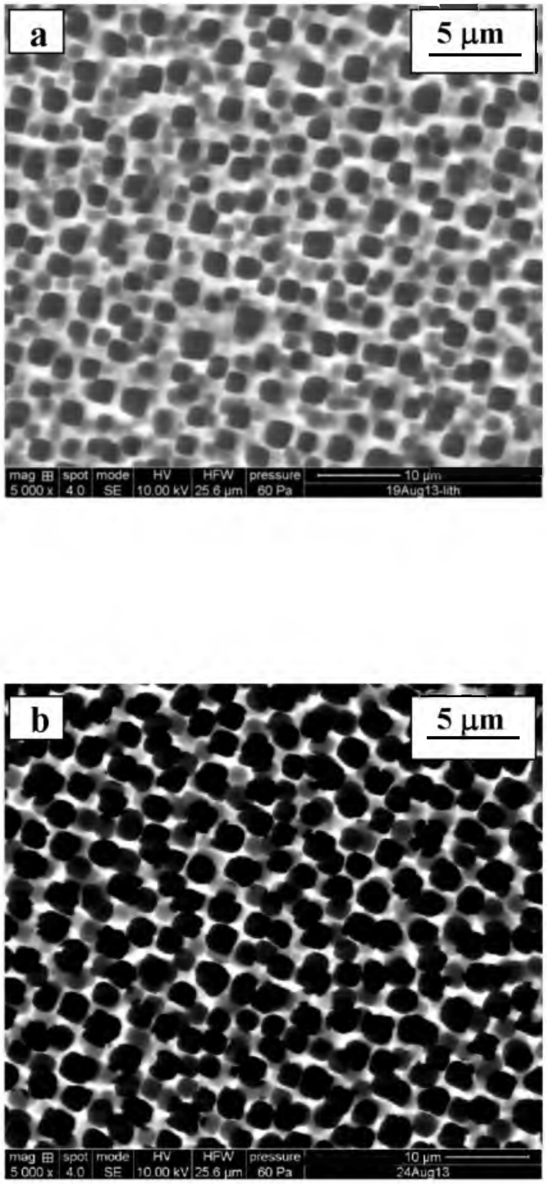

Figure 4.1 SEM micrographs showing the top views of the porous Si columnar structures: (a) PS1, (b) PS2, (c) PS3, and (d) PS4.

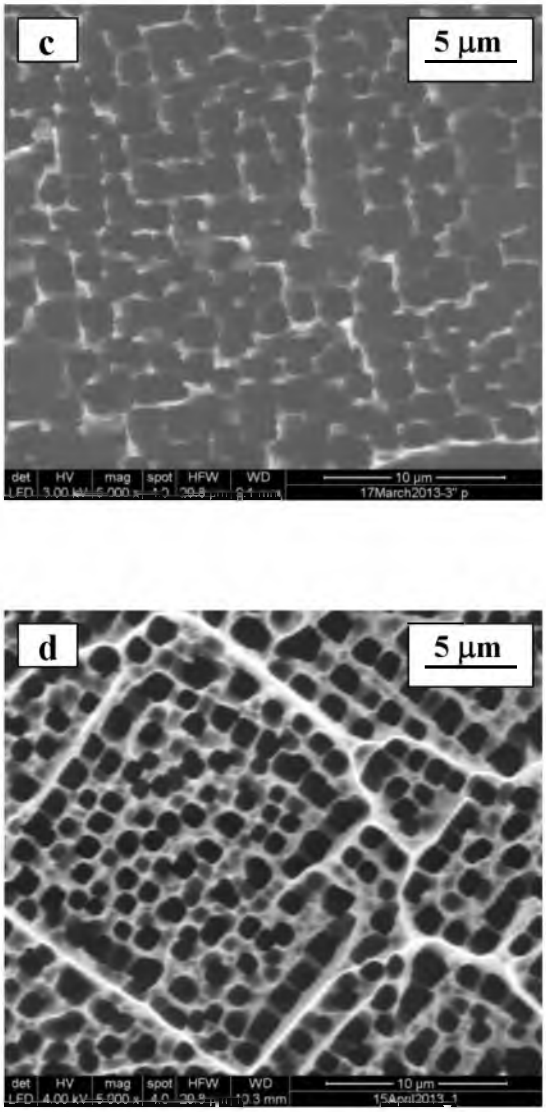

Figure 4.1 continued

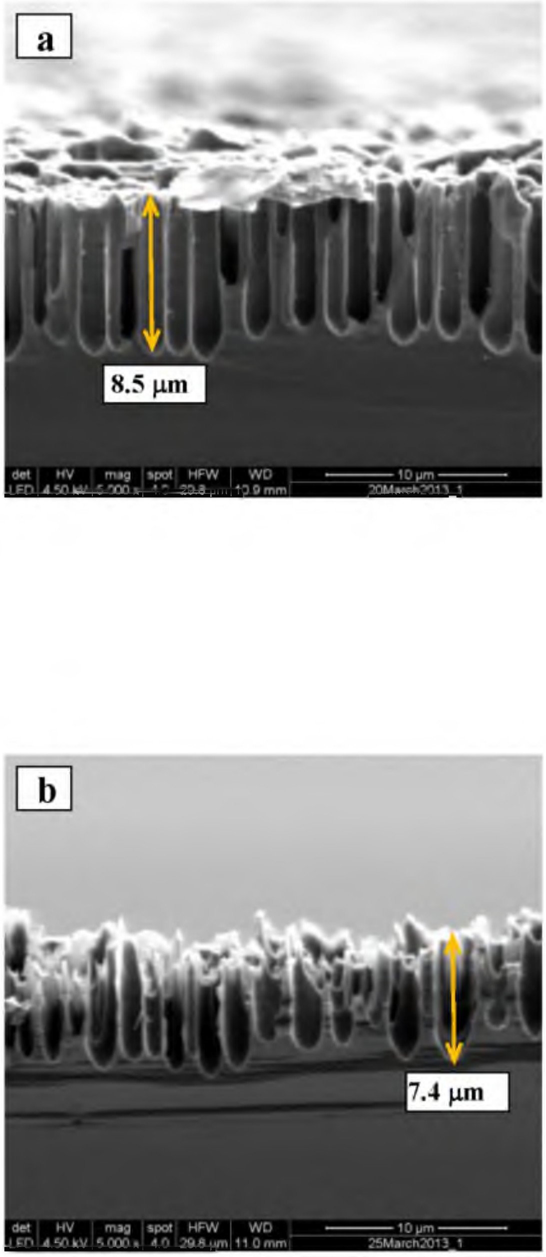

Figure 4.2 SEM micrographs showing the cross-sectional views of the porous Si columnar structures: (a) PS1, (b) PS2, (c) PS3, and (d) PS4.

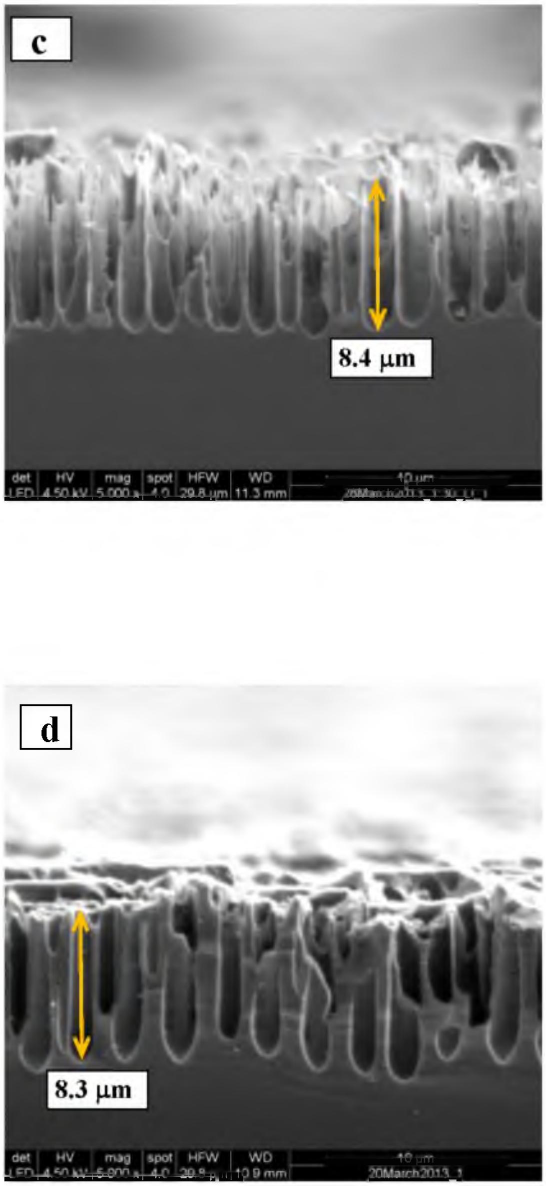

Figure 4.2 continued

the polished side, is responsible for the presence of these boundaries. An investigation into this, however, is beyond the scope of this work.

The SEM micrographs of transverse sections of Si columnar structures are shown in Figures 4.2(a) through 4.2(b). It can be seen that the average etch depths of all the structures are nearly similar, between 7-9 μm. The columnar pore walls are thicker in PS4 and PS1, whereas they are thinner and possibly more fragile in PS2 and PS3.

4.3.2 Electrochemical Lithiation/Delithiation Cycling of Porous Si

The electrochemical charge/discharge results of the porous Si columnar structures, with Li foil serving as the counter electrode, are shown in Figures 4.3(a)-4.3(d). For all the structures, during the first lithiation step, the cell potential reached a plateau at a voltage between 0 to 0.1V. This plateau can be attributed to the amorphization of crystalline Si [26] in the porous regions upon alloying with Li The first cycle lithiation was stopped at the end of 10 hours, (because a C-rate of C/10 was used) and then the cell was cycled between the potential limits of 0.1-1V.

The capacity corresponding to the first cycle delithiation of Si is always less than the first cycle lithiation capacity (3580 mAh/g), as can be seen in Figures 4.3(a-d). This irreversible capacity loss is of the order of 300-1000 mAh/g and is seen in other works as well. This is usually attributed to loss of active material due to reaction with electrolyte[27], which presumably involves the formation of the solid electrolyte interface (SEI) layer on Si.

The lithiation voltage curves, from the second cycle onwards, are quite different from the one observed in the first cycle—the sloping plateau is shifted to a higher voltage, close to 0.2 V. This plateau is followed by a slow decrease to about 0.1V.

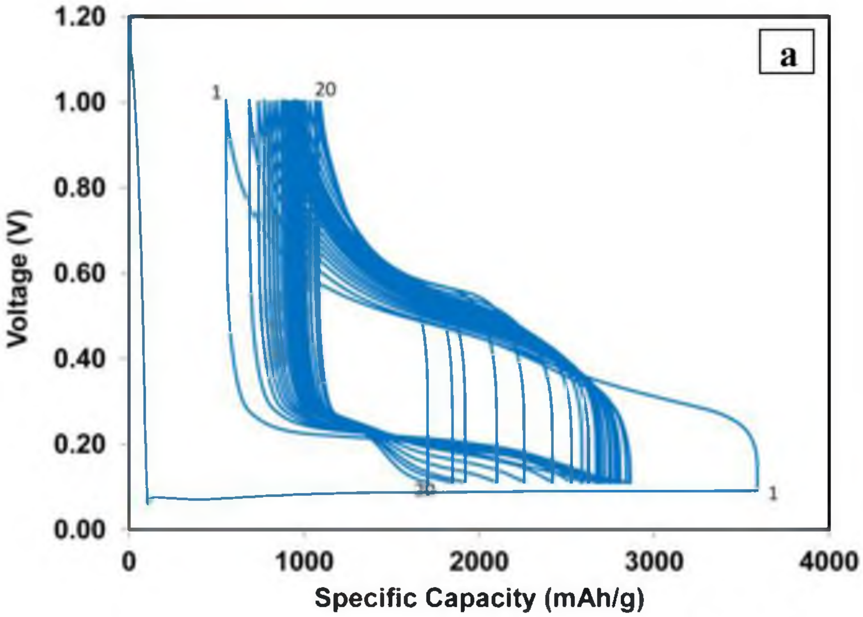

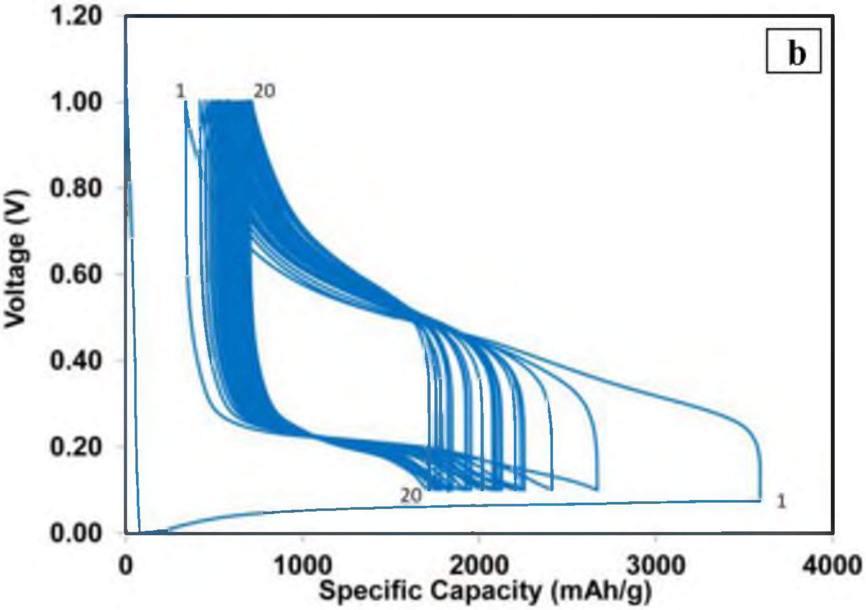

Figure 4.3 Cell potential curves obtained from electrochemical charge/discharge cycling of (a) PS1, (b) PS2, (c) PS3, and (d) PS4 porous Si electrodes with Li as the counter electrode at a constant current of C/10. The 1st and 20th charge/discharge cycles are marked.

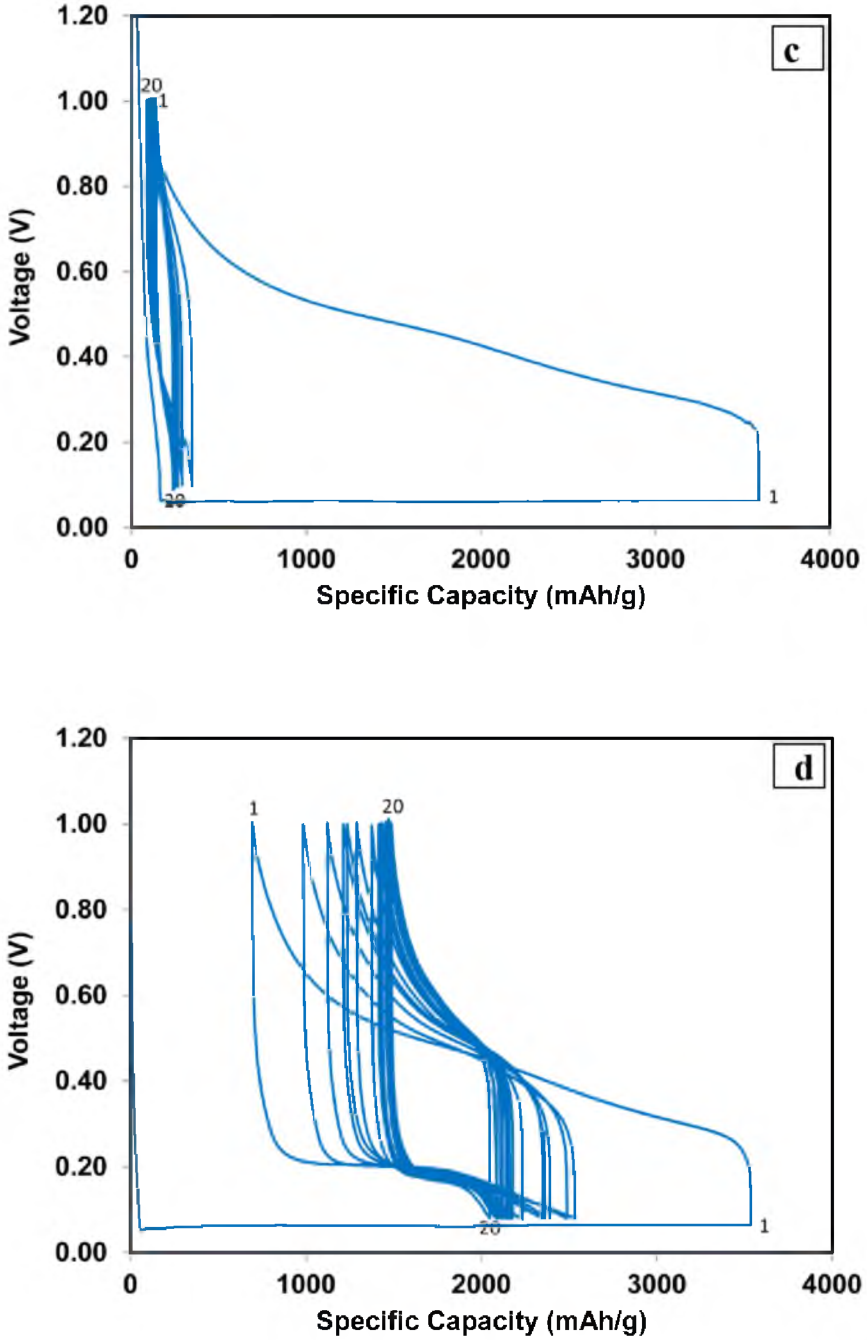

Figure 4.3 continued

The voltage during delithiation increases continuously from 0.1V till it reaches a potential of 1V—this trend is characteristic of a single phase reaction and can be attributed to delithiation occurring from a solid solution layer of amorphous Li_xSi[28].

The variations in lithiation and delithiation capacities with cycle number for the four porous Si columnar structures are shown in Figure 4.4. Both the lithiation/delithiation capacities for PS3 fall rapidly to <150 mAh/g within the first 5 cycles but during further cycling, the decrease is much less— by the end of 20th cycle, we still have a reversible capacity of ~100mAh/g. This perhaps suggests that the columnar network with large open porosity in PS3 is unable to efficiently accommodate the volume changes upon Li insertion and removal from the Si columns during cell cycling.

It is very interesting the structures PS1 and PS2 showed stable and reversible lithiation/delithiation capacities, in excess of 1000 mAh/g for 20 cycles. The capacities

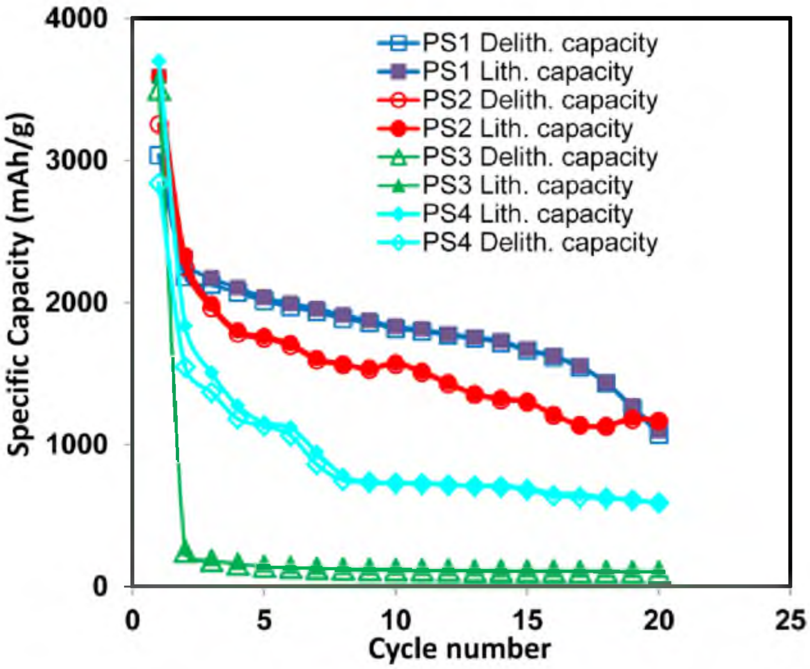

Figure 4.4 Variation of lithiation and delithiation capacities as a function of the cycle number for the four porous Si electrodes

for PS1 are larger than those for PS2 by 200-400 mAh/g during cycles 3 to 15. However, after 15 cycles, the PS1 capacities fall rapidly and by the end of the 20th cycle, both the structures show similar charge/discharge capacities, but are still larger than 1000 mAh/g, which is remarkable. In comparison, Thakur *et al.*[21] reported a reversible capacity of only 76 mAh/g after 10 cycles for macroporous columnar Si electrodes without any added coating on the Si columnar structures. The performance of the PS4 electrode was intermediate between PS2 and PS3, with the capacities dropping to <800 mAh/g after 8 cycles and then decreasing to 600 mAh/g by the end of 20th cycle.

The SEM micrographs of the cycled electrodes, shown in Figures 4.5(a) through 4.5(d), offer further insights into the nature of capacity trends observed in Figure 4.4. Also, Figures 4.6 (a) and 4.6(b) show the cross-sectional views of the cycled PS3 and PS4 electrodes, respectively. In general, the two major possible reasons behind a decrease in capacities are (a) consumption of active material due to reaction with electrolyte and (b) structural degradation in the electrode. It has been reported[27] that unlike many other anode materials, Si does not form a stable passivation layer with electrolyte, meaning there will be some capacity loss after each cycle due to reaction with electrolyte. This capacity loss will be more prominent in the initial cycles.

It appears from Figures 4.5(a) through 4.5(d) that the Si columns are reacting with the electrolyte to form a film. This reaction layer can be clearly seen in Figure 4.5 (a). The higher impedance of this thicker reaction layer could be limiting the extent of Li insertion and removal in the final few cycles for this structure. In the case of PS4, the long boundary walls present in the original etched structure are preserved (Figure 4.5(d)).

It is interesting to note that the columnar structure is preserved, to a large extent,

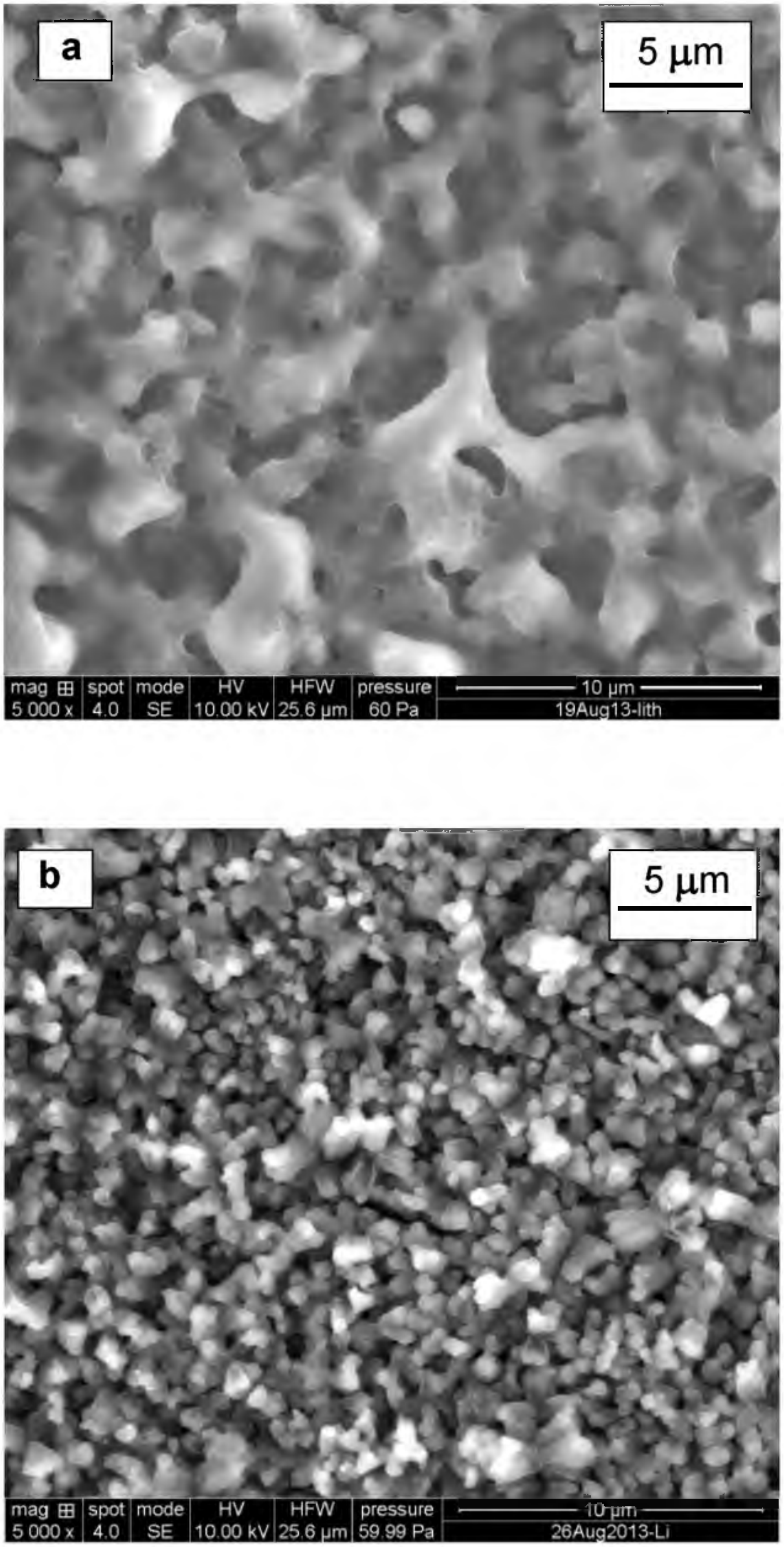

Figure 4.5 SEM micrographs showing the top views of the cycled porous Si electrodes for the samples: (a) PS1, (b) PS2, (c) PS3, and (d) PS4.

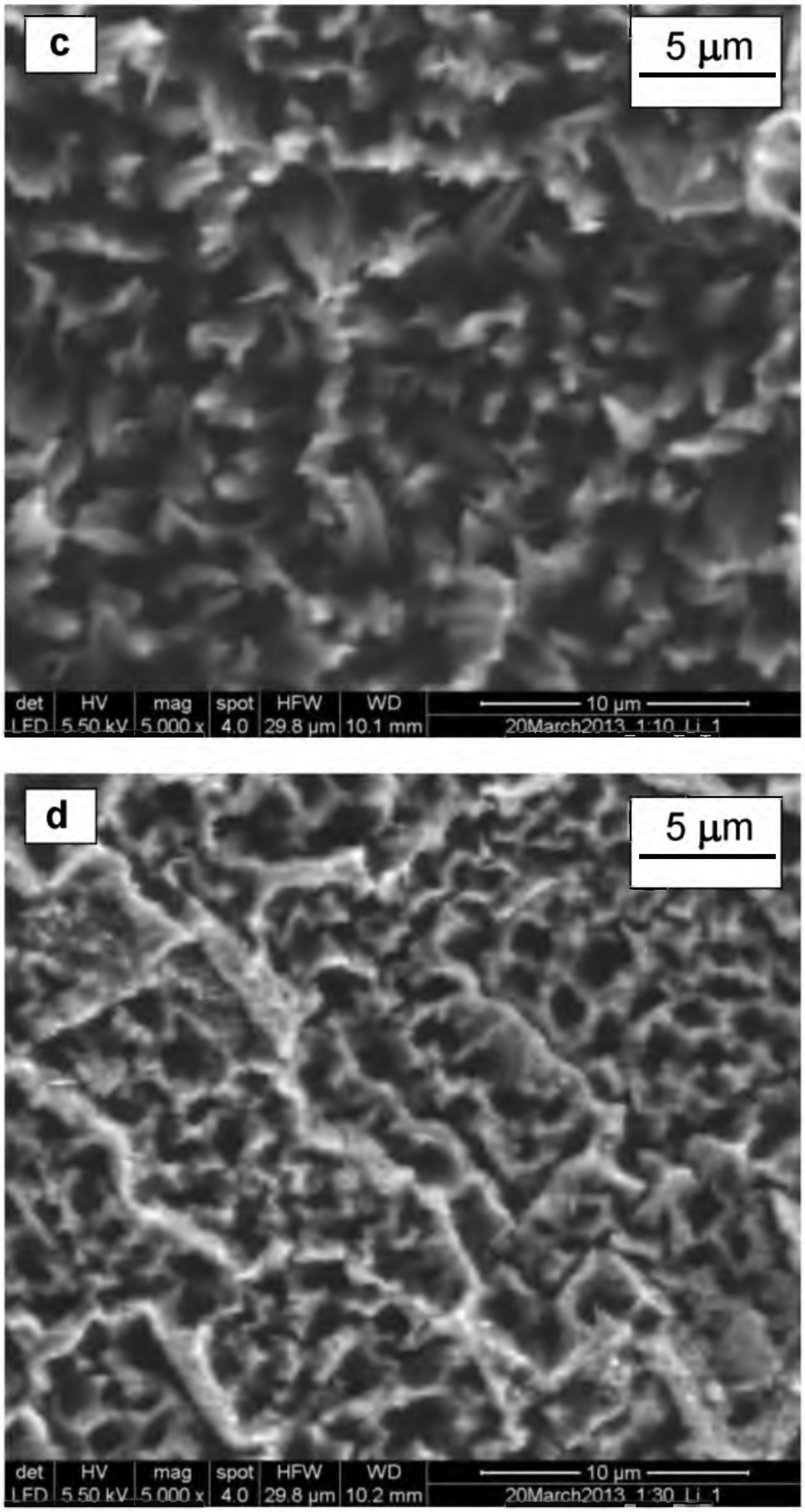

Figure 4.5 continued

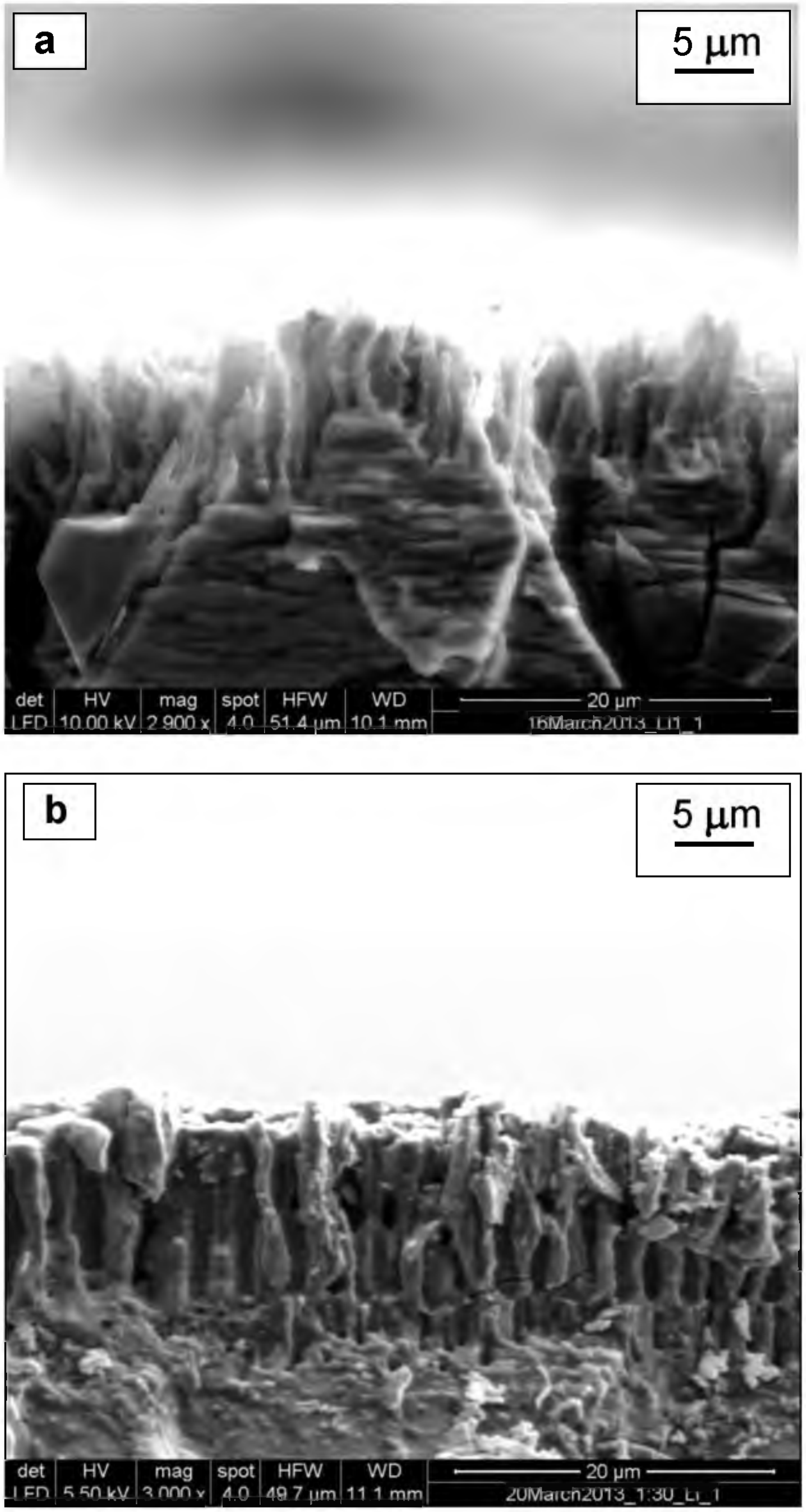

Figure 4.6 SEM micrographs showing the cross-sectional views of the cycled porous Si electrodes for the samples: (a) PS3, and (b) PS4.

in the cycled PS3 and PS4 electrodes (Figures 4.6(a) and 4.6(b)) (even though the electrochemical performance of PS3 was poor). The columns appear distorted in both the cycled electrodes, presumably due to the volume expansions during the lithiation cycles.

4.4 Conclusions

1. Four different pore morphologies were successfully synthesized on p-type [100] oriented Si wafers by electrochemical etching using an electrolyte made of HF and DMF.
2. The electrochemical performance of two electrodes (PS1, PS2) with porosities between 50-65% and with a clear columnar structure were the best —the reversible capacities at the end of 20th cycle for these electrodes were in excess of 1000 mAh/g, which is significantly higher than most values reported in literature for Si electrodes with columnar structures.
3. The Si electrode with the largest open porosity (75%) was not able to provide significant cyclic lithiation and delithiation capacities (<150 mAh/g) during cycling tests. This appears to be due to the gross destruction of the columnar/porous structure.
4. An important finding is that the columnar structure seems to be preserved in the electrodes after charge/discharge cycling, even in the case of the Si electrode with the poor electrochemical performance.

4.5 References

1. T. D. Hatchard and J. R. Dahn, *Journal of The Electrochemical Society*, **151**, A838 (2004).
2. J. O. Besenhard, J. Yang and M. Winter, *Journal of Power Sources*, **68**, 87

(1997).

3. J. H. Ryu, J. W. Kim, Y.-E. Sung and S. M. Oh, *Electrochemical and Solid-State Letters*, 7, A306 (2004).

4. K. L. Lee, J. Y. Jung, S. W. Lee, H. S. Moon and J.-W. Park, *Journal of Power Sources*, **129**, 270 (2004).

5. J. P. Maranchi, A. F. Hepp and P. N. Kumta, *Electrochemical and Solid-State Letters*, **6**, A198 (2003).

6. Z. P. Guo, J. Z. Wang, H. K. Liu and S. X. Dou, *Journal of Power Sources*, **146**, 448 (2005).

7. H. Li, X. Huang, L. Chen, Z. Wu and Y. Liang, *Electrochemical and Solid-State Letters*, **2**, 547 (1999).

8. B. Gao, S. Sinha, L. Fleming and O. Zhou, *Advanced Materials*, **13**, 816 (2001).

9. I. S. Kim, G. E. Blomgren and P. N. Kumta, *Electrochemical and Solid-State Letters*, **6**, A157 (2003).

10. Z. P. Guo, Z. W. Zhao, H. K. Liu and S. X. Dou, *Journal of Power Sources*, **146**, 190 (2005).

11. Q. Si, K. Hanai, N. Imanishi, M. Kubo, A. Hirano, Y. Takeda and O. Yamamoto, *Journal of Power Sources*, **189**, 761 (2009).

12. G. X. Wang, J. H. Ahn, J. Yao, S. Bewlay and H. K. Liu, *Electrochemistry Communications*, **6**, 689 (2004).

13. C. K. Chan, H. Peng, G. Liu, K. McIlwrath, X. F. Zhang, R. A. Huggins and Y. Cui, *Nature Nanotechnology*, **3**, 31 (2007).

14. K. Peng, J. Jie, W. Zhang and S. T. Lee, *Applied Physics Letters*, **93**, 033105 (2008).

15. C. K. Chan, R. N. Patel, M. J. O'Connell, B. A. Korgel and Y. Cui, *ACS Nano*, **4**, 1443 (2010).

16. L. F. Cui, R. Ruffo, C. K. Chan, H. Peng and Y. Cui, *Nano Letters*, **9**, 491 (2008).

17. L. F. Cui, Y. Yang, C. M. Hsu and Y. Cui, *Nano Letters*, **9**, 3370 (2009).

18. J. Cho, *Journal of Materials Chemistry*, **20**, 4009 (2010).

19. Y. Zheng, J. Yang, J. Wang and Y. NuLi, *Electrochimica Acta*, **52**, 5863 (2007).

20. H. C. Shin, J. A. Corno, J. L. Gole and M. Liu, *Journal of Power Sources*, **139**, 314 (2005).

21. M. Thakur, M. Isaacson, S. L. Sinsabaugh, M. S. Wong and S. L. Biswal, *Journal of Power Sources*, **205**, 426 (2012).

22. M. Thakur, S. L. Sinsabaugh, M. J. Isaacson, M. S. Wong and S. L. Biswal, *Scientific Reports*, **2** (2012).

23. J. Zhu, C. Gladden, N. Liu, Y. Cui and X. Zhang, *Phys. Chem. Chem. Phys.*, **15**, 440 (2012).

24. H. Ouyang, M. Archer and P. M. Fauchet, in *Frontiers in Surface Nanophotonics*, p. 49, Springer, New York (2007).

25. P. Bettotti, Z. Gaburro, L. D. Negro and L. Pavesi, *Materials Research Society Symposium Proceedings*, **722**, 449 (2002).

26. P. Limthongkul, Y. I. Jang, N. J. Dudney and Y. M. Chiang, *Acta Materialia*, **51**, 1103 (2003).

27. Y. M. Lee, J. Y. Lee, H.-T. Shim, J. K. Lee and J.-K. Park, *Journal of The Electrochemical Society*, **154**, A515 (2007).

28. H. S. Kim, K. Y. Chung and B. W. Cho, *Bull. Korean Chem. Soc*, **29**, 1965 (2008).

CHAPTER 5

ANALYTICAL MODELING AND SIMULATION OF ELECTROCHEMICAL CHARGE/DISCHARGE BEHAVIOR OF SI THIN FILM NEGATIVE ELECTRODES IN LI-ION CELLS

Published as:

M. Jagannathan and K.S. Ravi Chandran, “Analytical Modeling and Simulation of Electrochemical Charge/Discharge Behavior of Si Thin Film Negative Electrodes in Li-ion Cells”, *Journal of Power Sources*, 2014, Vol. 247, p. 667-675.

Journal of Power Sources 247 (2014) 667–675

Contents lists available at ScienceDirect

Journal of Power Sources

journal homepage: www.elsevier.com/locate/jpowsour

Analytical modeling and simulation of electrochemical charge/discharge behavior of Si thin film negative electrodes in Li-ion cells

M. Jagannathan, K.S. Ravi Chandran*

Department of Metallurgical Engineering, University of Utah, 135 South, 1460 East, Room 412, Salt Lake City, UT 84112, USA

HIGHLIGHTS

- We developed a model to simulate charge/discharge behavior of a-Si film electrodes.
- Analytical solutions were derived to describe Li concentration profiles within a-Si.
- Simulations agreed well with experimental charge/discharge data of a-Si films.
- Electrode-diffusion-limitation is prominent in thicker electrodes & at high C-rates.
- Low standard rate constant value for charge transfer limits capacity at all C-rates.

ARTICLE INFO

Article history:
Received 24 July 2013
Accepted 25 August 2013
Available online 3 September 2013

Keywords:
Analytical model
Amorphous Si
Thin films
Diffusion

ABSTRACT

Physically-based analytical models that provide insights into the diffusion and/or interface charge transfer effects in bulk (lithiating/delithiating) electrodes are needed to truly assess the performance/limitations of electrode materials for Li-ion batteries. In this context, an analytical modeling framework is constructed here to predict the electrochemical charge–discharge characteristics during lithiation and delithiation of solid amorphous Si (a-Si) thin film electrodes. The framework includes analytical expressions that satisfy Fick's second law for Li transport and the requisite flux boundary conditions of lithiation and delithiation steps. The expressions are derived here by the method of separation of variables. They enable the determination of transient Li concentration profiles in the thin film electrode as a function of state of charge/discharge. The time-dependent electrode surface concentrations (at the electrode–electrolyte interface) obtained from these profiles were used to determine the activation overpotentials and thus, the non-equilibrium cell potentials, as a function of state of charge/discharge using Butler–Volmer kinetics. The simulated charge/discharge characteristics agreed well with the experimental data of a-Si thin film electrodes obtained at different C-rates. The model offers insights into how the charge-discharge behavior is controlled by diffusion limitation within electrode and/or the activation overpotentials at the interface. The analytical framework is also shown to predict successfully the hysteretic behavior of lithiation/delithiation voltage curves.

1. Introduction

Lithiation/delithiation characteristics of a-Si solid electrodes in an electrochemical cell are ideally suited, for a number of reasons, for the development of physically-based models that provide a robust description of the electrochemical cell or battery behavior and performance. Firstly, other than Li, Si is the anode material that offers the highest energy density (~3590 mAh g^{-1}) [1]. Secondly, amorphous Si (a-Si) thin film electrodes, in particular, show better cycling characteristics than crystalline Si (c-Si) electrodes [2,3], primarily due to the continuous and single-phase reaction (Li_xSi with $x < 3.75$) without phase transformation and with more homogeneous volume expansions. A further advantage is the relatively fast Li transport in the amorphous phase — the diffusion coefficient of Li in a-Si is $\sim 10^{-13}$ cm^2 s^{-1}, which is higher than that in c-Si ($\sim 10^{-14}$ cm^2 s^{-1}) [4,5]. More importantly, a-Si films remain fully amorphous during lithiation/delithiation cycling, especially if

---

* Corresponding author. Tel.: +1 (801) 581 7197; fax: +1 (801) 581 4937.
E-mail address: ravi.chandran@utah.edu (K.S.R. Chandran).

0378-7753/$ – see front matter © 2013 Elsevier B.V. All rights reserved.
http://dx.doi.org/10.1016/j.jpowsour.2013.08.092

the film thickness is less than 1–2 μm [6], avoiding problems associated with crystalline-amorphous phase transitions. The modeling is also practically relevant because Si thin-film based Li-ion batteries are attracting a lot of attention as effective energy storage devices in microelectromechanical systems (MEMS), implantable medical devices, and in other such applications [5].

While it is clear that practically useful insights into the mass transfer and charge transfer aspects during cell cycling can be obtained by modeling, there is no specific modeling work in literature focusing on the charge/discharge processes in solid, or specifically, a-Si thin film electrode. There are several modeling works examining various aspects of cell/battery behavior of porous electrodes, which do not apply to the solid electrode situation considered here. Chandrasekaran et al. [1], adopting the well-known porous electrode models of Newman et al. [7,8], analyzed lithiation/delithiation of spherical Si electrode particles within a porous electrode. Sethuraman et al. [9] analyzed the Tafel kinetics of lithiation/delithiation and the consequent irreversibilities in crystalline Si thin films but the transient Li concentration profiles within the electrode were not considered. The transient Li concentration profiles are essential for the accurate determination of activation overpotentials and hence, the overall cell potential. In general, the porous electrode approach is not applicable for solid thin film electrodes, and, as noted in Newman's review [10], a planar diffusion problem is to be solved for dealing with the planar reaction front characteristics of solid non-porous electrodes. It should be noted that even in C/graphite electrodes (which are modeled sometimes using porous-electrode-spherical-particle framework) fabricated by binder burnout, lithiation was optically confirmed [11] to proceed by the movement of a planar reaction front, suggesting that the planar reaction front and the models based on that notion are perhaps more relevant to the Li-ion battery electrodes in general, than the spherical particle based models. Several reviews well documenting the porous electrode theory and modeling approaches have been published [12,13].

The objective of this research is to construct an analytical framework which can help to simulate easily the electrochemical charge/discharge behavior during lithiation/delithiation of a solid electrode — we demonstrate the modeling approach here using a-Si thin film electrode as an exemplar. Although numerical or COMSOL-type 3D modeling are prevalent in battery modeling, to generate a clear understanding of cell behavior and how it is impacted by the transient/interface mass transfer effects, physically meaningful analytical models will be needed. More importantly, analytic solutions that provide closed-form relationships between dependent and independent parameters can greatly help to examine parametrically the effects of the key variables with minimal numerical effort. In this study, we have obtained exact analytical solutions for the mass transport equations describing Li transport through the planar Si electrode, while satisfying appropriate boundary conditions. The analytical modeling framework, comprising these solutions, is used to closely simulate the Li-ion cell behavior and to illustrate how diffusion limitations and activation overpotentials affect the electrochemical performance. It is shown here that (i) the available experimental charge/discharge data, especially for a wide range of C-rates, can be simulated quite well and (ii) the hysteretic effects that amplify at higher C-rates can be largely attributed to the electrode-diffusion limitations. Further, using the modeling framework, we have examined the effect of the Li diffusion coefficient and the standard rate constant for charge transfer on the lithiation/delithiation capacities at different C-rates.

2. The a-Si/Li half-cell

Fig. 1(a) and (b) shows the modeling configuration of the electrochemical half-cell during discharge and charge cycles, respectively. Here, a-Si is the positive electrode and Li is the negative electrode with a liquid electrolyte transporting Li$^+$ ions between the two electrodes. The lithiation/delithiation is assumed to occur under a steady state flux of Li$^+$ to and from the a-Si electrode. It is also assumed that the continuous insertion of Li occurs by solid-state diffusion within the electrode, leading to the amorphous solid solution of the form, Li$_x$Si, with $0 < x < 3.75$.

In the modeling approach, first, analytical solutions for transient Li concentration profiles within the a-Si electrode, as a function of state of charge/discharge, are derived. Secondly, the instantaneous surface Li concentrations of the electrode (at the electrode–electrolyte interface), obtained from these profiles, are used to determine the corresponding activation overpotentials using the Butler–Volmer (B–V) equation. Finally, these overpotentials are added to the equilibrium charge/discharge potential to determine the actual potential over the period of charge/discharge.

It is to be noted that the overall cell potential is taken as the sum of the activation overpotential at the a-Si electrode surface and the electrode equilibrium potential. This is justified because the activation overpotential at the Li/electrolyte interface is very low [14] due to the high equilibrium exchange current density value for Li deposition/removal. Further, the overpotentials associated with mass transport of Li$^+$ in the electrolyte were calculated as per the Nernst–Planck equation [15]— they were found to be in the range of 10^{-6}–10^{-4} V, which are three orders of magnitude lower than the activation overpotential at the a-Si/electrolyte interface. Hence, the overpotentials at the Li/electrolyte interface and for Li$^+$ transport within the electrolyte can be safely ignored for the present purposes.

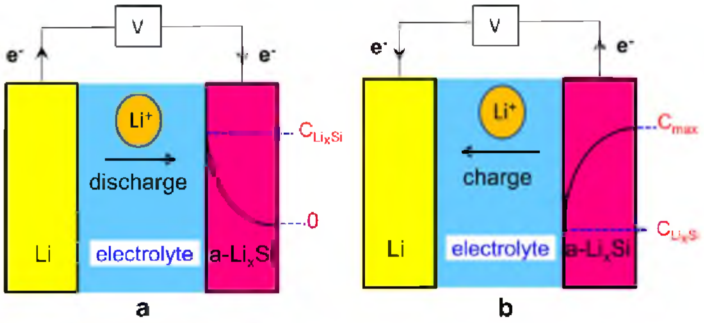

Fig. 1. Schematic of a Li-ion cell with a-Si as positive electrode and Li as negative electrode. The transport of Li ions is shown during (a) discharge and (b) charge.

3. Analytical models of lithiation/delithiation

Schematic transient Li concentration profiles within the a-Si electrode, during arbitrary lithiation and delithiation steps, are illustrated in Fig. 2(a) and 2(b), respectively. At any time, the transient profiles should satisfy Fick's second law:

$$\frac{\partial C}{\partial t} = D\frac{\partial^2 C}{\partial y^2} \tag{1}$$

where y is the position along the thickness direction of electrode, $C(y, t)$ is the Li concentration at location y within the electrode at time t, and D is the diffusivity of Li in $\mathrm{Li}_x\mathrm{Si}$ (assumed to be constant for all x).

First, lithiation of the electrode is considered — the initial and the boundary conditions are: (i) initial Li concentration is zero, (ii) steady state Li flux exists in the electrolyte under current I, and (iii) Li flux is zero at the electrode surface attached to the current collector. These conditions are specified by Equations (2)–(4).

$$C(y, t = 0) = 0 \tag{2}$$

$$-D\left.\frac{\partial C}{\partial y}\right|_{y=0} = \frac{I}{\mathrm{FS}} \tag{3}$$

$$\left.\frac{\partial C}{\partial y}\right|_{y=L} = 0 \tag{4}$$

where F is the Faraday's constant, S is the surface area and L is the thickness of the electrode.

In the subject of heat transfer, solutions for problems with complex boundary conditions have been obtained using the method of separation of variables [16]. Using this approach, the solution for Fick's law (Equation (1)) can be written as

$$C(y, t) = [A\cos(\lambda y) + B\sin(\lambda y)]\exp\left(-\lambda^2 Dt\right) \tag{5}$$

where λ, A and B are to be determined using the conditions (2)–(4). Using the boundary condition (3) in Equation (5),

$$B\lambda\exp\left(-\lambda^2 Dt\right) = -\frac{I}{\mathrm{DFS}} \tag{6}$$

Equation (6) can be satisfied only if $B = 0$, and if there is another function, $u(y, t)$, such that

$$C(y, t) = A\cos(\lambda y)\exp\left(-\lambda^2 Dt\right) + u(y, t) \tag{7}$$

and that

$$-D\left.\frac{\partial u}{\partial y}\right|_{y=0} = \frac{I}{\mathrm{FS}} \tag{8}$$

Using the boundary condition (4) in Equation (7),

$$-A\lambda\sin(\lambda L)\exp\left(-\lambda^2 Dt\right) + \left.\frac{\partial u}{\partial y}\right|_{y=L} = 0 \tag{9}$$

The above equation is satisfied only if $\lambda L = n\pi$ and $\left.\frac{\partial u}{\partial y}\right|_{y=L} = 0$ simultaneously. The general form of the solution can be represented as an infinite series. One possible solution for **u** (y, t), which satisfies Equations (1), (3) and (4), is

$$u(y, t) = \frac{I}{\mathrm{FSL}}t + \frac{I}{2\mathrm{DFSL}}(y - L)^2 \tag{10}$$

Thus, the general form of $C(y, t)$ will have to be

$$C(y, t) = \frac{I}{2\mathrm{DFSL}}(y - L)^2 + \frac{I}{\mathrm{FSL}}t + \sum_{n=0}^{\infty} A_n\cos\left(\frac{n\pi}{L}y\right) \times \exp\left(-\frac{n^2\pi^2}{L^2}Dt\right)$$

The values of coefficients A_n $(n = 0, 1, 2\ldots)$ can be derived from the initial condition (2), through Fourier series expansion. The final solution for concentration profile, thus obtained, is:

$$C(y, t) = \frac{I}{\mathrm{FSL}}t - \frac{IL}{6\mathrm{DFS}} + \frac{I}{2\mathrm{DFSL}}(y - L)^2 - \frac{2IL}{\pi^2\mathrm{DFS}}\sum_{n=1}^{\infty}\frac{1}{n^2}\cos\left(\frac{n\pi}{L}y\right)\exp\left(-\frac{n^2\pi^2}{L^2}Dt\right) \tag{11}$$

Equation (11) is a general expression for the development of transient Li concentration profiles as a function of time upon lithiation by steady state Li flux in the electrolyte. Next, the case of subsequent delithiation of the lithiated electrode is considered — the initial and boundary conditions are:

$$C(y, t = 0) = f(y) \tag{12}$$

$$-D\left.\frac{\partial C}{\partial y}\right|_{y=0} = -\frac{I}{\mathrm{FS}} \tag{13}$$

$$\left.\frac{\partial C}{\partial y}\right|_{y=L} = 0 \tag{14}$$

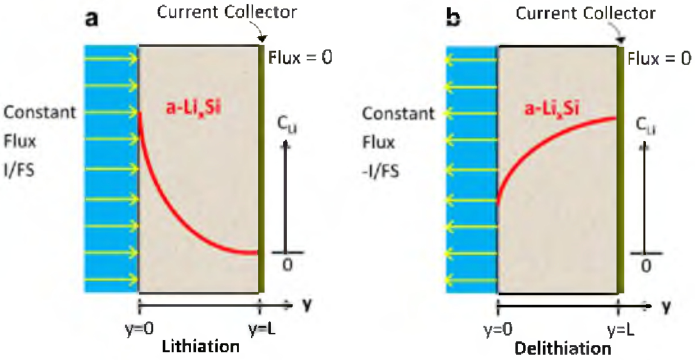

Fig. 2. Schematic of arbitrary transient Li concentration profiles within the a-Si thin film electrodes during (a) lithiation, and (b) delithiation under a constant Li-ion flux.

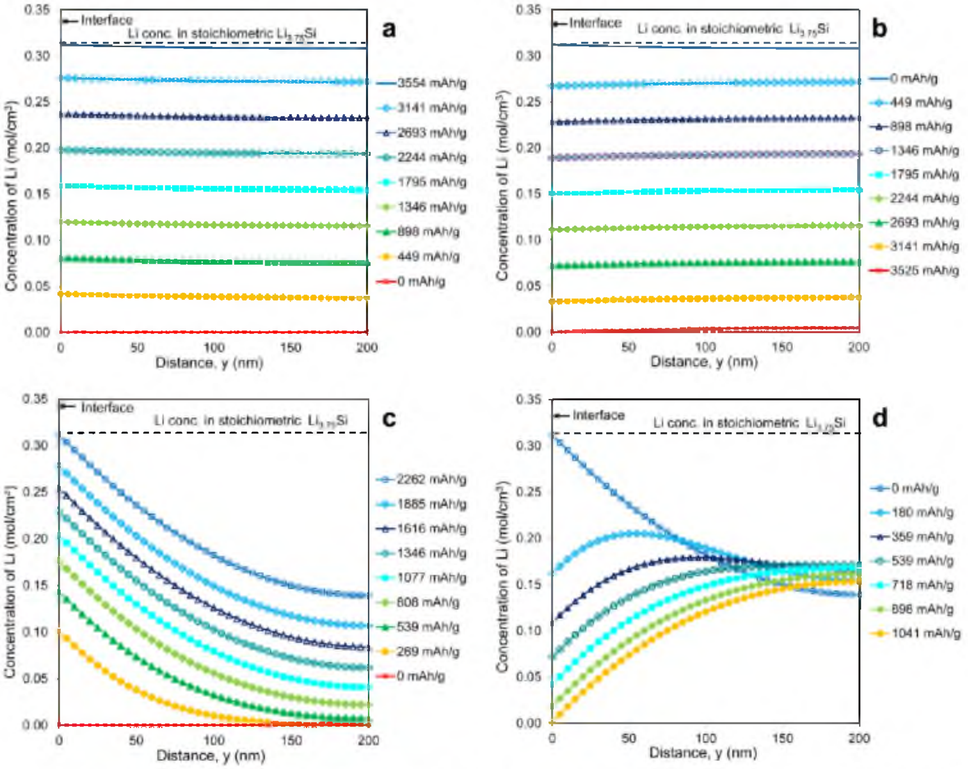

Fig. 3. The development of transient Li concentration profiles at different states of charge/discharge within a 200 nm thick a-Si thin film electrode with $D = 10^{-13}$ cm^2 s^{-1} (a) and (b) are during lithiation and subsequent delithiation, respectively, at C/40 rate, 0.0043 mA cm^{-2} and (c) and (d) are during lithiation and subsequent delithiation, respectively, at 1 C rate, 0.17 mA cm^{-2}.

Here, $f(y)$ is the transient Li concentration profile at the last step of the lithiation cycle which is taken as the initial Li concentration profile for the delithiation cycle, in order to mimic the sequence of charge–discharge process of a cell. Again, the suitable form of concentration profile is

$$C(y,t) = [E\cos(\lambda y) + G\sin(\lambda y)]\exp\left(-\lambda^2 Dt\right) + w(y,t) \tag{15}$$

With the substitution of the two boundary conditions, Equations (13) and (14), and following the same procedure as above, the concentration profile is obtained as

$$C(y,t) = -\frac{I}{2DFSL}(y-L)^2 - \frac{I}{FSL}t + \sum_{n=0}^{\infty} E_n\cos\left(\frac{n\pi}{L}y\right) \times \exp\left(-\frac{n^2\pi^2}{L^2}Dt\right) \tag{16}$$

Equation (16) is the general form of transient Li concentration profiles upon delithiation by a steady state Li flux in the electrolyte. The values of coefficients E_n are to be determined from the initial condition (12) using the Fourier series expansion and the initial concentration profile, $f(y)$. The expression for E_n is then given by

$$E_n = \frac{2}{L}\int_0^L f(y)\cos\left(\frac{n\pi}{L}y\right)dy \tag{17}$$

When the values for E_n calculated from Equation (17) are used in Equation (16), the Li concentration profile in the electrode at any time during delithiation can be obtained.

A typical development of time-dependent Li concentration profiles in a-Si thin film electrode (200 nm electrode thickness and $D = 10^{-13}$ cm^2 s^{-1}) during lithiation and during the subsequent delithiation is illustrated in Fig. 3(a) through (d). Fig. 3(a) and (b)

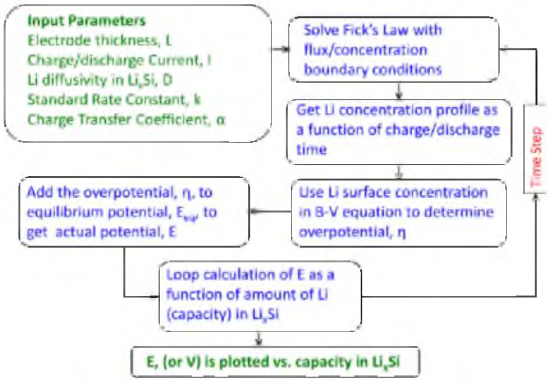

Fig. 4. The sequence of calculations in the modeling framework.

show the Li concentration profiles during lithiation/delithiation at a rate of C/40 (0.0043 mA/cm^2) whereas the profiles shown in Fig. 3(c) and (d) correspond to the 1C rate (0.17 mA/cm^2) of Li insertion and deinsertion. These profiles were determined from Equations (11), (16) and (17) at various time steps of calculation. It can be seen that for the slower C-rate of C/40, the surface Li concentration is not very different from the bulk value (Fig. 3(a) and (b)), due to Li equilibration within the electrode. However for the 1C rate, the Li profiles are highly non-linear, and in non-equilibrium due to rapid build-up/depletion of Li at the surface (Fig. 3(c) and (d)). It is also interesting to note that for the 1C-rate of Li insertion, during the last step of lithiation corresponding to the surface Li concentration reaching 0.312 mol cm ^{3}, a significant portion of the electrode (about one-third) is yet to be lithiated leading to underutilization of the storage capacity of the electrode. Similarly, at the last step of delithiation corresponding to zero surface Li concentration, considerable Li is left over within the electrode, underutilizing the Li charge available. It is also evident (Fig. 3(d)) that during the discharge period, there is a little bit of redistribution of Li due to diffusion, especially close to the electrode back surface.

4. Butler–Volmer kinetics

An electron transfer in a specific direction (oxidation/reduction) and at a specific rate can be facilitated at the electrode/electrolyte interface only if an excess potential, beyond the equilibrium electrode potential is provided [17]. The quantitative relationship between this overpotential and the oxidation/reduction current is expressed by the Butler–Volmer (B–V) equation. Accurate modeling of the Li-ion cell charge/discharge processes requires the calculation of activation overpotentials through the B–V equation—this means that the time-dependent concentration of Li at the electrode surface, obtained from the transient electrode Li concentration profile (previous section), is needed. The electrochemical charge transfer during lithiation/delithiation of Si is:

$$x\,\mathrm{Li}^{+} + x\,\mathrm{e}^{-} + \mathrm{Si} \rightleftarrows \mathrm{Li}_x\mathrm{Si} \tag{18}$$

Taking the anodic current as positive, the net current, according to the B–V equation, is

$$I_{\mathrm{net}} = I_{\mathrm{anodic}} - I_{\mathrm{cathodic}} = I_0\left(exp\left(\frac{\alpha F\eta}{RT}\right) - exp\left(\frac{-(1-\alpha)F\eta}{RT}\right)\right) \tag{19}$$

where α is the charge transfer coefficient for the anodic reaction (taken to be 0.5 here), η is the activation overpotential at the Si electrode interface, and I_0, the equilibrium exchange current density. Following the established approach [10] that was used for describing B–V kinetics in insertion electrodes, the equilibrium exchange current density can be written as

$$I_0 = \mathrm{FSk}\,[C_{\mathrm{Li}^+}]^{\alpha}[C_{\max} - C(0,t)]^{\alpha}[C(0,t)]^{1-\alpha} \tag{20}$$

where k is the standard rate constant for the charge transfer at the electrode/electrolyte interface and is a function of the forward and reverse rate constants, $C_{\mathrm{Li}+}$ is the concentration of Li^+ ions in the electrolyte (taken to be 0.001 mol cm ^{3} here), $C\,(0,\,t)$ is the time-dependent or transient concentration of Li in the Si electrode at the electrode/electrolyte interface and $C_{\max}$ is the maximum possible Li concentration in the lithiated alloy — this corresponds to the Li concentration in $\mathrm{Li}_{3.75}\mathrm{Si}$, at which the lithiation is considered to stop. The time-dependent equilibrium exchange current density from Equation (20) is used in Equation (19) along with I_{net} (or the C-rate) to determine the overpotential η and then the overall cell potential.

5. Calculation procedure

Fig. 4 illustrates the sequence of calculations involved in simulating the charge/discharge behavior using the analytical equations in previous sections. First, the values of input parameters (current, film thickness, constants related to diffusion and kinetic processes) are specified. Then, the transient Li concentration profiles within the electrode during the lithiation and delithiation periods are obtained with the help of Equations (11), (16) and (17). The surface Li concentrations, $C\,(0,\,t)$, are determined from these profiles as a function of the state of charge/discharge. These surface concentrations are then used in Equations (19) and (20) to obtain activation overpotential as a function of time over the charge/discharge period. These overpotentials are then added to the equilibrium half-cell potentials (with respect to Li/Li$^+$) to get the overall cell potential over the charge/discharge period.

It is important to highlight here how non-equilibrium conditions can develop due to diffusion limitation of active species within the solid electrode. Under equilibrium conditions, uniform Li concentration should exist within the electrode making the Li concentration at the surface facing the electrolyte necessarily equal to the bulk Li concentration of the electrode. Such conditions either exist only in a theoretical sense or are at extremely low C-rates [18] (as seen in Fig. 3(a) and (b)). Under practical operating conditions, however, the concentration profile within the electrode is highly non-linear (as seen in Fig. 3(c) and (d)) because of diffusion limitations of Li within the electrode. The electrode potential is then shifted with respect to the equilibrium value, because the electrode potential varies with $C\,(0,\,t)$. The charge/discharge current is also affected by this deviation, through the overpotential, η as in the B–V Equation (19). Therefore, to obtain the actual potential of a-Si electrode, the overpotential value (positive during charge and negative during discharge) should be added to the equilibrium voltage of a-Si (with respect to Li/Li$^+$), as a function of state of charge/discharge.

The calculations, as illustrated in Fig. 4, were performed iteratively until the end of lithiation/delithiation processes in order to obtain the cell voltage as a function of electrode capacity. The lithiation and delithiation processes were considered to stop at the reaching of the limiting potentials corresponding to 0 V and 1 V vs. Li/Li$^+$ respectively. The important input to the modeling is the equilibrium electrode potentials, as a function of Li content in the electrode — ideally this may be obtained from thermodynamic experiments, but for electrochemical purposes, galvanostatic charge/discharge tests, done using a-Si thin film electrodes at very low C-rates can be used. Here, the first cycle charge/discharge data at C/48 rate [6] is used as the equilibrium voltage data. The standard rate constant, k, is back calculated from the reported values of the equilibrium exchange current density [19] (0.7–1.3 A m ^{2} during delithiation at 0.390 V), with the help of Equation (20). There are no other adjustable parameters in the model.

6. Comparison of the simulated and the experimental cell behavior

In order to validate the model, three sets of experimental data, [19–21], corresponding to the first cycle charge/discharge behavior of a-Si film electrodes with varying thicknesses, cycled at different C-rates, were chosen. Table 1 shows a list of the values of the parameters used in the simulation. The value of diffusion coefficient of Li in a-Si films was determined to be about 10 ^{13} cm^2 s ^{1} [5,19,22], hence this value was used. The simulated charge/discharge potentials (solid lines) of a typical electrochemical cycle are compared with the experimental data (points), as shown in Fig. 5(a), (b) and (c). Overall, the simulations reproduce well the experimentally

Table 1
List of parameters and their values used in the model.

D, Li diffusion coefficient in Li_xSi	10^{-13} cm^2 s^{-1}
k, standard rate constant	10^{-7} $cm^{2.5}$ $mol^{-0.5}$ s^{-1}
α, charge transfer coefficient	0.5
C_{max}, maximum Li concentration in Li_xSi	0.312 mol cm^{-3}
C_{Li+}, Li concentration in electrolyte	0. 001 mol cm^{-3}
S, surface area	1 cm^2
F, Faraday's constant	96485 Coulombs mol^{-1}

observed lithiation/delithiation behavior. This agreement is quite encouraging, particularly in light of the fact that there are no "adjustable parameters". The volume changes during lithiation of amorphous Si are more homogeneous and uniform than that for crystalline Si. Hence this effect is not expected to impact much the charge/discharge behavior here.

Some interesting observations emerge from Fig. 5. The simulated data (or the expt. data) for the thicker electrode charged/discharged at a relatively slow rate (Fig. 5(a)) is nearly the same as the thinner electrode discharged at a relatively higher rate (Fig. 5(b)). Evidently, the level of Li insertion/depletion in a thin electrode can be achieved to the same capacity in an electrode that is thicker, but with a slower charge/discharge rate. This means that diffusion of Li within the electrode is responsible for this contrasting behavior — active species can be effectively inserted/depleted if diffusion distances are shorter, following the general relationship: $y \propto (Dr)^{1/2}$.

An intriguing observation is that the simulated delithiation voltage curve at 1 C rate (Fig. 5(c)) shows an electrode-diffusion-limitation, which is indicated by a steep increase in voltage. In this case, the cell potential during delithiation increases rapidly from 0.6 V to 1 V, limiting the capacity to about 2000 mAh g^{-1}. At this C-rate, during delithiation, the relatively high flux of Li rapidly depletes the electrode surface Li concentration at a rate faster than that can be supplied to the surface by bulk diffusion. Such a limitation did not exist in Fig. 5(a) and (b). Hence, the electrode-

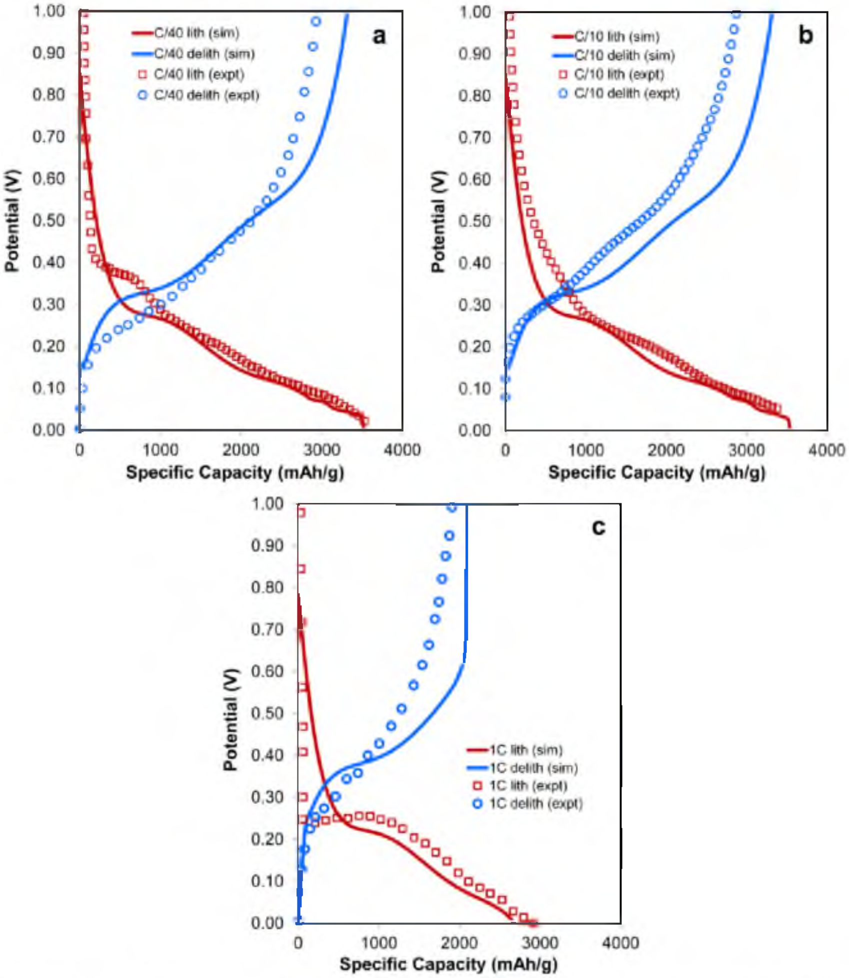

Fig. 5. Comparison of simulation results (lines) with experimental data (points) of first cycle charge/discharge potentials of a-Si film electrodes with the following thicknesses and C-rates: (a) 275 nm at C/40 (b) 100 nm at C/10 (c) 150 nm at 1 C.

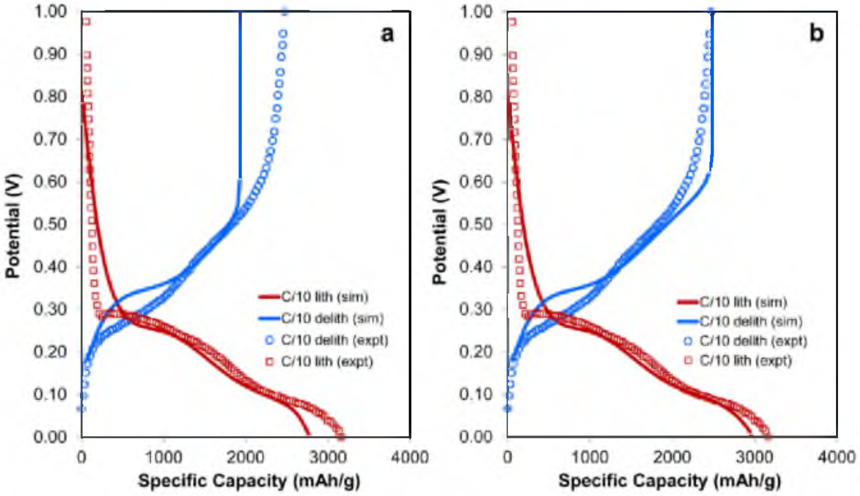

Fig. 6. Comparison of simulation results (lines) with experimental data (points) of first cycle charge/discharge voltages of (a) a 500 nm thick a-Si film electrode at C/10 rate with a Li diffusion coefficients of 10^{-13} cm^2 s^{-1} and (b) the same electrode with the diffusion coefficient of 1.5×10^{-13} cm^2 s^{-1}.

diffusion-limitation can be considered to be important primarily under two conditions: (i) when the C-rate is sufficiently high (e.g. 1C rate in Fig. 5(c)), and (ii) when the electrode thickness is too high, where large gradients in Li concentration might be expected.

Another way of looking at the capacity-limitation due to electrode-diffusion-limitation in thicker electrodes can be illustrated using Fig. 6(a) and (b). Here, even at a nominal C-rate of C/10, we see (by comparing Figures 6(a) and 5(b)) that the delithiation capacity in the simulated curve rapidly approaching to <2000 mAh g^{-1} because of a thicker a-Si film used (500 nm). For the thicker electrode, an increased diffusion distance for mass transport of Li leads to build-up of excess Li during lithiation, or rapid depletion of Li during delithiation, at the electrode-electrolyte interface. It is well known [5,23,24] that the electrochemical performance of a-Si film anodes is severely degraded with increasing film thickness. This degradation is usually attributed to volume changes and the pulverization of the electrode [5,23,24]. However, the results of our simulations strongly suggest that diffusion limitations within thicker a-Si electrodes also play an important role in reducing the lithiation/delithiation capacities.

For thicker electrodes, an increase in Li diffusivity can overcome the diffusion limitation — to illustrate this, the results of simulations obtained for the same conditions of Fig. 6(a) (for the same C rate, C/10 and thickness, 500 nm), but with a slightly higher Li diffusion coefficient 1.5×10^{-13} cm^2 s^{-1}, are compared with the experimental data (Fig. 6(b)). It can be seen that the simulated data agreed better with the actual experimental data (Fig. 6(b)) whereas in Fig. 6(a), the delithiation capacity is underestimated, when a lower value of diffusivity was used. This is important in electrode design, because considerable variation in diffusivity values due to electrode microstructure parameters (particle or phase or grain boundaries and other such short diffusion paths) can be expected. The Li diffusivity also depends on the thin film synthesis technique (CVD, Sputtering, PLD, etc.) [22].

7. Hysteresis between charge-discharge curves

The lithiation/delithiation processes of an electrode, when simulated at different C-rates also enable us to study the hysteretic behavior during cell cycling. This effect has been analyzed before for crystalline Si electrodes, but those simulations were either done on the basis of the porous electrode theory [1] or for a thin film electrode without considering electrode Li diffusion [9], which strictly do not apply to the solid non-porous a-Si electrodes. To investigate hysteretic behavior, simulations of first cycle lithiation/delithiation cell potentials for a 200 nm thick a-Si film (with Li diffusivity of 10^{-13} cm^2 s^{-1}) for C-rates ranging from C/40 to 2 C were performed. The simulated behavior is shown in Fig. 7. As the C-rate is increased, both the lithiation and delithiation capacities are reduced, and this can be primarily attributed to the electrode-diffusion-limitation. The drop in cell capacity becomes drastic at C-rates higher than C/5. A steep increase in voltage is an indicator of diffusion-limitation within the electrode and it can be seen for the delithiation curves at C/2, 1 C and 2 C rates. The difference between the lithiation and delithiation capacities also becomes increasingly large as the C-rate is increased. This is because, in the simulations,

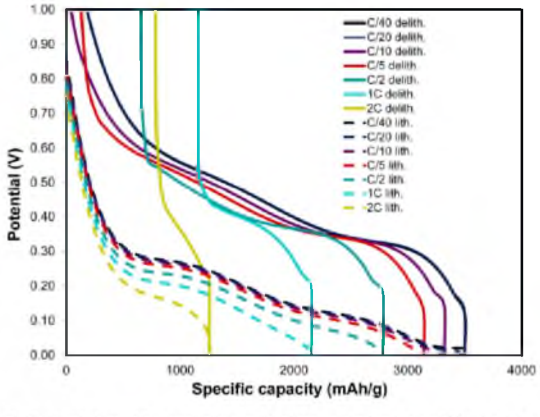

Fig. 7. Simulations of first cycle lithiation/delithiation hysteresis for a 200 nm thick a-Si film with a Li diffusivity value of 10^{-13} cm^2 s^{-1} at different C-rates between C/40 to 2 C.

electrode lithiation is performed before delithiation. Thus, any reduction in storage capacity due to rapid Li accumulation at electrode surface (in contact with the electrolyte) at higher C-rates also sets up a reduced initial capacity for the delithiation step. This is because the non-linear Li concentration profile within the electrode at the last step of lithiation becomes the input for the subsequent delithiation, as in real battery cycles. Thus the electrode-diffusion-limitation can mutually affect lithiation and delithiation, which is a natural sequence of electrode processes and can contribute significantly to the capacity fading of electrodes with repeated charge-discharge cycles. The structure of model/simulations where the last step of lithiation forms the input for the subsequent delithiation step allows one to examine capacity degradation with the cycling of the cell.

8. Effect of diffusion coefficient on lithiation/delithiation capacities

The modeling framework also allows us to systematically examine the effect of electrode/interface parameters such as diffusion coefficient and standard rate constants on the lithiation/delithiation capacities. Fig. 8 shows the lithiation and the subsequent delithiation capacities simulated for a 200 nm thick a-Si electrode at different C-rates for the choice of three Li diffusivity values: 2×10^{-13}, 1×10^{-13}, and 5×10^{-14} $cm^2\ s^{-1}$. Generally in literature [25,26] the estimated diffusion coefficient of Li in amorphous Si is found to range anywhere between 10^{-11} and 10^{-13} $cm^2\ s^{-1}$ — this means that considerable variation on electrode capacity/performance can be expected solely from microstructural factors that primarily affect Li diffusivity in electrode. Although a much narrower range of 5×10^{-14} to 2×10^{-13} $cm^2\ s^{-1}$ (yet variation by a factor of four) has been reported recently [19,22], it is instructive to evaluate the effect of diffusivity on cell behavior both during charge and discharge processes. In Fig. 8, it can be seen that at the lowest C-rates considered in the simulation, the lithiation/delithiation capacities for electrodes with three diffusivities are not very different, indicating that any variation in electrode microstructures that affect Li diffusivity (in the above range) will not impact cell performance at the lowest C-rates. However, at higher C-rates (>C/10) the effect of variation in diffusivity is quite remarkable — the capacity for the electrode with the lowest diffusivity ($D = 5 \times 10^{-14}$ $cm^2\ s^{-1}$) drops more rapidly than that with the highest diffusivity ($D = 2 \times 10^{-13}$ $cm^2\ s^{-1}$). This can be rationalized on the basis of rapid Li accumulation/depletion at the electrode surface facing the electrolyte during lithiation/delithiation steps.

An interesting observation in Fig. 8 is the asymmetry of lithiation/delithiation behavior at the highest C-rates. For the high C-rates of 1 C and 2 C, the lithiation capacities of the a-Si electrode with $D = 2 \times 10^{-13}$ $cm^2\ s^{-1}$ are quite higher than those of the electrodes with $D = 1 \times 10^{-13}$ $cm^2\ s^{-1}$; however, the corresponding delithiation capacities of the two electrodes for these C-rates are comparable. Although the last inserted transient Li concentration profile forms the input at the beginning of the delithiation cycle, the diffusion limitation plays a significant role even at high diffusivity values — that is, although the stored capacity may be high, removable capacity is quite less if removed at a faster rate. Thus, the effect of diffusion limitation is more severe during delithiation, especially at high C-rates, due to the coupled effect of reduced initial available (or stored) capacity and the rapid rate of Li depletion.

9. Effect of standard rate constant on lithiation/delithiation capacities

The standard rate constant, *k*, is a charge transfer parameter that indicates the kinetic facility of the charge transfer at the electrode-electrolyte interface. For lithiation/delithiation to occur smoothly, its values should be of the right magnitude and the rate of charge transfer should be commensurate with the Li transport within the electrode, if the electrode storage/discharge capacities are to be maximized. Fig. 9 shows the first cycle lithiation and delithiation capacities of a 200 nm thick a-Si film with a Li diffusivity of 1×10^{-13} $cm^2\ s^{-1}$ and with standard rate constant values of 10^{-7} and 10^{-8} $cm^{2.5}\ mol^{-0.5} s^{-1}$, plotted as a function of C-rate. These values of the standard constants were calculated approximately from the range of equilibrium exchange current densities reported [19,27] for lithiation of a-Si.

As seen in Fig. 9, the lithiation and delithiation capacity curves for the electrode with $k = 10^{-8}$ $cm^{2.5}\ mol^{-0.5}\ s^{-1}$ appear to be significantly shifted down with respect to those of the electrode with $k = 10^{-7}$ $cm^{2.5}\ mol^{-0.5}\ s^{-1}$ at all C rates. It is therefore evident

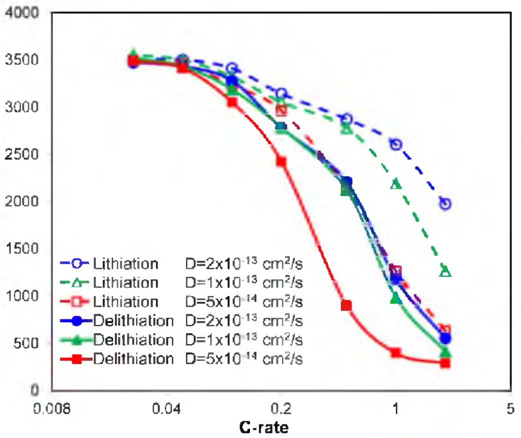

Fig. 8. First cycle lithiation and delithiation capacities of a 200 nm thick a-Si film with three Li diffusivity values: 2×10^{-13}, 1×10^{-13}, and 5×10^{-14} $cm^2\ s^{-1}$, plotted as a function of C-rate on a log-scale.

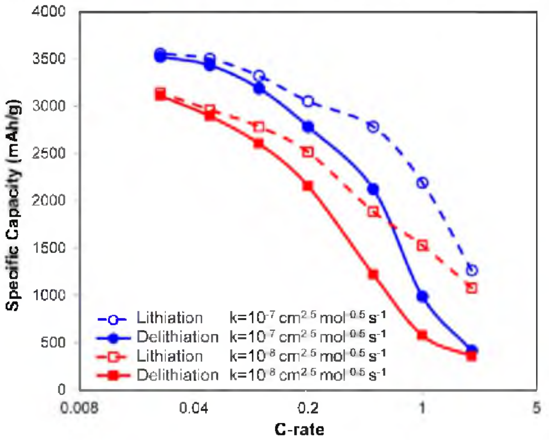

Fig. 9. First cycle lithiation and delithiation capacities of a 200 nm thick a-Si film with a Li diffusivity of 1×10^{-13} $cm^2\ s^{-1}$ and with standard rate constants, (*k*): 10^{-7} and 10^{-8} $cm^{2.5}\ mol^{-0.5}\ s^{-1}$, plotted as a function of C-rate on a log-scale.

that a low value of the standard rate constant for the lithiation/delithiation reactions will adversely affect the capacities even at low C-rates, unlike the electrode-diffusion-limitation which usually appears only at higher C-rates.

To be more accurate or relevant, further experiments or characterizations of solid electrodes are necessary to determine the values of the equilibrium exchange current densities during charge and discharge as a function of voltage for solid electrodes in Li-ion cells. In that case, the standard rate constant can be estimated from a relation, such as the one given in Equation (20).

10. Conclusions

(1) A complete analytical modeling framework for predicting the charge/discharge potential behavior of a-Si thin film electrodes during lithiation/delithiation processes has been developed. The model utilizes two important steps: (i) explicit consideration of transient Li concentrations within the electrode determined by solving diffusive mass transport equations and (ii) the determination of time-dependent activation overpotentials, as calculated from the Butler–Volmer equation.

(2) The simulated charge/discharge potential variation as a function of capacity agreed well with the experimental data of lithiation/delithiation voltages of a-Si film electrodes of different thicknesses and different C-rates.

(3) It was shown that the modeling can simulate the hysteresis between charge/discharge voltage curves at different C-rates for a-Si film electrode. The simulations demonstrate that at higher C-rates, the increases in the electrode activation overpotentials due to rapid Li build-up/depletion at the electrode surface cause widening of the hysteresis loop whereas electrode-diffusion-limitations lead to reduced capacities.

(4) The effect of C-rate on the lithiation/delithiation capacities was assessed for a-Si electrodes with different diffusivities and standard rate constants. It was found that electrode-diffusion-limitation is more important during delithiation than during the lithiation step, especially at higher C-rates. A reduction in the value of the standard rate constant, on the other hand, caused reduction in both lithiation and delithiation capacities at all C-rates.

(5) The structure of model/simulations where the last step of lithiation forms the input for the subsequent delithiation step allows one to examine capacity degradation with the cycling of the cell.

Acknowledgment

The research was partially supported through a grant from the DOE Office of Science, U.S. Department of Energy, DE-SC0008681.

References

[1] R. Chandrasekaran, A. Magasinski, G. Yushin, T.F. Fuller, J. Electrochem. Soc. 157 (2010) A1139–A1151.
[2] L.Y. Beaulieu, K.W. Eberman, R.L. Turner, L.J. Krause, J.R. Dahn, Electrochem. Solid-State Lett. 4 (2001) A137–A140.
[3] L.Y. Beaulieu, K.C. Hewitt, R.L. Turner, A. Bonakdarpour, A.A. Abdo, L. Christensen, K.W. Eberman, L.J. Krause, J.R. Dahn, J. Electrochem. Soc. 150 (2003) A149–A156.
[4] M. Green, E. Fielder, B. Scrosati, M. Wachtler, J.S. Moreno, Electrochem. Solid-State Lett. 6 (2003) A75–A79.
[5] H. Xia, S. Tang, L. Lu, Mater. Res. Bull. 42 (2007) 1301–1309.
[6] T.D. Hatchard, J.R. Dahn, J. Electrochem. Soc. 151 (2004) A838–A842.
[7] J. Newman, K.E. Thomas-Alyea, Electrochemical Systems, Wiley-Interscience, New Jersey, 2004, pp. 517–565.
[8] J. Newman, W. Tiedemann, AlChE J. 21 (1975) 25–41.
[9] V.A. Sethuraman, V. Srinivasan, J. Newman, J. Electrochem. Soc. 160 (2013) A394–A403.
[10] K. Thomas, J. Newman, R. Darling, Advances in Lithium-ion Batteries, 2002, pp. 345–392.
[11] S.J. Harris, A. Timmons, D.R. Baker, C. Monroe, Chem. Phys. Lett. 485 (2010) 265–274.
[12] M. Doyle, J. Newman, J. Appl. Electrochem. 27 (1997) 846–856.
[13] G.G. Botte, V.R. Subramanian, R.E. White, Electrochim. Acta 45 (2000) 2595–2609.
[14] N. Munichandraiah, L.G. Scanlon, R.A. Marsh, J. Power Sources 72 (1998) 203–210.
[15] D. Danilov, P.H.L. Notten, Electrochim. Acta 53 (2008) 5569–5578.
[16] H.S. Carslaw, J.C. Jaeger, Conduction of Heat in Solids, Oxford University Press, Oxford, 1959, pp. 92–132.
[17] A.J. Bard, L.R. Faulkner, Electrochemical Methods: Fundamentals and Applications, Wiley, New York, 1980.
[18] D. Danilov, R.A.H. Niessen, P.H.L. Notten, J. Electrochem. Soc. 158 (2011) A215–A222.
[19] J. Li, X. Xiao, F. Yang, M.W. Verbrugge, Y.T. Cheng, J. Phys. Chem. C 116 (2011) 1472–1478.
[20] L.B. Chen, J.Y. Xie, H.C. Yu, T.H. Wang, J. Appl. Electrochem. 39 (2009) 1157–1162.
[21] S. Ohara, J. Suzuki, K. Sekine, T. Takamura, J. Power Sources 136 (2004) 303–306.
[22] J. Xie, N. Imanishi, T. Zhang, A. Hirano, Y. Takeda, O. Yamamoto, Mater. Chem. Phys. 120 (2010) 421–425.
[23] J. Li, A.K. Dozier, Y. Li, F. Yang, Y.-T. Cheng, J. Electrochem. Soc. 158 (2011) A689–A694.
[24] J.P. Maranchi, A.F. Hepp, P.N. Kumta, Electrochem. Solid-State Lett. 6 (2003) A198–A201.
[25] K. Yoshimura, J. Suzuki, K. Sekine, T. Takamura, J. Power Sources 146 (2005) 445–447.
[26] T. Zhang, H.P. Zhang, L.C. Yang, B. Wang, Y.P. Wu, T. Takamura, Electrochim. Acta 53 (2008) 5660–5664.
[27] M. Pharr, K. Zhao, X. Wang, Z. Suo, J.J. Vlassak, Nano Lett. 12 (2012) 5039–5047.

CHAPTER 6

INTEGRATED ANALYTICAL MODELING AND SIMULATION OF ELECTROCHEMICAL OPERATIONAL CHARACTERISTICS OF LI-ION CELLS WITH GRAPHITE/LIFEPO$_4$ ELECTRODES

(Manuscript in preparation)

6.1 Introduction

Effective design of Li-ion batteries, including maximum utilization of storage capacities and their repeatability over a large number of cell cycles, can be accomplished only with a quantitative understanding of the electrochemical processes occurring in the entire cell, especially the charge/discharge characteristics. An integrated modeling framework that simultaneously includes the Li transport and electron transfer effects in both the electrodes is essential in this regard. Such modeling can provide new insights into the effect of each electrode on the overall cell behavior.

A large body of modeling of lithiation/delithiation characteristics of electrodes in Li-ion batteries is based on the well-known Newman's porous electrode theory[1, 2]. In these models, the inherent assumption is that the solid electrode consists of spherical particles with each particle having access to electrolyte and current collector[3]. Li insertion/removal is assumed to occur by solid-state diffusion across these individual spherical particles[4]. Lithiation/delithiation is thus assumed to occur across all particles simultaneously, with the limiting diffusion distance being of the order of the particle radius. Electrolyte is considered to be in contact with all the particles throughout the electrode. The Li^+ ion transport through the liquid electrolyte is considered to follow the concentrated solution theory.

The assumption of diffusion of Li through individual spherical electrode particles is not supported by the experimental observations. For instance, Srinivasan and Newman [5] proposed a spherical "shrinking-core" model to describe lithiation of $FePO_4$ particles. However, transmission electron microscopy[6] and high-resolution electron energy loss microscopy [7] investigations of $LiFePO_4$ electrodes reveal that the transformation from

$LiFePO_4$ to $FePO_4$ occurs in a one-dimensional fashion with the phase boundary separating the lithiated and delithiated regions moving across the electrode as a macroscopic front. Also, several modeling works in literature[5, 8-10] solve for Li transport across nanometer-sized particles, with adjusted current density values. The adjusted current density comes as a consequence of the assumption that the state of charge/discharge of a particular particle is representative of the state of charge/discharge of the entire electrode. Such an assumption is very difficult to justify both on theoretical and experimental grounds. More recently, Harris *et al.*[11] observed the motion of a planar lithiation front in a porous graphite electrode by in situ optical microscopy. The presence of such a front strongly suggests that the electrode particles closer to the separator are lithiated first, followed by the planar movement of the lithiation front across the electrode thickness and towards the current collector. Hence, the assumption of uniform current density across the entire electrode, as implied in the spherical particle model appears to be unrealistic for electrodes in Li-ion cells.

Harris *et al.* [11], in their work also developed a macroscale model to describe Li transport through the entire electrode in a planar fashion. The microscopic Li diffusion and migration processes through liquid phase and solid phase within the electrode were not considered individually. Instead, an effective diffusion coefficient value for the Li ions through the porous electrode was used. This model was reasonably successful in predicting Li transport within graphite electrode.

In view of the preceding discussion, it is clear that a macrohomogeneous model that considers planar Li diffusion within the electrode is a better choice to describe lithiation/delithiation characteristics of the electrodes in a Li-ion cell. In such mathematical models, it is preferable to deal with analytical solutions for Li transport because they provide closed-form relationships between dependent and independent variables. Such relationships enable easy parametric evaluation of electrode variables that affect their electrochemical performance. In the context of modeling of Li-ion batteries, such a model can explicitly show the effect of the key parameters (e.g., diffusion coefficient, Butler-Volmer rate constant, electrode thickness and C-rate) on the overall cell performance. In the porous electrode theory, the governing equations with their boundary conditions are not amenable to analytical solutions and have to be solved numerically[1]. Further several assumptions and transformations have to be made to fit the spherical particle lithiation into the overall lithiation of the electrode, the consequences of which are not readily obvious.

The objective of the present work is to develop an integrated analytical modeling framework, to describe the electrochemical discharge behavior of a Li-ion cell consisting of $LiFePO_4$ cathode and graphite anode. Such a model will enable the evaluation of the relative effects of the two electrodes and will help to determine the electrode effects that limit/enhance the electrochemical performance of the cell. Analysis of the cell behavior at different C-rates will help to better understand (a) which of the two electrodes limits the cell performance at higher C-rates, and (b) whether this limitation is caused due to diffusional or kinetic effects in that electrode and/or other physical aspects of the electrode including composition and thickness.

6.2 Model Development

The model electrochemical cell consists of $LiFePO_4$ cathode and graphite anode separated by liquid electrolyte, as shown in Figure 6.1. In the cell, the initial absolute

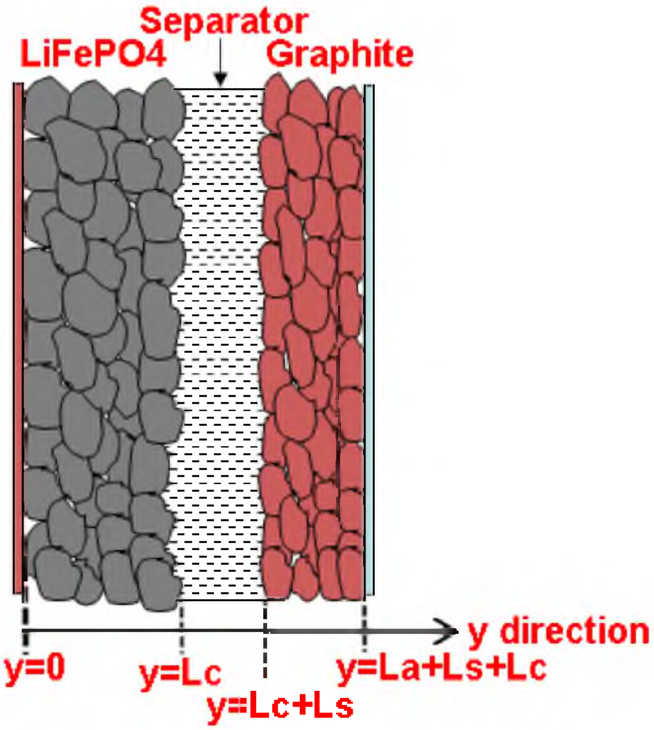

Figure 6.1 Schematic of the electrochemical cell with $LiFePO_4$ cathode, graphite anode

capacities of the two electrodes are matched, that is the amount of Li that can be stored is the same, although the electrodes will have different thicknesses. The half-cell potentials (vs. Li/Li^+) for lithiation of $LiFePO_4$ and for delithiation of LiC_6 are individually calculated and then coupled to simulate the overall $LiFePO_4/C$ cell performance. In determining the half-cell potentials, the over potentials due to B-V kinetics of charge transfer at the electrolyte-$LiFePO_4$ interface is treated in conjunction with the lithiation of $LiFePO_4$. Similarly, the over potential due to B-V kinetics at the graphite-electrolyte interface is treated in conjunction with the delithiation of graphite. The over potentials associated with Li transport through electrolyte are not considered in this model, since they are negligible when compared with the activation over potentials and ohmic losses in the electrodes. Simulations are carried for different values of the current, or the C-rate, with C here referring to the cell capacity. This work simulates only the discharge behavior of the cell, that is, the delithiation of lithiated graphite and the lithiation of $FePO_4$. However, using the approach outlined here, the cell behavior during recharging (lithiation of graphite and delithiation of $LiFePO_4$ electrodes) can also be easily modeled and simulated.

6.2.1 Modeling of Lithiation of $FePO_4$ Electrode

$LiFePO_4$ has an orthorhombic olivine lattice, which consists of interconnected and distorted LiO_6 and [12], as can be seen in Figure 6.2(a). From the structure, it is clear that the movement of Li along the [010] direction (or b-axis) would be preferred over other directions, because of the availability of one-dimensional diffusional channels [13]. This has been experimentally verified by Nishimura *et al.* [14] who demonstrated, by neutron diffraction, that Li motion is confined to the b-axis.

At room temperature, Li_xFePO_4 exists as two phases (Figure 6.2(b)): a Li-lean phase (heterosite H, denoted as α), and a Li-rich phase (triphylite, T denoted as β). The two phases have orthorhombic olivine structures, but with different lattice parameters[15]. During electrochemical cell discharge (or lithiation of $FePO_4$ or α), since the α phase has only a limited solubility of Li ($x<0.027$ in Li_xFePO_4), a β phase layer forms quickly and the β/α phase-boundary is driven into the electrode material in a planar fashion as more Li is inserted. It is obvious here that the rate of Li insertion will determine the velocity of the boundary movement. The lithiation of the electrode is then controlled by the movement of the β/α phase boundary because the kinetics of lithiation within the electrode should be commensurate with equilibrium phase transformation. The problem at hand is, therefore, the moving boundary problem of solid state diffusion with two phases separated by the moving boundary. A solution for this moving-boundary problem

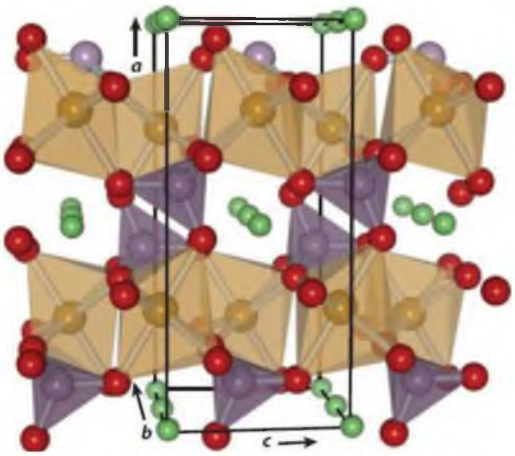

(a)

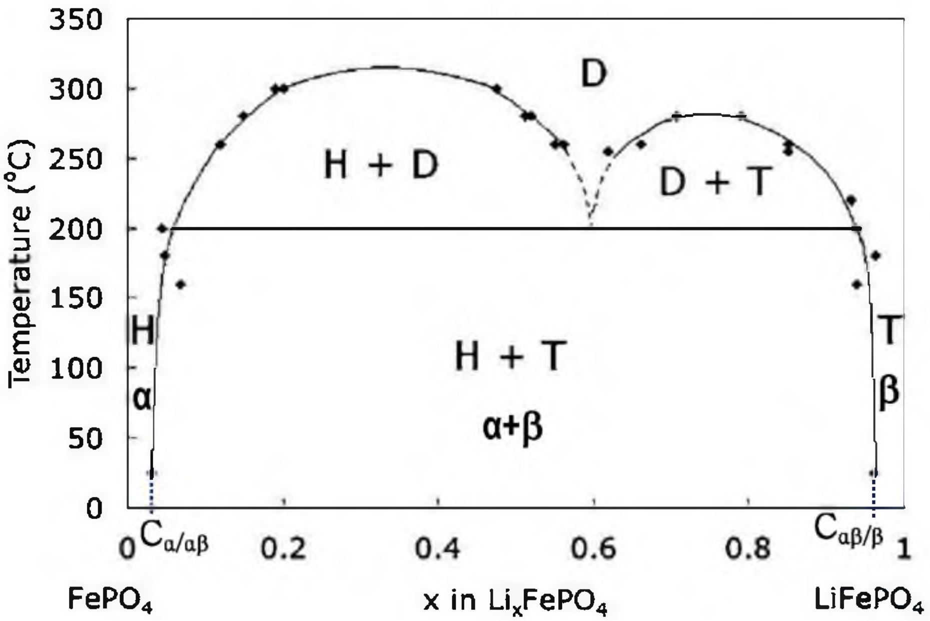

(b)

Figure 6.2 The structure and phase diagram of $LiFePO_4$. (a) shows the orthorhombic structure of $LiFePO_4$. Fe octahedra are shown in tan color, P tetrahedral in purple, Li atoms in green, and O atoms in red[16]. (b) shows the phase diagram of Li_xFePO_4. Li is solid soluble at RT up to x = 0.027 about above which a two phase region (heterosite + tryphilite) is present. Tryphilite exists for x > 0.93 in Li_xFePO_4. (a) is reprinted with permission from T. Maxisch, and G. Ceder, Physical Review- Series B-73(17), 174112, 2006. Copyright 2006 by the American Physical Society. (b) is reprinted from J. L. Dodd, R. Yazami, and B. Fultz, Phase Diagram of Li_xFePO4, Electrochemical and Solid-State Letters, 9(3), A151, 2006[17]. Reproduced by permission of The Electrochemical Society.

will involve the solutions of Fickian diffusion of Li in the two phases and a Li conservation balance at the moving two-phase boundary. The steps involved in determining these solutions will be outlined in the following section.

6.2.2 Analytical Model for Li Diffusion during Lithiation of $FePO_4$

The equilibrium lithiation of Li_xFePO_4 has to proceed through three essential stages, as shown in Figure 6.3. Initially, α phase will be lithiated (Figure 6.3(a)) until the concentration of Li at the surface exceeds the room temperature solubility limit ($C_{\alpha/\alpha\beta}$), after which a thin β-phase layer will form at the surface. In this two-phase regime, the β/α phase boundary will advance in a planar fashion across the thickness of the electrode until the original α-phase regions are entirely converted to β-phase (Figure 6.3(c)). Subsequently, the single β-phase will be lithiated until the surface concentration exceeds the maximum equilibrium solubility at room temperature in that phase. Since, both the phases have narrow compositional ranges; much of the inserted Li and its transport is involved in moving the phase-boundary through the material causing α-β phase transformation. The mathematical equations for Li diffusion and the associated Li conservation balance at the moving boundary will be developed using appropriate boundary conditions in the following sections.

6.2.2.1 Stage I. Initial α-Phase Lithiation

At any time, the transient Li concentration profile within the α-phase should satisfy Fick’s second law:

$$\frac{\partial C}{\partial t} = D_{\alpha}\frac{\partial^2 C}{\partial y^2} \tag{1}$$

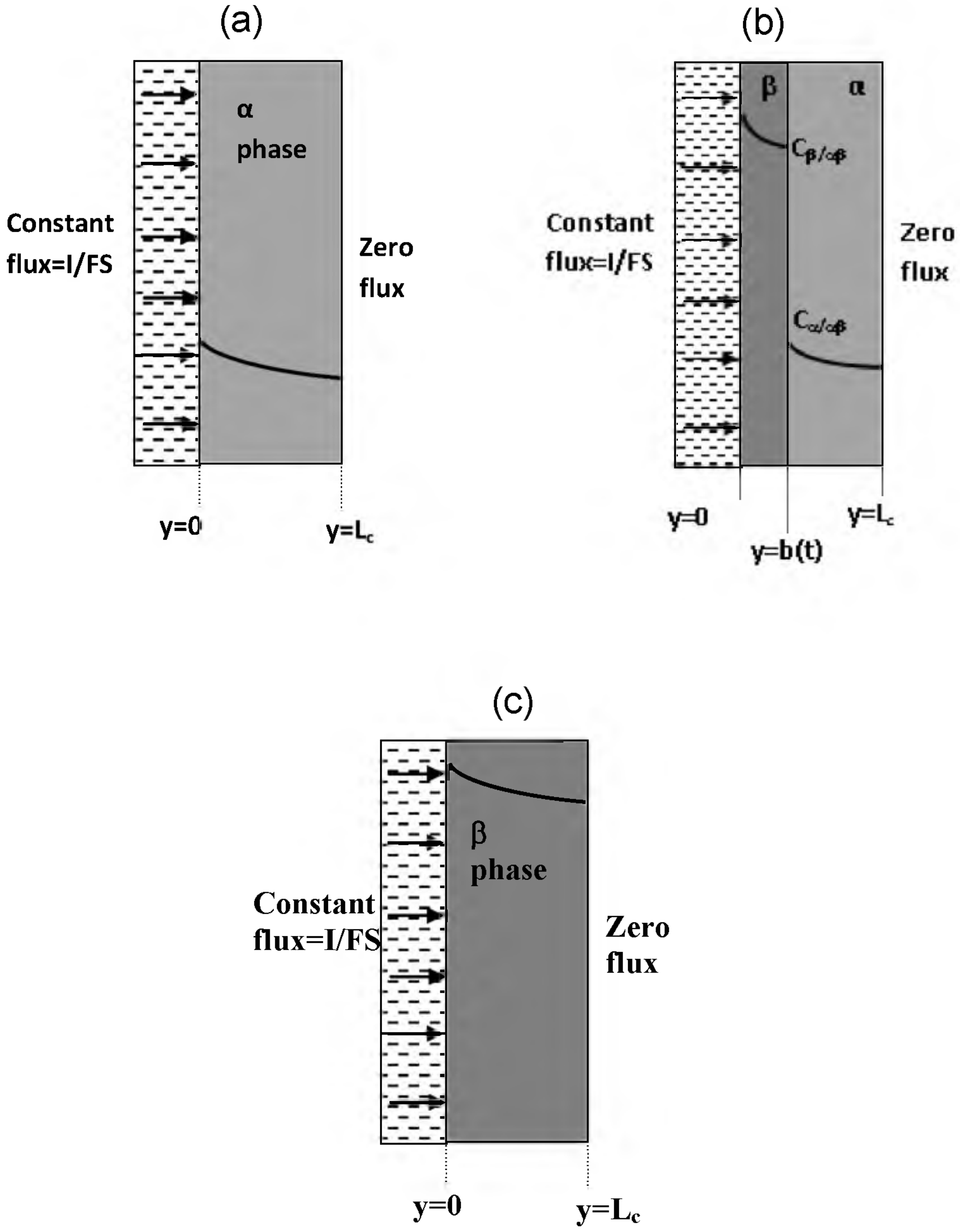

Figure 6.3 Development of Li concentration profile in Li_xFePO_4 electrode during three possible stages: (a) stage I: lithiation in single phase α, (b) stage II: lithiation in two-phase region, along with phase boundary movement and (c) stage III: lithiation in single phase β

where y is the position along the thickness direction of electrode, C(y,t) is the Li concentration at location y within the electrode at time t and D_α is the diffusivity of Li in the α-phase.

During lithiation of the α-phase (Figure 6.3(a)), the initial and the boundary conditions are: (i) initial Li concentration is zero, (ii) steady state Li flux exists in the electrolyte under current I, and (iii) Li flux is zero at the electrode surface attached to the current collector. These conditions are specified by equations (2)-(4).

$$C(y,t=0)=0 \tag{2}$$

$$-D_\alpha \left.\frac{\partial C}{\partial y}\right|_{y=0} = \frac{I}{FS} \tag{3}$$

$$\left.\frac{\partial C}{\partial y}\right|_{y=L_c} = 0 \tag{4}$$

where F is the Faraday's constant, S is the surface area of the electrode, and L_c is the thickness of the electrode. Now using the separation of variables approach, the general solution for Fick's law (equation (1)) can be written as

$$C(y,t)=[A\cos(\lambda y)+B\sin(\lambda y)]\exp(-\lambda^2 D_\alpha t) \tag{5}$$

where λ, A and B are to be determined using the conditions (2)-(4). Using the boundary condition (3) in equation (5),

$$B\lambda\exp(-\lambda^2 D_\alpha t) = -\frac{I}{DFS} \tag{6}$$

Equation (6) can be satisfied only if B = 0, and if there is another function, u(y,t), such that

$$C(y,t) = A\cos(\lambda y)\exp(-\lambda^2 D_\alpha t) + u(y,t) \tag{7}$$

and that

$$-D_\alpha \left.\frac{\partial u}{\partial y}\right|_{y=0} = \frac{I}{FS} \tag{8}$$

Using the boundary condition (4) in equation (7),

$$-A\lambda\sin(\lambda L)\exp(-\lambda^2 D_\alpha t) + \left.\frac{\partial u}{\partial y}\right|_{y=L_c} = 0 \tag{9}$$

The above equation is satisfied only if $\lambda L_c = n\pi$ and $\left.\frac{\partial u}{\partial y}\right|_{y=Lc} = 0$ simultaneously. The general form of the solution can be represented as an infinite series. One possible solution for u(y,t), which satisfies equations (1), (3) and (4), is

$$u(y,t) = \frac{I}{FSL_c}t + \frac{I}{2DFSL_c}(y - L_c)^2 \tag{10}$$

Thus, the general form of C(y,t) will have to be

$$C(y,t)= \frac{I}{2DFSL_c}(y-L_c)^2+\frac{I}{FSL_c}t+\sum_{n=0}^{\infty}A_n\cos\left(\frac{n\pi}{L_c}y\right)\exp\left(-\frac{n^2\pi^2}{L_c{}^2}Dt\right)$$

The values of coefficients A_n (n=0, 1, 2…) can be determined from the initial condition (2), through Fourier series expansion. The final solution for concentration profile, thus obtained, is:

$$C(y,t)=\frac{I}{FSL_c}t-\frac{IL_c}{6D_\alpha FS}+\frac{I}{2D_\alpha FSL_c}(y-L_c)^2-\frac{2IL_c}{\pi^2 D_\alpha FS}\sum_{n=1}^{\infty}\frac{1}{n^2}\cos\left(\frac{n\pi}{L_c}y\right) * \exp\left(-\frac{n^2\pi^2}{L_c^2}D_\alpha t\right) \quad (11)$$

Equation (11) is a general expression for the development of transient Li concentration profiles as a function of time during the lithiation of α-phase by steady state Li flux in the electrolyte.

6.2.2.2 Stage II. Lithiation in α/β Two-Phase Regime

A thin layer of β-phase will form when the surface concentration of Li at the electrolyte-$LiFePO_4$ interface exceeds the maximum lithium content in α phase ($C_{\alpha/\alpha\beta}$). After that, lithiation will occur over the α/β two-phase region (Figure 6.3(b)), with the inserted Li causing the movement of the α/β phase boundary into the electrode and towards the current collector. The Li diffusion during this two-phase regime will have to be solved for each of the phases separately. Following this, Li conservation/balance at the boundary needs to be introduced satisfying the appropriate Li compositions at either side of the phase boundary. Finally, combining of all these together will lead to an accurate description of the lithiation in the α/β two-phase region.

6.2.2.2.1 Stage II. Lithiation in β phase regions (0<y<b(t)) of the electrode.

The governing equation for the Li concentration profile within the β phase is given by:

$$\frac{\partial C}{\partial t} = D_\beta \frac{\partial^2 C}{\partial y^2} \text{ for y} \in (0, \text{b(t)}) \tag{12}$$

where D_β is the Li diffusivity in the Li-rich phase and b(t) is the time-dependent location of the moving phase boundary. The initial condition is as follows:

$$C(y,t_2) = C_{\alpha\beta/\beta} \text{ for y} \in (0, \text{b}(t_2)) \tag{13}$$

where t_2 is the time at which the β-phase layer first forms and $C_{\alpha\beta/\beta}$ is the minimum Li solubility level in β-phase. At any time $t > t_2$, the β-phase exists between x=0 and x= b(t). The boundary conditions are:

$$C(b(t),t) = C_{\alpha\beta/\beta} \text{ for y} \in (0, \text{b(t)}) \tag{14}$$

$$-D_\beta \left.\frac{\partial C}{\partial y}\right|_{y=0} = \frac{I}{FS} \tag{15}$$

It is assumed that equilibrium concentrations are maintained in the two phases on either side of the moving boundary. Following a similar approach as before, the solution for the Li concentration profile in the β phase is obtained as:

$$C(y,t) = C_{\alpha\beta/\beta} - \frac{I}{D_\beta FS}(y - b(t)) - \frac{8Ib(t)}{\pi^2 D_\beta FS}\sum_{n=0}^{\infty}\frac{1}{(2n+1)^2}\cos\left(\frac{(2n+1)}{2b(t)}\pi y\right) * \exp\left(-\frac{(2n+1)^2}{4b(t)^2}\pi^2 D_\beta (t - t_2)\right) \tag{16}$$

for y $\in$ (0, b(t)).

Equation (16) shows the general expression for the Li concentration within the β-phase as a function of time and distance (Figure 6.3(b)). It is to be noted that if the surface concentration C(0,t) exceeds C_{max}, the maximum possible Li concentration in the β-phase, lithiation will stop even if the two-phase boundary has not traveled through the entire thickness of the electrode. As a side note, this may be one of the limiting conditions due to lithium diffusion limitation within $LiFePO_4$ electrode in general, which will lead to cell potential precipitously dropping towards zero, especially at high C-rates.

6.2.2.2.2 Stage II. Lithiation in α phase regions (b(t) < y < L_c) of the electrode.

The governing equation for Li profile within the α-phase is given by:

$$\frac{\partial C}{\partial t} = D_\alpha \frac{\partial^2 C}{\partial y^2} \text{ for } y \in (b(t), L_c) \tag{17}$$

The initial condition for Li profile within the α-phase after the formation of a thin β-phase layer is:

$$C(y,t_2) = f_1(y) \text{ for } y \in (b(t_2), L_c) \tag{18}$$

where $f_1(y)$ is the Li concentration profile in the α-phase at the end of the single-phase lithiation stage (Figure 6.3(a)). The boundary conditions are:

$$C(b(t),t) = C_{\alpha/\alpha\beta} \text{ for } t > t_2 \tag{19}$$

$$\left.\frac{\partial C}{\partial y}\right|_{y=L_c} = 0 \tag{20}$$

The solution for this system of governing equation and the initial/boundary conditions is derived as:

$$C(y,t) = C_{\alpha/\alpha\beta} + \sum_{n=1}^{\infty}\left(\frac{2}{L_c - b(t)}\int_0^{Lc}(f_1(y) - C_{\alpha\beta})\sin\left(\lambda_n(y-b(t))\right)dy\right)\sin\left(\lambda_n(y-b(t))\right) \\ * \exp\left(-\lambda_n^2 D_\alpha (t-t_2)\right) \tag{21}$$

for y ∈ (b(t), L_c), $t > t_2$ and where $\lambda_n = \frac{2n+1}{2(L_c - b(t))}\pi$

Equations (16) and (21) describe the development of Li concentrations within the β-phase ($0 < y < b(t)$) and the α- phase ($b(t) < y < L_c$) but the time-dependent variation of b(t) with time is still to be determined. This is accomplished by considering a Li mass balance across the two sides of the α/β phase boundary. The idea is that if enough Li, sufficient to cause lithiation of an α layer of size "dy" causes α to β phase transition, and has accumulated at the interface, then the boundary will displace by "dy" towards the current collector. In other words, for a small time step, Δt, the accumulation of Li at the interface, driven by the differences in the Li fluxes in the two phases, will result in advancement of the α/β boundary. Mathematically, this mass conservation can be expressed as:

$$\left(C_{\alpha\beta/\beta} - C_{\alpha/\alpha\beta}\right)\frac{\Delta b}{\Delta t} = D_{\alpha}\frac{\partial C}{\partial y}\bigg|_{y=b^{+}} - D_{\beta}\frac{\partial C}{\partial y}\bigg|_{y=b^{-}} \tag{22}$$

where Δt is the time step and Δb is the advancement in the location of the phase boundary for the duration of the time step. The value of b(t) is iteratively updated in the simulations after every time step, Δt. For these calculations, the time-dependent fluxes at either sides of the phase boundary are obtained from equations (16) and (21), respectively.

6.2.2.3 Stage III. Lithiation of β Phase

If the planar front moves across the entire thickness of the electrode, a third stage will be reached where there will be a single-phase lithiation in the Li-rich β-phase (Figure 6.3(c). The equations for variation in Li concentration in the β-phase can be developed as per the procedure outlined for the lithiation in α-phase in stage I (equations (1-11)). The only difference will be that the initial condition to be considered for stage III β-phase lithiation will be the concentration profile (say, $f_2(y)$) in the β phase towards the end of stage II.

6.2.3 Butler-Volmer Kinetics at Electrolyte/$LiFePO_4$ Interface

Lithiation of Li_xFePO_4, carried out at on nonequilibrium electrode at a C-rate, will result in the electrode potential deviating from the equilibrium potential value. This deviation from the equilibrium condition, called the over potential, η is to be estimated as a function of state of charge (SOC) to predict the half-cell potential of Li_xFePO_4 electrode vs. Li/Li^+. This over potential is quantitatively estimated here using the Butler-Volmer (B-V) kinetics approach. The electrochemical charge transfer reaction during lithiation of $FePO_4$ can be written as:

$$Li^+ + e^- + FePO_4 \leftrightarrows LiFePO_4 \tag{23}$$

Taking the anodic current as positive, the net current, according to the B-V equation, is

$$I_{net} = I_{anodic} - I_{cathodic} = I_{oc}\left(\exp\left(\frac{\alpha F\eta_c}{RT}\right) - \exp\left(\frac{-(1-\alpha)F\eta_c}{RT}\right)\right) \tag{24}$$

where α is the charge-transfer coefficient for the anodic reaction (taken to be 0.5 here), η_c is the activation over potential at the Li_xFePO_4 electrode/electrolyte interface, and I_{oc}, the corresponding equilibrium exchange current density. Since, lithiation of $FePO_4$ is a cathodic reaction, both I_{net} and η_c will have negative values. Following the established approach[18] that is used for describing B-V kinetics in insertion electrodes, the equilibrium exchange current density can be written as:

$$I_{oc} = FSk\,[C_{Li^+}]^{\alpha}[C_{max} - C(0,t)]^{\alpha}[C(0,t)]^{1-\alpha} \tag{25}$$

where k is the standard rate constant for the charge transfer reaction (equation (23)) at the electrode/electrolyte interface and is a function of the forward and reverse rate constants, C_{Li^+} is the concentration of Li^+ ions in the electrolyte (taken to be 1mol/L here), C(0,t) is the time-dependent or transient concentration of Li in the Li_xFePO_4 electrode at the electrode/electrolyte interface (and is obtained from equation (11) or (16), depending on whether single phase or two-phase lithiation is considered, respectively) and C_{max} is the maximum possible Li concentration in the lithiated alloy. This corresponds to the Li concentration in $LiFePO_4$, at which lithiation is considered to stop. The time-dependent equilibrium exchange current density from equation (25) is used in equation (24) along with I_{net} (or the C-rate) to determine the over potential η and then the half-cell potential, for Li_xFePO_4 vs. Li/Li^+.

6.2.4 Ohmic Resistance during Lithiation of Li_xFePO_4

Apart from the activation over potential at the electrode/electrolyte interface, ohmic losses due to movement of electrons through the electrode material also need to be taken into account. This is particularly relevant for Li_xFePO_4 electrode because of its low conductivity. It is well known that the conductivity of intrinsic Li_xFePO_4 powders is not high enough to function effectively as an electrode [ref] but the addition of C to the Li_xFePO_4 increases the conductivity from 10^{-6} S/cm to 10^{-3}-10^{-4} S/cm[19], which is still lower than that of other cathode materials.

It has also been reported that the electronic conductivity of $FePO_4$ (α) phase is higher than that of $LiFePO_4$ (β) phase[20]. This indicates that as the α phase regions in the electrode get converted to β phase, the overall average resistance of the electrode increases. The average resistance of the electrode with both the phases, R_{avg}, which depends on the location of the β-phase in the electrode (b(t)), can be calculated in terms of the resistivities of each phase, using the following formula:

$$R_{avg} = \rho_\beta \frac{b(t)}{S} + \rho_\alpha \frac{L_c - b(t)}{S} \tag{26}$$

where ρ_α and ρ_β are the resistivities of the α and β phases, respectively. The ohmic potential loss, as a function of time of lithiation can then be calculated as IR_{avg}.

The actual electrode potential of Li_xFePO_4 during lithiation, E_c, is obtained as a function of SOC by subtracting the kinetic over potentials and the ohmic losses from the equilibrium lithiation voltage of Li_xFePO_4, at a given SOC, i.e.,

$$E_c = E_{eq,c} - \eta_c - IR_{avg} \tag{27}$$

The equilibrium voltage, E_{eq}, for lithiation of Li_xFePO_4 is obtained from the literature[5]. The activation over potentials, η_c and the ohmic losses are calculated using the equations (24) and (26), respectively.

6.2.5 Modeling of Delithiation of LiC_6 Electrode

In a Li-ion cell with graphite/ $LiFePO_4$ electrodes, the discharge occurs when graphite is delithiated and $FePO_4$ is lithiated. For proper cell performance, the rate of delithiation of graphite should be commensurate with the rate of lithiation of $FePO_4$. For lithiation to occur in $FePO_4$, delithiation should occur from graphite. Hence, in this section, the delithiation of LiC_6 electrode or lithiated graphite is modeled as a half-cell.

In this section, we model the cell discharge, i.e., the delithiation of precharged or lithiated graphite electrode. Lithium intercalation in graphite involves the formation of a series of different structures, each having a specific number of graphene layers between the intercalated Li layers[21], with the final lithiated phase having the formula LiC_6. For our model, we assume that the charged graphite at the beginning of cell discharge is in its fully lithiated state (LiC_6). We will now mathematically model the Li diffusion/transport within the lithiated graphite and charge transfer processes during Li removal from this electrode. The equations thus obtained will be used to determine the half-cell (graphite vs. Li/Li$^+$) potentials, as a function of SOC.

6.2.5.1 Analytical Modeling of Li Diffusion during Delithiation of LiC$_6$

Even though discharge of LiC$_6$ proceeds through the formation of several intermediate structures, including LiC$_{12}$, for purposes of mathematical simplicity, we assume that the lithiated graphite behaves like a solid solution of the form, Li$_x$C$_6$ with x varying continuously from 1 to 0. This assumption is justified because there is not much difference in the concentrations of Li in the different structures formed during delithiation. The schematic for the development of Li concentration profile within the graphite electrode during delithiation is shown in Figure 6.4. The governing equation for Li concentration within the electrode is

$$\frac{\partial C_a(x,t)}{\partial t} = D\frac{\partial^2 C_a\,(y,t)}{\partial y'^2}\,for\ y' \in (0, L_a) \tag{28}$$

where y' is the local coordinates for the graphite electrode, with y'=0 being the graphite/electrolyte interface and with the current collector at y'=L$_a$. C$_a$ (y',t) is the Li concentration at a location y' inside the electrode at time t, and D is the diffusion coefficient of Li in Li$_x$C$_6$ (it is assumed to be independent of x). The initial and boundary conditions are as follows:

$$C_a(y',0) = C_0 \tag{29}$$

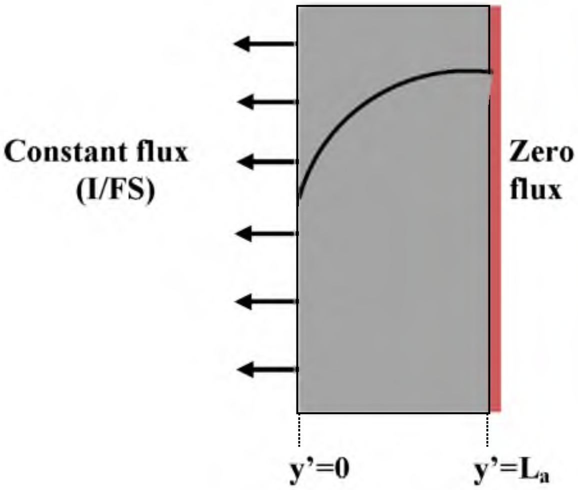

Figure 6.4 Typical development of Li profile during delithiation in Li_xC_6

$$-D\frac{\partial C_a}{\partial y'}\bigg|_{y'=0} = -\frac{I}{FS} \tag{30}$$

$$\frac{\partial C_a}{\partial y'}\bigg|_{y'=La} = 0 \tag{31}$$

where C_0 is the maximum Li concentration in graphite, corresponding to LiC_6. Following the same approach of separation of variables (Section 6.2.2.1) the solution for this diffusion problem can be obtained as:

$$\begin{aligned} C_a(y',t) = C_0 + \frac{IL_a}{6DFS} - \frac{I}{2DFSL_a}(y'-L_a)^2 - \frac{I}{FSL_a}t \\ + \frac{2IL_a}{\pi^2 DFS}\sum_{n=1}^{\infty}\frac{1}{n^2}\cos\left(\frac{n\pi}{L_a}y'\right)\exp\left(-\frac{n^2\pi^2}{L_a^2}Dt\right) \end{aligned} \tag{32}$$

This is the general solution for the Li concentration within the graphite electrode as a function of location within the electrode and time. The delithiation will stop when the surface concentration $C_a(0,t)$ reaches zero.

6.2.5.2 Butler-Volmer Kinetics at Electrolyte-Graphite Interface

The Butler-Volmer kinetics approach is again used here to compute the activation over potential at the graphite/electrolyte interface. The delithiation reaction of Li_xC_6 can be written as:

$$Li_xC_6 \leftrightarrows x\, Li^+ + x\, e^- + 6C \tag{33}$$

According to the B-V first order kinetics, the net current, I_{net} can be written as

$$I_{net} = I_{anodic} - I_{cathodic} = I_{oa}\left(\exp\left(\frac{\alpha F \eta_a}{RT}\right) - \exp\left(\frac{-(1-\alpha) F \eta_a}{RT}\right)\right) \tag{34}$$

where η_a is the activation over potential associated with delithiation of Li_xC_6, I_{0a} is the equilibrium exchange current density for the reaction, α is the charge transfer parameter. The equilibrium exchange current density has a similar expression as that for Li_xFePO_4 electrode:

$$I_{0a} = FSk_a\,[C_{Li^+}]^{\alpha}[C_0 - C_a(0,t)]^{\alpha}[C_a(0,t)]^{1-\alpha} \tag{35}$$

where k_a is the standard rate constant for the delithiation reaction, C_0 the Li concentration in LiC_6, and $C_a(0,t)$ the instantaneous surface concentration of Li in the electrode, which is obtained from equation (32).

For delithiation, the net current will be positive and hence the over potential will also be positive. This over potential must be added to the equilibrium voltage of graphite (vs. Li/Li$^+$), as a function of Li composition in the electrode, in order to obtain the actual potential of the graphite as a function of discharge time.

6.2.5.3 Ohmic Resistance during Delithiation in Graphite

The graphite electrode has a much higher electronic conductivity than Li_xFePO_4, however, it is well known that the formation of the solid electrolyte interface (SEI) layer on the electrode surface introduces a resistance[22], which needs to be taken into account while modeling the actual potential of the half-cell. The value of this resistance could be a function of the state of discharge, but for the purposes of this work, a constant value for it will be considered. Thus, the actual potential of the graphite during delithiation will be

$$E_a = E_{eq,a} + \eta_a + IR_{SEI} \qquad (36)$$

6.2.6 Electrode Parameters used in Simulation

Table 6.1 lists all the parameters used for both the electrodes (graphite and $LiFePO_4$) in the simulation. The diffusion coefficient values for the $LiFePO_4$ and graphite electrodes are necessarily higher than the reported values in literature. This is because in a macrohomogeneous model, Li diffusion is assumed to occur across the thickness of the electrode by planar lithiation front movement and not across individual nanometer-sized electrode particles. This "effective diffusion coefficient" can be argued[11] to be of the order of the Li diffusion coefficient in organic electrolytes. This may be because in $LiFePO_4$ electrodes made by a mixing carbon and $FePO_4$ particles, Li diffusion occurs in three parts: C, $FePO_4$ and the interfaces between them.

The values for the resistivities of the two phases in Li_xFePO_4 were obtained from

Table 6.1 List of parameter values used in the simulations

D, Li diffusion coefficient in Li_xC_6	10^{-6} cm^2/s
D_α, Li diffusion coefficient in α phase $FePO_4$	$3x10^{-6}$ cm^2/s
D_β, Li diffusion coefficient in β phase $LiFePO_4$	$5x10^{-7}$ cm^2/s
k_c, standard rate constant for lithiation of $FePO_4$	$5x10^{-5}$ $cm^{2.5}mol^{-0.5}s^{-1}$
k_a, standard rate constant for delithiation of LiC_6	10^{-4} $cm^{2.5}mol^{-0.5}s^{-1}$
$C_{\alpha/\alpha\beta}$, maximum solubility in α phase $FePO_4$	0.0006 mol/cm^3
$C_{\alpha\beta/\beta}$, minimum solubility in β phase $LiFePO_4$	0.0212 mol/cm^3
C_{max}, Li concentration in $LiFePO_4$	0.0228 mol/cm^3
ρ_α , resistivity of α-phase	2000 Ω-cm
ρ_β , resistivity of β-phase	5000 Ω-cm
L_c, thickness of the Li_xFePO_4 cathode	70 μm
C_0, Li concentration in LiC_6	0.029 mol/cm^3
α, charge transfer coefficient	0.5
RSEI, resistance of SEI layer on graphite	25 Ω
La, thickness of the Li_xC anode	35 μm
C_{Li+} , Li concentration in electrolyte	0. 001 mol/cm^3
S, surface area	1 cm^2
F, Faraday's constant	96485 Coulombs/mol

the specified ranges for the overall conductivity of the $LiFePO_4$ electrode material, when mixed with C[23]. An average value of the resistance of the SEI layer for graphitic anode was chosen, close to the reported values [24]. The standard rate constants for both the reactions were back-calculated from the reported values of the equilibrium exchange current densities at known states of charge/discharge, respectively[25].

The electrode thicknesses assumed in our simulations were based on the reported values of the electrode dimensions in commercial 18650 $LiFePO_4$/C cells[26]. With these dimensions, the absolute capacities of the anode and the cathode are matched in the cell— this requires that the thickness of $LiFePO_4$ electrode to be twice as thick as the graphite electrode.

6.3 Results and Discussion

6.3.1 Development of Concentration Profiles within Electrodes

Figures 6.5(a) and 6.5(b) show the development of transient Li concentration profiles within Li_xFePO_4 electrodes at different states of charge during lithiation at C/5 and 5C rates, respectively. These profiles were obtained with the help of equations (11), (16) and (21). It can be seen that at lower C-rate of C/5, the β/α phase boundary moves throughout the entire thickness of the electrode, following which Li insertion continues to occur in the β-phase. At this C-rate, the electrode appears to be in a state of equilibrium, as evidenced by the almost constant Li concentration profile through the electrode thickness at the end of lithiation corresponding to near maximum lithiation capacity (155 mAh/g).

On the other hand, for a higher C-rate of 5C, the surface concentration reaches the limiting value of Li concentration at a specific capacity of only 85 mAh/g, well before the

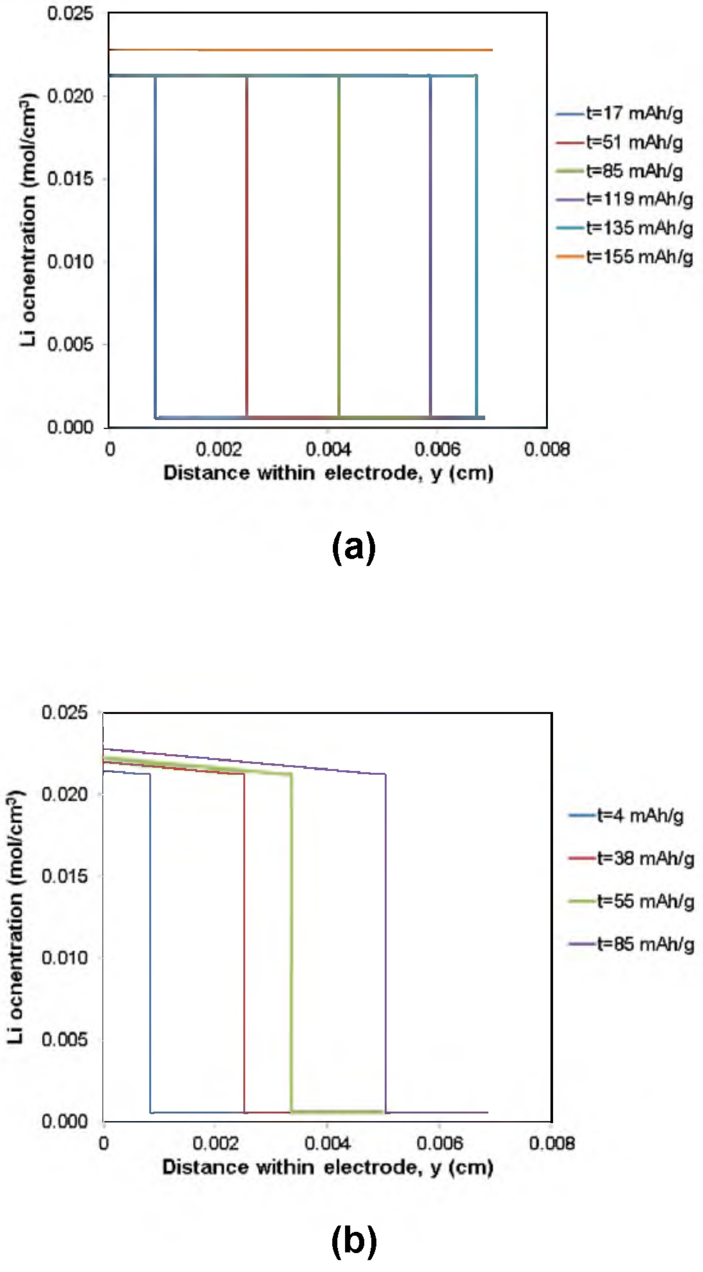

Figure 6.5 Development of Li concentration profiles during lithiation of Li_xFePO_4 electrode at (a) 0.2C rate and (b) 5C rate, and Li concentration profiles during delithiation in Li_xC electrode at (c) 1C rate and (d) 20C rate

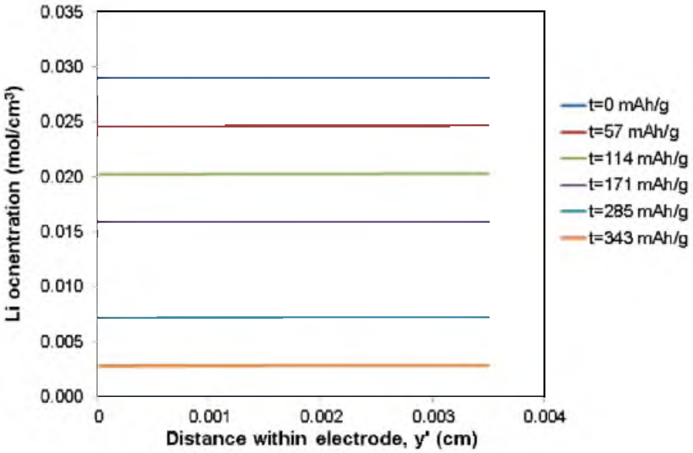

(c)

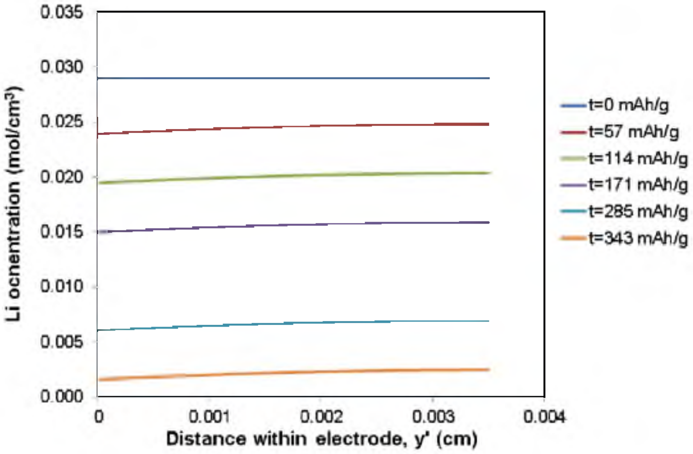

(d)

Figure 6.5 continued

two-phase boundary advanced through the entire electrode thickness. The concentration profiles are shifted from equilibrium but still linear, indicative of steady state conditions, which were reached due to the high value of the effective diffusivity.

Figures 6.5(c) and 6.5(d) show the variation of Li concentration within Li_xC_6 electrodes at different states of discharge during delithiation at C-rates of 1C and 20C, respectively. It can be seen that at a lower C-rate of 1C, the electrode appears to be in a state of equilibrium—there is not much difference between the surface and the bulk concentration values. At a higher C-rate of 20C, a slightly nonlinear Li profile, indicating a small deviation from the equilibrium state, is observed in the electrode.

6.3.2 Comparison of Simulated and Experimental Behavior of Li_xFePO_4 /Li Half-Cell

Figure 6.6 shows the simulations (lines) and the experimental data (points) for the lithiation voltages of $LiFePO_4$ in a half cell with Li as the counter electrode, at different C-rates between 10C and 1C. There is excellent agreement between the simulated curves and the experimentally observed voltage curves, especially in the beginning stages of lithiation. At higher C-rates, however, the half-cell exhibits sloping voltage profiles instead of the flat plateau associated with two-phase regions. This could be attributed to rapid Li accumulation on the electrode surface during the two-phase regime and/or due to greater ohmic losses with the growth of the β-phase. On the other hand, at 1C-rate, we see the simulated curve resembles the equilibrium condition, where we have a flat plateau corresponding to movement of the two-phase boundary and finally there is a sudden drop in voltage corresponding to lithium insertion in single β-phase. The drop in voltage corresponds to the state where the Li concentration at the electrode-$LiFePO_4$ surface has

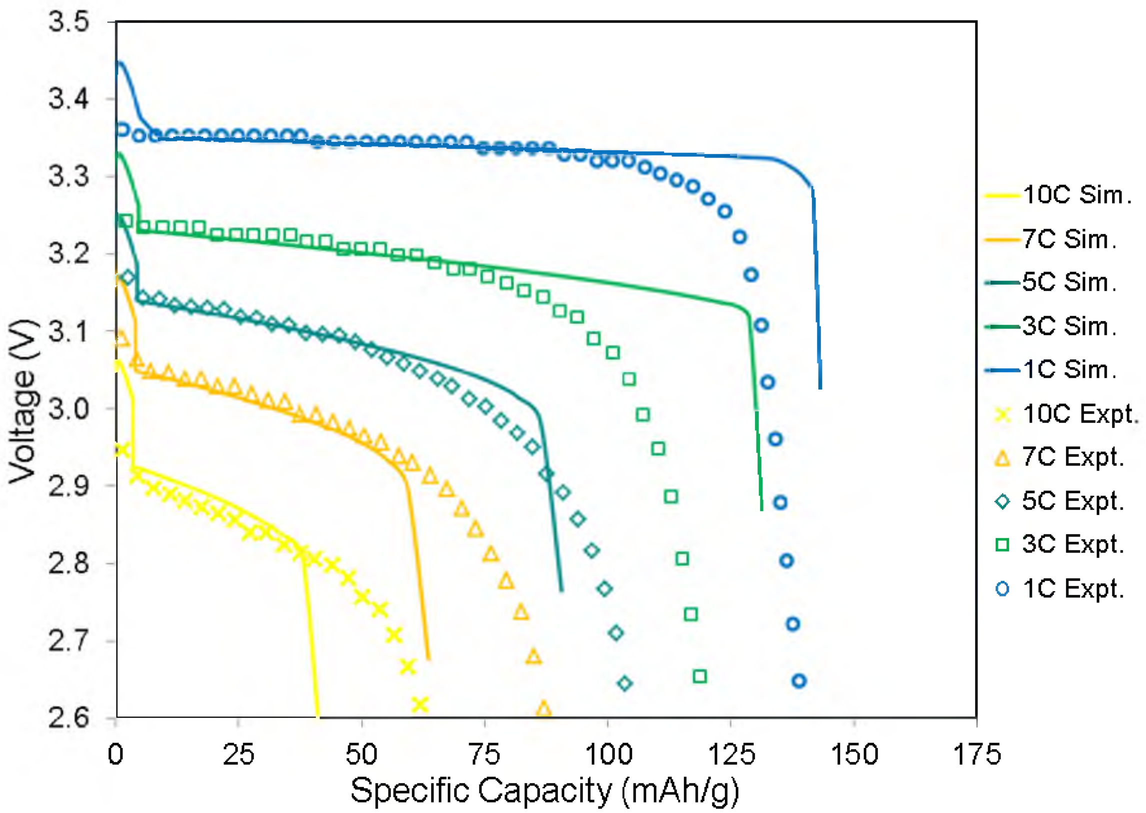

Figure 6.6 Simulations (lines) and experimental data (markers) for the lithiation voltages of Li_xFePO_4 cathode (in a half-cell with Li as counter electrode) at different C-rates

reached the maximum Li concentration that can be inserted in $FePO_4$.

The simulations tend to underestimate the lithiation capacities at higher C-rates and overestimate the capacities at lower C-rates. This discrepancy could perhaps be attributed to the assumption of concentration-independent diffusion coefficient in the Li-rich β-phase, Li_xFePO_4. A model which incorporates a concentration-dependent Li diffusion coefficient value, one that decreases with x in Li_xFePO_4 ($0.93< x <1$), might provide the simulated data that are in better agreement with the experimentally observed lithiation characteristics in Li_xFePO_4 cathode material. The Li diffusion coefficient in the Li-rich β-phase has been observed to decrease with increasing Li content[27].

6.3.3 Comparison of Simulated and Experimental Behavior of Li_xC_6 /Li Half-Cell

Figure 6.7 shows a comparison of the simulated results and the experimental data for the Li_xC_6/Li half-cell voltages during delithiation of LiC_6 at C-rates between 0.2C to 20C. There appears to be good agreement between the simulated and the experimentally observed delithiation voltage curves. In the initial stages of delithiation, the simulated voltage curves reach values that are higher than the experimentally observed voltages. The agreement between simulations and the experimental data becomes excellent for specific capacities >100 mAh/g. It is possible that the resistance associated with the SEI layer increases during delithiation as the thickness of the SEI layer increases [28].

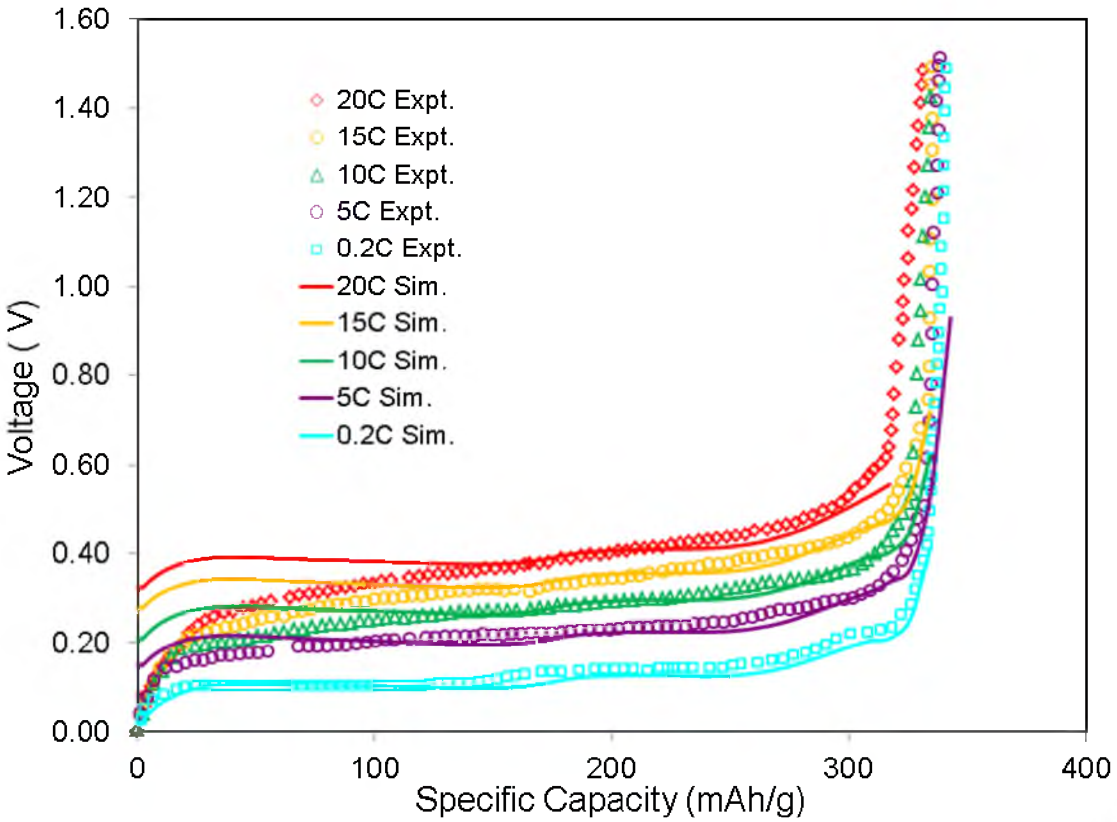

Figure 6.7 Simulations (lines) and experimental data (markers) for the delithiation voltages of LiC_6 electrode (in a half-cell with Li as counter electrode) at different C-rates

Therefore, the assumption of a constant value for the SEI layer resistance in the simulations could be leading to higher voltages during the initial stages of delithiation.

6.3.4 Comparison of Simulated and Experimental Behavior of Li_xFePO_4 / Li_xC_6 Full Cell

Since the absolute capacities of Li_xFePO_4 and Li_xC_6 electrodes were matched, the overall cell voltage can be obtained by subtracting the delithiation voltage of Li_xC_6 (vs. Li/Li^+) from the lithiation voltage of Li_xFePO_4 at corresponding states of charge/discharge, for a specific C-rate. The overall cell voltage as a function of discharge time was thus obtained here for the graphite-$LiFePO_4$ cell.

A comparison of the simulation results with the experimental data for overall cell discharge at different C-rates between 0.2C to 5C is shown in Figure 6.8. Here, the cell voltage is plotted as a function of the absolute cell capacity, which is 5.75 Ah, in this case. It can be seen that the simulated cell voltage curves agree well with the experimental data. The local plateaus in the discharge curves at lower C-rates (0.2C and 1C) can be attributed to the formation of different structures in graphite during delithiation. These plateaus are not present at higher C-rates and the discharge curves show a general downward sloping trend, which indicates that the shape of the discharge curves at higher C-rates is controlled more by the discharge characteristics of $LiFePO_4$ cathode than by the delithiation of graphite. The simulations agree well with the experimental data towards the initial stages of cell discharge but towards the end of discharge, the experimentally observed voltages drop more smoothly. It is not clear if this difference at the end of cell discharge occurs due to higher ohmic resistance at the end or lower diffusivity in the β-phase as x in Li_xFePO4 reaches values close to 1. The final cell

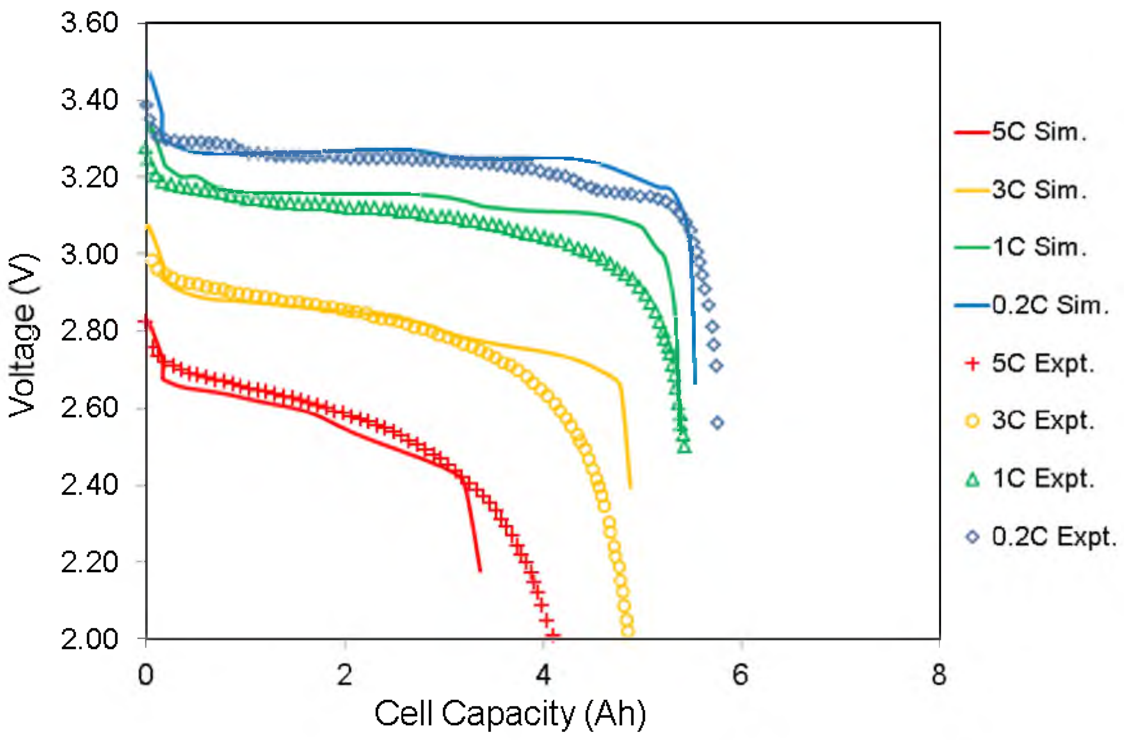

Figure 6.8 Comparison of the simulated cell voltage data (lines) with the experimental data (markers) corresponding to the discharging of Li_xFePO_4 / Li_xC_6 cells at different C-rates

discharge capacities in the simulations do appear to be determined by diffusion limitations within Li_xFePO_4 cathode, and not in the graphite anode, because the final drop in the discharge voltages was associated with the surface Li concentration reaching the maximum possible value in the β-phase in $LiFePO_4$ electrode.

6.4 Conclusions

1. Analytical models that enable mathematical simulation of one-dimensional-Li-transport and electron transfer in Li_xFePO_4 cathode and Li_xC_6 anode have been developed. The models include a proper description of phase boundary movement within $LiFePO_4$ electrode upon

lithiation and thus provide an accurate modeling of lithiation processes. The simulated results showed good agreement with experimental data for the time-dependent half-cell potentials of graphite and $LiFePO_4$ electrodes.

2. The simulation results of lithiation and delithiation in Li_xFePO_4 /Li and the Li_xC_6 /Li half-cells were coupled together to predict the discharge voltage in the overall Li_xFePO_4 / Li_xC_6 cell, that was capacity-matched. This means that the present model simulates the cell behavior very well. This should greatly facilitate examination of the effects of various cell parameters analytically to optimize and design Li-ion cells.
3. It was found that diffusional transport limitations of Li in the Li_xFePO_4 electrode during lithiation determined the overall discharge capacity of the cell. The electrochemical performance of the graphite was better at higher C-rates and hence, the anode was not the limiting factor in the overall cell-discharge experiments.
4. It appears that the agreement between the simulations and the experimental data for the Li_xFePO_4 lithiation and delithiation of Li_xC_6 can be improved if (a) a concentration-dependent Li diffusion coefficient in the Li-rich β-phase in Li_xFePO_4 can be incorporated in the simulations, and (b) if a time-varying SEI layer resistance in graphite anode is considered while accounting for the ohmic losses in the anode.

6.5 References

1. G. G. Botte, V. R. Subramanian and R. E. White, *Electrochimica Acta*, **45**, 2595 (2000).

2. J. Newman and W. Tiedemann, *AIChE Journal*, **21**, 25 (1975).

3. R. Darling and J. Newman, *Journal of The Electrochemical Society*, **144**, 4201 (1997).

4. M. Doyle, T. F. Fuller and J. Newman, *Journal of The Electrochemical Society*, **140**, 1526 (1993).

5. V. Srinivasan and J. Newman, *Journal of The Electrochemical Society*, **151**, A1517 (2004).

6. G. Chen, X. Song and T. J. Richardson, *Electrochemical and Solid-State Letters*, **9**, A295 (2006).

7. L. Laffont, C. Delacourt, P. Gibot, M. Y. Wu, P. Kooyman, C. Masquelier and J. M. Tarascon, *Chemistry of Materials*, **18**, 5520 (2006).

8. U. S. Kasavajjula, C. Wang and P. E. Arce, *Journal of The Electrochemical Society*, **155**, A866 (2008).

9. C. Wang, U. S. Kasavajjula and P. E. Arce, *The Journal of Physical Chemistry C*, **111**, 16656 (2007).

10. M. Safari and C. Delacourt, *Journal of The Electrochemical Society*, **158**, A562 (2011).

11. S. J. Harris, A. Timmons, D. R. Baker and C. Monroe, *Chemical Physics Letters*, **485**, 265 (2010).

12. J. L. Allen, T. R. Jow and J. Wolfenstine, *Chemistry of Materials*, **19**, 2108 (2007).

13. M. Tang, J. F. Belak and M. R. Dorr, *The Journal of Physical Chemistry C*, **115**, 4922 (2011).

14. S. I. Nishimura, G. Kobayashi, K. Ohoyama, R. Kanno, M. Yashima and A. Yamada, *Nature Materials*, **7**, 707 (2008).

15. M. Takahashi, S. Tobishima, K. Takei and Y. Sakurai, *Journal of Power Sources*, **97**, 508 (2001).

16. T. Maxisch and G. Ceder, *Physical Review Series-B*, **73**, 174112 (2006).

17. J. L. Dodd, R. Yazami and B. Fultz, *Electrochemical and Solid-State Letters*, **9**, A151 (2006).

18. K. Thomas, J. Newman and R. Darling, *Advances in Lithium-Ion Batteries*, 345 (2002).

19. S. Y. Chung, J. T. Bloking and Y.-M. Chiang, *Nature Materials*, **1**, 123 (2002).

20. C. Zhu, K. Weichert and J. Maier, *Advanced Functional Materials*, **21**, 1917 (2011).

21. K. Jalkanen, T. Aho and K. Vuorilehto, *Journal of Power Sources* (2013).

22. S. Zhang, M. S. Ding, K. Xu, J. Allen and T. R. Jow, *Electrochemical and solid-state letters*, **4**, A206 (2001).

23. H. C. Shin, W. I. Cho and H. Jang, *Electrochimica Acta*, **52**, 1472 (2006).

24. S. Zhang and P. Shi, *Electrochimica Acta*, **49**, 1475 (2004).

25. K. G. Gallagher, D. W. Dees, A. N. Jansen, D. P. Abraham and S.-H. Kang, *Journal of The Electrochemical Society*, **159**, A2029 (2012).

26. V. Srinivasan and J. Newman, *Journal of The Electrochemical Society*, **151**, A1530 (2004).

27. P. P. Prosini, M. Lisi, D. Zane and M. Pasquali, *Solid State Ionics*, **148**, 45 (2002).

28. C. Wang, A. J. Appleby and F. E. Little, *Journal of Electroanalytical Chemistry*, **497**, 33 (2001).

CHAPTER 7

CONCLUSIONS

7.1 Conclusions from Experimental Work

The conclusions that can be drawn from the work involving synthesis and electrochemical testing of Li-Mg alloy anodes for high capacity Li-ion batteries are as follows:

1. Li(Mg) alloy electrodes of two nominal compositions, Li_7Mg_3 and Li_8Mg, were successfully synthesized in the laboratory. The Li(Mg) alloy electrodes showed a delithiation behavior during cell discharge which is comparable to that of pure Li electrode.
2. A continuous and gradual phase transition from Li-rich BCC β-phase to Li-lean α-phase occurred, evidencing a diffusion-controlled Li transport process, during the delithiation of the electrodes. The accompanying shifts in X-ray diffraction peaks were consistent with the notion of RT Li diffusion causing the phase transition during delithiation.
3. The Mg-rich electrodes after discharge were structurally intact, suggesting Mg can act as a host for Li insertion and removal.
4. The cyclic reversibility of the Li(Mg)-$LiCoO_2$ cell was limited as indicated by the charging potential saturating to about 4V over all the cycles. There was some experimental indication of limited alloying of Li with Li(Mg) during charging.

The conclusions from the work involving synthesis and electrochemical testing of porous Si columnar structures can be summarized as follows:

1. Four different columnar morphologies were successfully synthesized on p-type [100] oriented Si wafers by electrochemical etching using an

electrolyte made of HF and DMF.

2. The electrochemical performance of two electrodes with porosities between 50-65% and with a clear columnar structure was the best —the reversible capacities at the end of 20th cycle for these electrodes were in excess of 1000 mAh/g, which is significantly higher than most values reported in literature for Si electrodes with columnar structures.
3. The Si electrode with the largest open porosity (75%) was not able to provide significant cyclic lithiation and delithiation capacities (<150 mAh/g) during cycling tests. This appears to be due to the gross destruction of the columnar/porous structure.
4. An important finding is that the columnar structure is preserved in the different Si electrodes after charge/discharge cycling. The electrochemical performance appears to be clearly linked to the morphology of the columns.

7.2 Conclusions from Theoretical Modeling Work

The first part of the modeling work which involved analytical modeling and simulation of electrochemical charge/discharge characteristics of a-Si thin film anodes led to the following conclusions:

1. A complete analytical modeling framework for predicting the charge/discharge potential behavior of a-Si thin film electrodes during lithiation/delithiation processes was developed. The model utilizes two important steps: (i) explicit consideration of transient Li concentrations within the electrode determined by solving diffusive mass transport

equations and (ii) the determination of time-dependent activation over potentials, as calculated from the Butler-Volmer equation.

2. The simulated charge/discharge potential variation as a function of capacity agreed well with the experimental data of lithiation/delithiation voltages of a-Si film electrodes of different thicknesses and different C-rates.
3. It was shown that the modeling can simulate the hysteresis between charge/discharge voltage curves at different C-rates for a-Si film electrode. The simulations demonstrate that at higher C-rates, the increases in the electrode activation over potentials due to rapid Li build-up/depletion at the electrode surface cause widening of the hysteresis loop, whereas electrode-diffusion-limitations lead to reduced capacities.
4. The effect of C-rate on the lithiation/delithiation capacities was assessed for a-Si electrodes with different diffusivities and standard rate constants. It was found that electrode-diffusion-limitation is more important during delithiation than during the lithiation step, especially at higher C-rates. A reduction in the value of the standard rate constant, on the other hand, caused reduction in both lithiation and delithiation capacities at all C-rates.

The conclusions that emerge from the theoretical work involving integrated analytical modeling and simulation of discharge characteristics of a full graphite/$LiFePO_4$ cell are:

1. Analytical models that enable mathematical simulation of one-dimensional-Li-transport and electron transfer in Li_xFePO_4 cathode and

Li_xC_6 anode were developed. The models include a proper description of phasve boundary movement within $LiFePO_4$ electrode upon lithiation and thus provide an accurate modeling of lithiation processes. The simulated results showed good agreement with experimental data for the time-dependent half-cell potentials of graphite and $LiFePO_4$ electrodes. The simulated results agreed well with the experimental data for full cell (Li_xFePO_4 / Li_xC_6 cell) discharge as well.

2. It was found that diffusional transport limitations of Li in the Li_xFePO_4 electrode during lithiation determined the overall discharge capacity of the cell. The electrochemical performance of the graphite was better at higher C-rates and hence, the anode was not the limiting factor in the overall cell-discharge experiments.
3. It appears that the agreement between the simulations and the experimental data for the Li_xFePO_4 lithiation and delithiation of Li_xC_6 can be improved if (a) a concentration-dependent Li diffusion coefficient in the Li-rich β-phase in Li_xFePO_4 can be incorporated in the simulations, and (b) if a time-varying SEI layer resistance in graphite anode is considered while accounting for the ohmic losses in the anode.